DESIGN AND OPTIMIZATION OF DONOR-BASED SPIN QUBITS IN SILICON

A Dissertation

Submitted to the Faculty

of

Purdue University

by

Yu Wang

In Partial Fulfillment of the

Requirements for the Degree

of

Doctor of Philosophy

May 2017

Purdue University

West Lafayette, Indiana

THE PURDUE UNIVERSITY GRADUATE SCHOOL
STATEMENT OF DISSERTATION APPROVAL

Dr. Gerhard Klimeck, Co-Chair
    School of Electrical and Computer Engineering
Dr. Rajib Rahman, Co-Chair
    School of Electrical and Computer Engineering
Dr. Supriyo Datta
    School of Electrical and Computer Engineering
Dr. Zhihong Chen
    School of Electrical and Computer Engineering
Dr. Michelle Y. Simmons
    School of Physics, The University of New South Wales, Australia

Approved by:

Dr. Venkataramanan Balakrishnan
    Head of the School of Electrical and Computer Engineering

To my beloved wife and parents.

ACKNOWLEDGMENTS

I would like to thank my advisor, Professor Gerhard Klimeck who gave me this precious opportunity to work in his nanoelectronic modeling group. I began appreciating his work and achievements when I was an undergraduate student.

I would like to express my sincere gratitude to Dr. Rajib Rahman, Professor Michelle Y. Simmons, Professor Supriyo Datta and Professor Zhihong Chen for being my advisory committee members. Specially, I would like to thank Dr. Rahman who is guiding my research work on a daily basis. He led me into the world of solid-state quantum computing and helped me a lot in all perspectives. He is always patient and open to discussions. I benefit a lot from his knowledge, personality and his way of thinking and solving problems. I would like to thank Professor Simmons for valuable guidance and discussions during our frequent remote meetings. I would like to express my appreciation to Professor Datta, from whom I gained a lot of knowledge on quantum transport.

I would like to thank Professor Lloyd C. L. Hollenberg and Professor Andrew S. Dzurak for their valuable guidance and advice. I would also like to thank the colleagues, Dr. Holger Büch, Dr. Bent Weber, Dr. Thomas Watson, Dr. Fahd Mohiyaddin, Samuel Hile, Dr. Matthew House, Matthew Broome, Dr. Menno Veldhorst, Dr. Kok Wai Chan and Dr. Charles Hill in University of New South Wales and University of Melbourne for collaborations, discussions and their insights from an experimental perspective, and their help when I was visiting Sydney.

I would like to thank Dr. Yaohua Tan for his selfless help and insights on almost everything I started to work on. I would like to thank Dr. Yu He for his help with fixing problems when I began to work in this group. I would like to thank Yuling Hsueh, Rifat Ferdous, Archana Tankasala, Chin-Yi Chen and Harshad Sahasrabudhe for valuable cooperation, help and discussions. I would like to thank Dr. Zhengping

Jiang, Dr. Xufeng Wang, Pengyu Long, Dr. Kai Miao, Junzhe Geng, Yuanchen Chu, Xinchen Guo, and all the other colleagues in the Network for Computational Nanotechnology for friendship and help. I would also like to thank Ms. Vicki Johnson, Ms. Leslie Schumacher and Ms. Ashley Byrne for their kind help.

Last but not the least, I would like to thank my wife and my parents for their love and unconditional support. Without them, I cannot fulfill this important step in my life.

TABLE OF CONTENTS

LIST OF FIGURES

ABSTRACT

Wang, Yu Ph.D., Purdue University, May 2017. Design and optimization of donor-based spin qubits in silicon. Major Professor: Gerhard Klimeck.

Donor-based spin qubits in silicon are promising candidates for solid-state quantum computation as they have exceptionally long coherence time. Single donor and few-donor quantum dots can be patterned by scanning tunneling microscopy based lithography technique in silicon with atomic precision, making them propitious for building a scalable quantum computer. Compared to single donors, few-donor quantum dots have more nuclear spins and extra quantum confinement, leading to additional degrees of freedom to engineer single and multi-qubit operations, while retaining long coherence times. Combined, they can be utilized to obtain outstanding performance or novel approaches for qubit operation.

In this work, approaches for design and optimization of donor-based spin qubits in silicon are proposed based on atomistic simulations, focusing on qubit characterization, manipulation and readout. For few-donor qubits, we put forward a metrology technique to obtain their atomic scale information, needed for single qubit manipulation. Also, a new design is introduced for two-qubit gates to gain flexibility in device fabrication and tuning the exchange coupling, in which theoretical guidance to the realization of two-qubit logic is provided. In addition, an all-electric spin control scheme is proposed, giving rise to a promisingly scalable architecture of a donor-based quantum computer. We also explore the electrical and opto-electric hybrid spin readout under realistic electrostatics and device geometry, providing guidance for optimizing device parameters in experiments.

1. INTRODUCTION

Quantum logic provides a new paradigm for computing as the technology scaling of classical computing becomes more and more challenging. Due to the inherent properties of quantum computing, i.e. superposition and entanglement, massive parallelism can in principle be realized, leading to tremendous speedup of computation. It has been claimed that a 30-qubit quantum computer would have about the same processing power as a conventional computer consisting of billions of transistors processing commands at 10 teraflops per second [1]. Some currently intractable problems, such as searching in a huge amount of data, quantum chemistry simulations, large network optimization, and protein folding could be potentially solvable with quantum computing algorithms within reasonable time.

In terms of the hardware that carries out quantum algorithms, one of the promising protocols is to utilize donor spins in silicon as quantum bits (qubits), i.e. the basic computing units. To achieve long coherence time, silicon is usually chosen as the host for spin qubits because it provides a spin-free environment (in enriched Si-28) and weak spin-orbit coupling. The coherence time of single electron spins bound to phosphorus donors in silicon is expected to be $\sim$10 s [2]. In comparison, gate-defined silicon quantum dots (QDs) that can also define spin qubits usually have shorter coherence times, ranging from $\sim 37\mu$s to $\sim$30ms [3, 4]. To perform quantum computing operations with donors, the popular Kane architecture [5] uses A-gates to control the hyperfine interactions between the donor electron and the nucleus to address individual qubits, and J-gates between two phosphorus donors to tune the exchange coupling between the two bound electrons (Fig. 1.1). Recently, tuning the hyperfine interactions by A-gates for individual qubits has been demonstrated [6], pushing it forward to the realization of donor-based quantum computing in silicon.

A donor-based hardware architecture has also been postulated for scalable silicon quantum computing using the surface code [7].

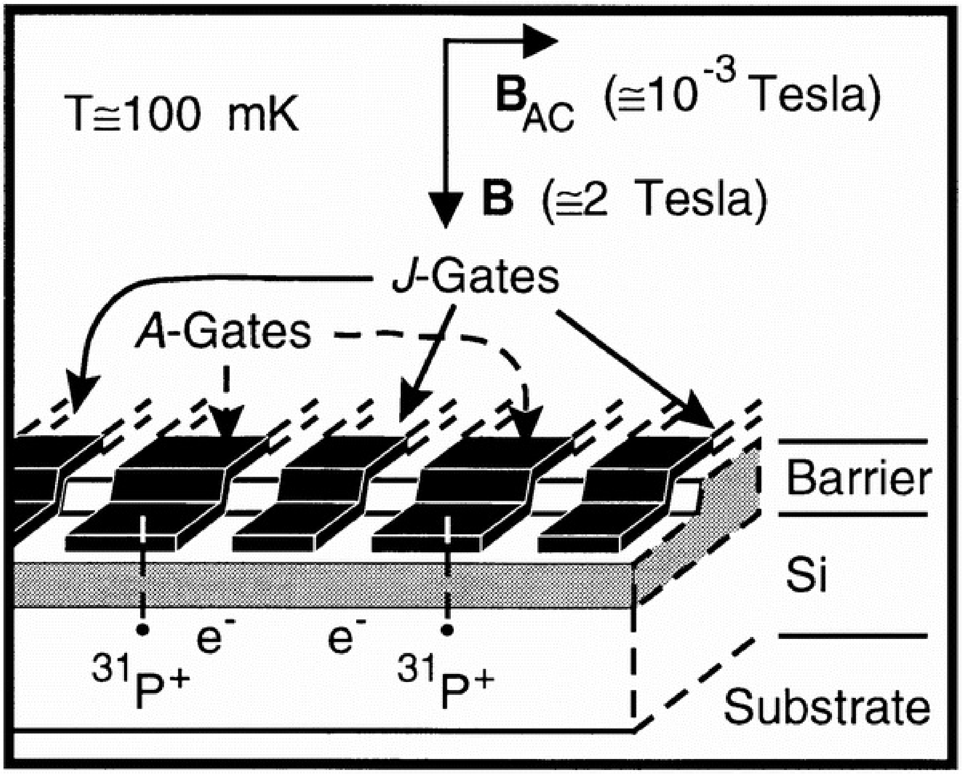

Fig. 1.1. 'A gates' control the resonance frequency of the nuclear spin qubits; 'J gates' control the electron-mediated coupling between adjacent nuclear spins. The ledge over which the gates cross localizes the gate electric field in the vicinity of the donors. (Adopted from Ref. [5].)

As to fabrication, recent advances in scanning tunneling microscope (STM) based lithography [8] have enabled the realization of donor-based QDs (or donor-clusters) buried deep in silicon and far from surfaces and interfaces with atomic precision [9], providing coherence times comparable or even superior to single donors in silicon. Electrons bound to these Si:P QDs are confined by the 3D Coulombic potential of a few donors located within a few nm^2 lithographic patch. These donor electrons can be electrostatically controlled by in-plane gates that can also be fabricated by the STM lithography technique [10]. Due to different quantum confinements and hyperfine interactions compared to single donors, few-donor quantum dots provide more flexibility in individual qubit addressing [10, 11] and exchange coupling engineering [12], which are favorable for multi-qubit operations. Already, transport spectroscopy has been performed on single, double, and triple Si:P QDs [13–15], and their single-electron spin readout and two-electron spin blockade have been demonstrated as well [10, 14].

To achieve robust and optimum performance of a donor-based quantum computer, improvements are still needed in terms of qubit characterization, operation and readout. In this work, we will provide guidelines for these three aspects based on atomistic simulations. For a donor-dot spin qubit, it is critical to relate the spin resonance frequency to its atomic spatial configuration, which is difficult to identify only from its STM image. In chapter 2, we propose a characterization technique for few-donor quantum dot qubits to resolve the uncertainty in configuration using electron spin resonance (ESR) techniques, exploiting the difference of quantum confinements and hyperfine interactions in different donor-dot qubits.

With recent demonstration of single qubits in silicon with both electron and nuclear spins of donors [16, 17], the next biggest challenge is to demonstrate two-qubit gates based on electron-electron exchange interaction in experiment. Ideally, the exchange coupling (J) in a two-qubit gate needs to be electrically tuned by several orders of magnitude between an 'Off' and an 'On' state within a small and realizable bias range. In the long run, such a J- and A-gate architecture in Kane's proposal leads to a high gate density, requiring ultra small gate widths to minimize electrical cross-talk between gates, and precise donor positioning relative to gates. Moreover, the tunability of the exchange coupling is limited both by the electric field range the J-gate can produce and the field ionization of the electrons to the surface. Previous calculations have also shown that the J-coupling oscillates as a function of donor separation due to crystal momentum states [18], and is therefore sensitive to atomic scale placement errors. All these issues lead to severe constraints in the implementation of a two-qubit gate in donors. In chapter 3, we will provide an alternative two-qubit gate design that circumvents these issues and provides highly tunable exchange coupling.

As it is challenging to use magnetic approach to control a spin qubit locally, it is more favorable to exploit schemes with electrical control. In chapter 4, we propose an approach to realize electrical control of donor-based spin qubits in silicon [19]. We utilize the difference of hyperfine couplings in two different donor-based qubits and put forward a device structure that is promisingly scalable and in the meantime, provides highly tunable two-qubit exchange interaction as described in chapter 3.

Fast readout of qubits with high-fidelity is one of the critical steps in performing quantum computation. Single-shot spin readout have been demonstrated in a single donor qubit [20] and a donor-cluster qubit [10]. The readout scheme is based on selectively loading or depleting a spin-up or spin-down electron in or from the qubit through quantum mechanical tunneling. The readout fidelity is governed by the tunnel time between the qubit and a nearby reservoir, e.g. a single-electron-transistor (SET) island [10]. In chapter 5, we develop a multi-scale method to model the quantum tunneling process in the spin readout phase in realistic devices, and provide guidelines for optimizing the tunnel times to achieve high readout fidelity.

Nuclear spins in semiconductors are also promising candidates for solid-state qubits with the advantage of exceptionally long spin coherence times and the potential to be integrated into the existing semiconductor device technology [5, 17, 21, 22]. Recent experiments have shown that donor nuclear spins in enriched silicon can achieve coherence times exceeding 30 minutes even at room temperature due to a semiconductor vacuum-like environment for spins [23]. However, the relative isolation of the nuclear spins from their environment also makes it difficult to prepare, and readout their spin states. Several recent experiments have utilized optical techniques to initialize and readout the donor nuclear spins in silicon by photo-excitation of a donor bound exciton - a three-particle system with two electrons and a hole bound to the donor [24–28]. While these experiments have so far been performed on bulk donor ensembles, the techniques will offer the best rewards if extended to single donor spin qubits in the already existing design schemes of a silicon quantum computer [29, 30]. Unlike the dominant spin readout techniques that rely on spin-to-charge conversion, optical readout can offer higher fidelities as it is not limited by temperature dependent broadening in the leads. In chapter 6, we investigate the electronic structure of donor bond exciton under electric field and interfaces, providing useful information in realistic design.

Here is a list of publications I have contributed to:

1) Y. Wang, C.-Y. Chen, G. Klimeck, M. Y. Simmons, and R. Rahman, “All-electrical control of donor-bound electron spin qubits in silicon,” arXiv:1703.05370 (2017) [19].

2) Y. Wang, C.-Y. Chen, G. Klimeck, M. Y. Simmons, and R. Rahman, “Characterizing Si:P quantum dot qubits with spin resonance techniques,” Sci. Rep. **6**, 31830 (2016) [11].

3) Y. Wang, A. Tankasala, L. C. L. Hollenberg, G. Klimeck, M. Y. Simmons, and R. Rahman, “Highly tunable exchange in donor qubits in silicon,” npj Quantum Information **2**, 16008 (2016) [12].

4) J. Huang, Y. Wang, P. Long, M. Povolotskyi, and G. Klimeck, “High-Performance Complementary III-V Tunnel FETs with Strain Engineering,” arXiv:1605.00955 (2016).

5) R. Rahman, J. Verduijn, Y. Wang, C. Yin, G. De Boo, G. Klimeck, and S. Rogge, “Bulk and sub-surface donor bound excitons in silicon under electric fields,” arXiv:1510.00065 (2015) [98].

6) Y.-L. Hsueh, H. Büch, Y. Tan, Y. Wang, L. C. L. Hollenberg, G. Klimeck, Michelle Y. Simmons, and Rajib Rahman, “Spin-lattice relaxation times of single donors and donor clusters in silicon,” Phys. Rev. Lett. **113**, 246406 (2014) [42].

7) Y. He, Y. Wang, G. Klimeck, and T. Kubis, “Non-equilibrium Green’s functions method: Non-trivial and disordered leads,” Appl. Phys. Lett. **105**(21), 213502 (2014).

2. CHARACTERIZING SI:P QUANTUM DOT QUBITS WITH SPIN RESONANCE TECHNIQUES

The work in this chapter is published in Ref. [11], and the text is taken from there.

2.1 Introduction

The popular Kane qubit proposal of single phosphorus based quantum computer [5] utilizes an ac-magnetic field for single qubit operations and an inter-donor exchange coupling for two-qubit operations. Experimentally, ac-magnetic fields have been used to perform electron spin resonance (ESR) and nuclear magnetic resonance (NMR) on single phosphorus electron [16] and nuclear spins [17] respectively. Recently, a two-qubit logic gate in gate-defined silicon QDs has also been demonstrated with ESR based single qubit control [31]. To utilize Si:P QDs as spin qubits, it is important to know the precise number of electron and nuclear spins bound to these dots, which can also help to identify appropriate spin transitions of the qubit and to deplete the dots down to the ideal regime of one electron occupation. Understanding the extent of the electron wavefunctions of the donor dots is important for optimizing the inter-dot exchange and tunnel coupling useful for two-qubit gates. In this chapter, we present a metrological method based on a non-invasive atomic-scale characterization technique to extract information about the donor numbers, electron numbers, and donor locations based on ESR measurements using the on-chip circuitry already needed for qubit manipulation. The method relies on probing the spin splittings of the donor dots through the electron-nucleus hyperfine coupling which is sensitive to atomic-scale details of the donor dot. To establish this metrology technique, we compute hyperfine couplings as a function of donor number, electron number, and donor locations using atomistic tight-binding method with a Hartree approximation, and show how the combined experimental characteristic with theoretical mapping can inform the use of donor dot qubits.

Although transport spectroscopy can also be used to determine the number of electrons bound to a donor dot [14] based on charging energy extraction for various charge transitions, such a procedure has some associated uncertainties as the charging energies depend on the electrostatics and geometry of the device and can show large variations between devices [14]. Moreover, electron transport depends on a complicated interplay of a number of parameters such as lead-to-dot tunnel couplings, dot energy levels, charging energies, spin and charge relaxation rates [9, 13]. As a result, it is often difficult to ensure that the last charge transition measured in the device indeed corresponds to a single electron occupation. Also, there are uncertainties in donor locations up to 1 nm resulting from donor incorporation mechanism, donor diffusion and segregation within the dot and in the leads [32]. All these effects produce a wide band of charging energies as shown in Ref [14], making the extraction of electron and donor numbers difficult. The proposed ESR based metrology circumvents these challenges and provides a more accurate way to characterize and customize Si:P QDs for spin qubit experiments.

First, we will discuss how this metrology works theoretically on different device samples. Fig. 2.1(a) shows a simplified schematic of a donor dot qubit with a microwave ESR line. In reality, this metrology can be performed on a Kane-like device [5] or any of the already realized silicon QD qubits operated with ESR [6, 16, 31]. The donor dot (shown as the red disk in the dashed rectangular region) is patterned into the silicon substrate (the pink box) by STM lithography [10]. A static magnetic field (B_0) is applied to the system to polarize the electron spins bound to the dot. The metal wire (the blue bar) deposited on the SiO_2 layer carries an alternating current that can generate an electromagnetic field (B_{ac} represented by the blue dashed ellipses) to rotate the qubit electron spin with microwave frequency. Spin readout can be performed by spin dependent tunneling to a single-electron-transistor using the protocol described in Refs [10, 20].

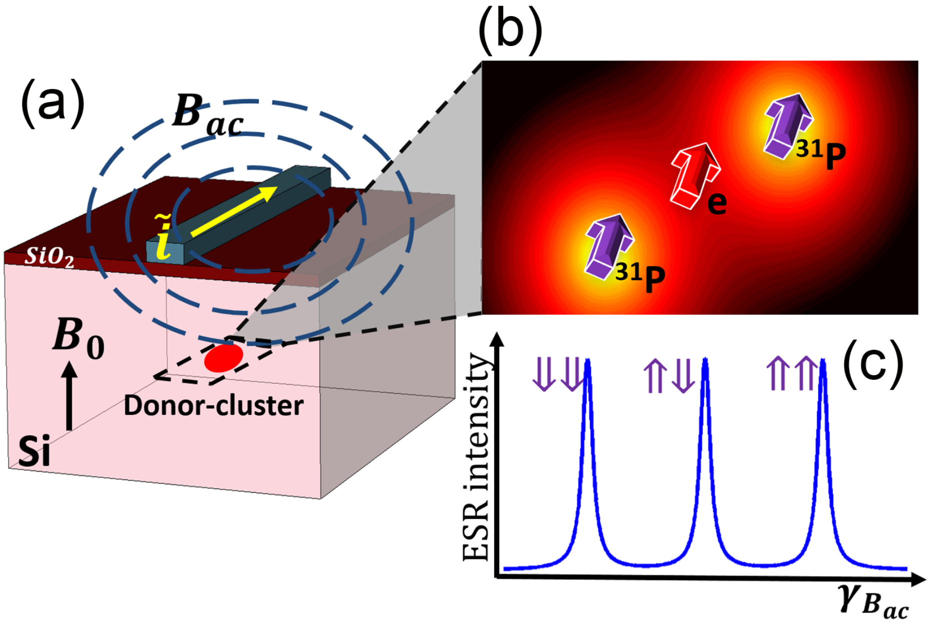

Fig. 2.1. (a) A schematic of a donor dot qubit device in silicon with ESR measurements using an ac-magnetic field (B_{ac}). (b) The potential landscape of a 2P donor-dot with one bound electron (2P:1e), where light color represents high magnitude and dark color represents low magnitude. The arrows indicate the nuclear and electronic spins. (c) The schematic of a representative ESR measurement on 2P:1e showing three transition peaks associated with given nuclear spin configurations (thick arrows).

Fig. 2.1(b) shows an electron spin (red arrow) bound by the quantum confinement of a 2P donor dot containing two nuclear spins (purple arrows). The background depicts its electrostatic potential landscape. The spins are coupled by the electron-nuclear hyperfine interaction which depends on both the nuclear spin orientation and the electronic probability density at the site of the nuclear spins. The latter is sensitive to the quantum confinement of the electron wavefunction provided by the potential of the donors, and hence, in the more general case, depends on the number of donors and electrons, as well as their locations. This dependency is crucial for the metrology technique proposed here as shown later. A solution of the electron-nuclear spin Hamiltonian with hyperfine interaction, magnetic dipole interaction, and an external B-field provide specific up/down transition frequencies at which we can address the electron spin.

Fig. 2.1(c) shows a schematic of three ESR transition frequencies that could exist for a 2P:1e dot associated with different possible orientations of the two nuclear spins (thick purple arrows). As the overall hyperfine interaction depends on the nuclear spin orientations, three possible ESR frequencies can be detected due to three possible nuclear spin configurations in a 2P donor dot. The splittings between the ESR peaks depends on the strength of the hyperfine interaction. Experimentally the transition frequencies can be resolved easily since the broadening of the peaks in the ESR spectrum are typically in the order of 1 kHz, and the separations between the peaks are in the order of 100 MHz as determined by the hyperfine interaction [17]. An experiment-theory comparison helps to map the number of peaks and their locations in the ESR spectra to specific configurations of the Si:P QD.

2.2 Methods

To accurately calculate the ESR frequencies of a Si:P QD, it is crucial to capture its electronic structure. Here we obtain the ESR frequencies by solving the effective spin Hamiltonian based on the atomistic tight-binding approach. A donor-dot consists of m nuclear spins and n electron spins localized in a silicon crystal lattice. In spin qubit experiments, a static external magnetic field $\vec{B}$ is applied to generate well-defined spin polarized states split by the Zeeman energy. Its effective spin Hamiltonian thereby can be expressed as

$$H_{spin} = H_{zeeman} + H_{hyperfine}. \tag{2.1}$$

The external B-field is included in the Zeeman term, H_{Zeeman}, as

$$H_{zeeman} = \sum_{i=1}^{n} g_e \mu_B \vec{B} \cdot \vec{S}_i - \sum_{j=1}^{m} g_n \mu_n \vec{B} \cdot \vec{I}_j, \tag{2.2}$$

where $\vec{S}_i$ and $\vec{I}_j$ denote the spin operator of the ith electron and the jth nucleus respectively. g_e and g_n are the electron and nuclear g-factors respectively. μ_B is the Bohr magneton and μ_n is the nuclear magneton. The second term, $H_{hyperfine}$, is the hyperfine interaction between electron spins bound to the donor-dot and the nuclear spins of the donors, and is given as,

$$H_{hyperfine} = \sum_{i}^{n} \sum_{j}^{m} A_{ij} \vec{I}_j \cdot \vec{S}_i + \sum_{i}^{n} \sum_{j}^{m} \vec{I}_j \cdot \widetilde{\widetilde{D}}_{ij} \cdot \vec{S}_i, \tag{2.3}$$

where A_{ij} represents the Fermi contact hyperfine coupling of the ith electron and the jth nuclei, which is proportional to the electronic probability density at the jth donor site. $\widetilde{\widetilde{D}}_{ij}$ is the anisotropic hyperfine (or magnetic dipolar) interaction tensor. A_{ij} and the components of $\widetilde{\widetilde{D}}_{ij}$ can be expressed as [33, 34]:

$$A_{ij} = \frac{\mu_0}{4\pi} g_e \mu_B g_n \mu_n \frac{8\pi}{3} |\Psi_i(\vec{R}_j)|^2, \tag{2.4}$$

$$D_{ij,kl} = \frac{\mu_0}{4\pi} g_e \mu_B g_n \mu_n \langle \Psi_i | \frac{3 r_k r_l - |\vec{r} - \vec{R}_j|^2 \delta_{kl}}{|\vec{r} - \vec{R}_j|^5} | \Psi_i \rangle, \tag{2.5}$$

where μ_0 is the vacuum permeability. Ψ_i is the wavefunction of the ith electron, $\vec{R}_j$ is the position vector of the jth nucleus, and $r_{k,l} = (x, y, z)$ are the electron position vector components. Although we consider both contact and the anisotropic hyperfine interactions in the simulations, we find that the $\widetilde{\widetilde{D}}_{ij}$ terms are at least three orders of magnitude less than the A_{ij} terms, analogous to the case of Si-29 in silicon [33, 34]. Hence, the spin splitting is mostly affected by the A_{ij} terms. This helps in the direct mapping of ESR frequencies to A_{ij} and eventually to the physical properties of the donor dot, as needed for the metrology. In obtaining the A_{ij} coupling from the tight-binding wavefunction, we adopt the same technique as Ref [35] using the experimentally measured hyperfine resonance frequency of 117.53 MHz for a bulk phosphorus as a calibration.

To obtain the electron wavefunctions, the tight-binding Hamiltonian of the silicon and the donor atoms is represented by an $sp^3d^5s^*$ spin-resolved atomic orbital basis with nearest neighbor interaction and spin-orbital coupling. The resulting eigenvalue problem is solved by a parallel block Lanczos algorithm for about 1.4 million atoms using the nanoelectronic modeling tool (NEMO-3D) [36]. The Hamiltonian contains three terms as shown below.

$$H = H_{Si} + H_D + H_{e-e}, \tag{2.6}$$

where H_{Si} represents the Hamiltonian of the silicon lattice, H_D denotes the central-cell corrected Coulomb potential energy given by the positive charges of donor cores, and H_{e-e} is the mean-field electron-electron interaction energy present for multi-electron occupation of the donor dot. The term H_{Si} contains the full bandstructure of silicon [37] along with hydrogen passivated surface atoms [38]. Each donor potential in H_D is represented by a Coulomb potential screened by the dielectric constant of silicon along with a central-cell correction term which assumes a constant potential U_0 at the donor site [35]. This model has been well calibrated with single donor spectroscopy measurements and reproduces all the bound states of the donor with correct energy levels [39]. The donor wavefunction obtained from this model also agrees very well with measurements from recent STM imaging experiments [40]. For multi-electron occupation, a mean-field method is utilized to reduce the computational complexity using the Hartree self-consistent field (SCF) approximation. In this scheme, the mean-field potential energy of the electrons is solved self-consistently with the Poisson equation, assuming that the electrons occupy the lowest states conforming to the Pauli exclusion principle. This method has successfully captured the experimental two-electron binding energy of a single donor in silicon called the D$^-$ state [41], multi-electron binding energies in donor dots [14], and can also reproduce experimentally measured spin-lattice relaxation times T_1 times in donor dots [42], providing us confidence in the mean-field approximation for multi-electron occupation.

As for multi-electron occupation, for qubit applications, we are mostly interested in effective 1/2 spin configurations of a donor dot, where there is an odd numbered electron in the dot. As indicated by eq. (2.3) and (2.4), the net hyperfine interaction at site $\vec{R_j}$ depends on the on-site spin density $\sum_{p=\uparrow} |\Psi_p(\vec{R_j})|^2 - \sum_{q=\downarrow} |\Psi_q(\vec{R_j})|^2$. The inner electrons form spin pairs occupying the same orbital states of the dot. As a result, they have identical spatial wavefunction but different spins S_i which leads to no contribution to the hyperfine term $\sum_i^n \sum_j^m A_{ij}\vec{I_j} \cdot \vec{S_i}$. Thereby, the hyperfine interaction as well as the ESR frequencies of donor-dot with multi-electron occupation only depends on the wavefunction of the unpaired outermost electron, which can be captured by the mean-field theory applied here.

2.3 Results and Discussions

In the results presented in the following, the simulation domain is set to 30nm × 30nm × 30nm of a regular silicon crystal lattice (∼1.4 million atoms) in NEMO-3D, so that the Coulombic potential of the donors approach almost zero near the boundaries of the domain. This ensures that the donor-dot bound wavefunctions are not affected by the artificial hard-wall confinement of the box of silicon. The P-donor dots are placed in the middle of the box in the (001) atomic plane. A static magnetic field $B_0 = 1.5$T is applied in the [001] direction.

First, we show how we can infer the number of donors in a donor-dot using ESR measurements. Fig. 2.2(a) shows the single-electron probability density distributions for 1 to 4 P donors in the central plane. Fig. 2.2(b) shows the energy levels computed from the spin Hamiltonian (eq. (2.1)) for single electron occupation. The levels are shifted relative to the ground orbital state located at zero energy for reference due to Zeeman effect. The number of energy levels increases with the number of donors in a dot, as the total number of nuclear spins increases. The spin orientations of the nuclear and electron spins can be identified from the eigenvectors of the spin Hamiltonian, and are shown in Fig. 2.2(b) as well. The transition frequencies for an electron spin flip can be computed from the difference between the up and down electron spin (thin arrows) states with the same nuclear spin orientations (thick arrows). Fig. 2.2(c) shows the ESR transition frequencies for the 4 cases. These transition frequencies correspond to the location of the peaks in a sample ESR measurement as illustrated in Fig. 2.2(c). Firstly, as expected the number of peaks increases with the

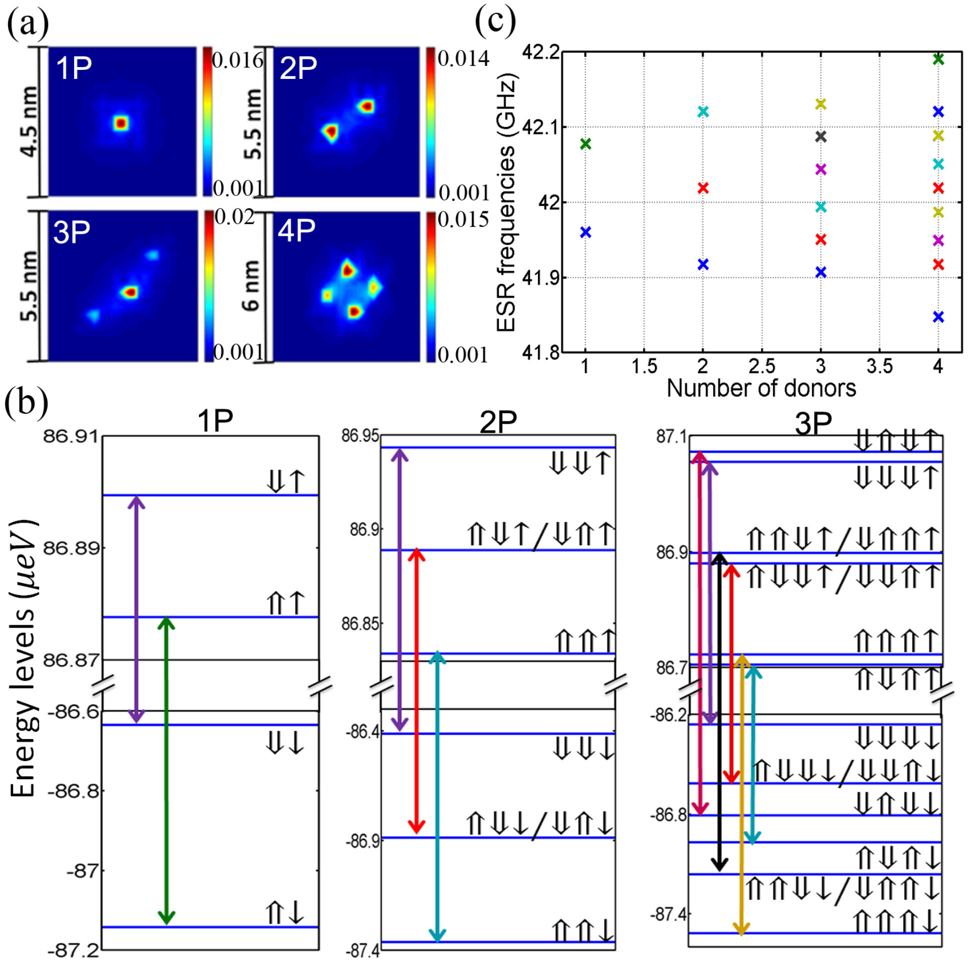

Fig. 2.2. Dependence of ESR spectra on donor number in donor-based quantum dots. (a) Single-electron probability density distribution of the ground states (in nm^{-3}). The four figures show the 1-4 P donor cases respectively. (b) The electron spin transitions of devices with 1-3 P donors corresponding to each spin configuration of electron ↑ or ↓ and nuclei ⇑ or ⇓. The thick (thin) arrows indicate the orientations of the nuclear (electron) spins. The ground orbital state energy without B-fields is the zero energy reference. (The 4P case follows the same routine and is not shown here as 2^5 spin configurations are involved.) (c) The ESR frequencies of devices with 1-4 P donors.

number of donors since the number of possible nuclear spin configurations increases. If the ac-B-field frequency can be controlled with enough accuracy, all the ESR peaks can in principle be observed. Comparing the number of measured peaks with the theoretical calculations of Fig. 2.2(c), it is possible to determine the number of donors in the quantum dot.

Not only are the number of ESR transitions important, but their locations and spacings in the frequency axis can also provide information about the locations of the the P donors and the number of bound electrons in the quantum dot. In the next section, we discuss the effect of the donor locations on ESR frequencies. The hyperfine couplings between the electron and the nuclear spins, which are proportional to electron probability density at each donor site, are quite sensitive to the relative donor locations within the quantum dot. The quantum confinement and hence, the on-site wavefunction concentrations strongly depend both on the radial and angular separation of the donors due to the crystal symmetry, even for ∼1-2 nm variations in quantum dot sizes. For the purpose of characterizing and operating qubits, it is not very important to know the exact location of the donors within the dot. However, it is beneficial to obtain some information of the extent of the electron wavefunction for the design of two-qubit gates [12] and to engineer long T_1 times [42]. Moreover, it is useful to obtain a range within which hyperfine couplings can vary given the number of donors in a dot.

In a STM patterned Si:P quantum dots, a lithographic patch defines a region where donors can be incorporated into the silicon crystal. The donors in reality can occupy different energetically favourable atomic sites within the patch, which provides some variations in hyperfine couplings between dots with the same number of donors. Here, we use 2P donor dots as an example to demonstrate how the hyperfine couplings and hence the ESR frequencies are correlated with donor separations within a 2P donor quantum dot. Fig. 2.3(a) shows four different 2P configurations within a lithographic patch on the silicon (100) plane, labeled as D1-D4. The black squares represent silicon atoms and the white filled circles represent the substituting P atoms on a (001) atomic plane of silicon crystal lattice. From left to right, the separation of the two donors are increased by a step of ∼3.84 angstroms in the [110] direction, from D1 to D4. And in the $[1\bar{1}0]$ direction, two donors are ∼3.84 angstroms apart, which is fixed for

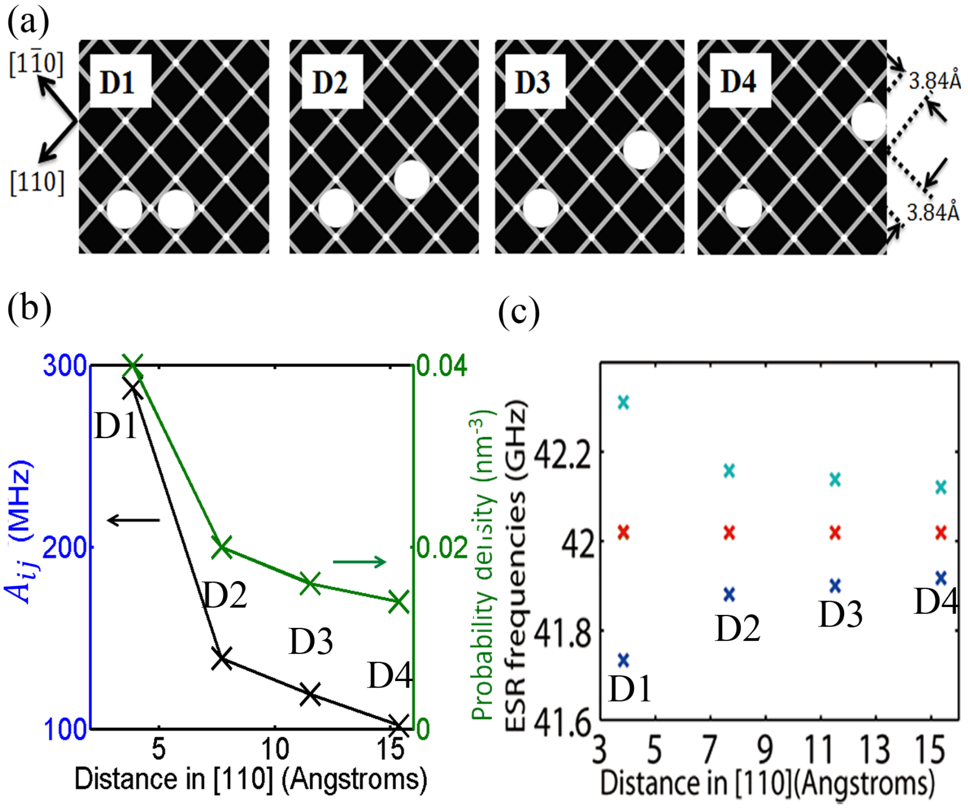

Fig. 2.3. Dependence of ESR spectra on donor separation with the donor-based quantum dot. (a) The four studied positional configurations of 2P donor-dots (D1-D4) respectively. The black squares represent silicon atoms and white filled circles represent the substituting P atoms on an atomic plane of silicon. The nearest-neighbor atoms are separated by ∼3.84 $\mathring{A}$ in the [110] or [1$\bar{1}$0] direction. (b) The Fermi contact hyperfine constant A_{ij} as a function of two donor separation in [110] corresponding to (a). (c) The impact of variations in the Fermi contact hyperfine couplings on the ESR frequencies of D1-D4 cases in (a). Here we find variations in ESR frequencies up to ∼190 MHz.

all the four cases. The right y-axis of Fig. 2.3(b) shows that the on-site electron probability density decreases with the distance between two donors. This will lead to a decrease in hyperfine coupling with the distance, which is shown as the left y-axis in Fig. 2.3(b). Fig. 2.3(b) gives the values of Fermi contact hyperfine coupling (A_{ij}) of one of the two donors, in which the other shares the same value because of symmetry.

Fig. 2.3(c) shows the corresponding ESR frequencies of these four configurations. We note the ESR frequencies are farther apart when the donors are closer spatially. The results provide valuable information about the extent of the electron wavefunctions in devices where we have the same number of donors but different donor locations.

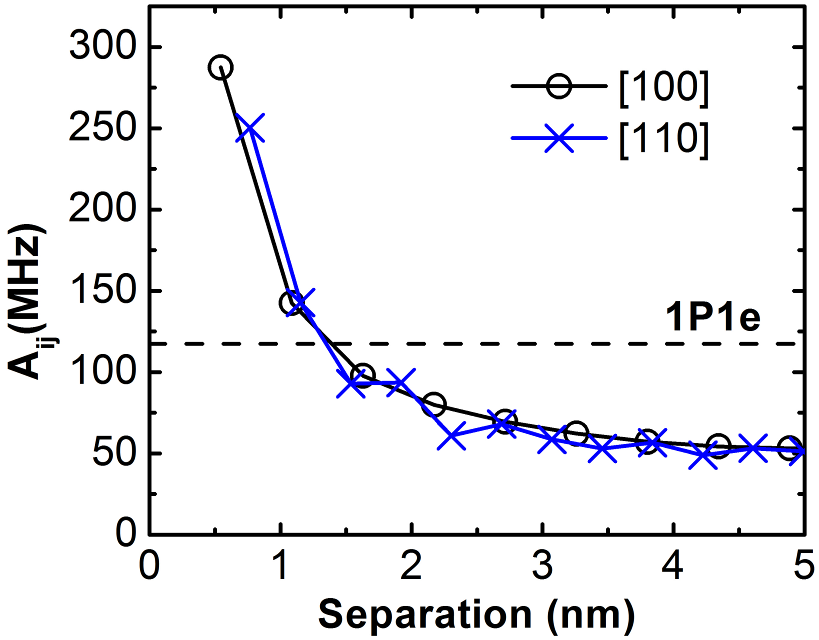

Fig. 2.4. Impact of inter-donor separation along the [100] and the [110] direction on the Fermi contact hyperfine coupling A_{ij} of a donor dot. The horizontal dashed line represents the hyperfine coupling of a single P donor in bulk silicon, which is ∼117.53 MHz.

Effects such as dopant diffusion and segregation can often cause the precisely placed donors to occupy lattice sites outside the lithographic patch. To account for this scenario, we explore the hyperfine interaction of a P donor pair for larger radial separations along two high symmetry directions in the plane. Fig. 2.4 shows the Fermi contact hyperfine coupling A_{ij} as a function of inter-donor separation along the [100] (circles) and the [110] direction (crosses). In the [100] direction, A_{ij} first decreases from 287.4 MHz to 57.1 MHz from a separation of ∼0.54 nm to ∼3.8

nm, and smoothly levels off when the separation is larger than 4 nm. A very close separation distance increases the quantum confinement of the electron wavefunction as the potential of the two donors enhance each other significantly near the donor cores. Here the electron density from the outskirts of the dot is redistributed to the central region forming a strongly hybridized molecular state, thereby enhancing the hyperfine coupling.

When the separation is even larger ($>\sim$5 nm), the two P donors approach the regime of two isolated bulk-like donors with A_{ij} converging to about half of the bulk value of 117.53 MHz, as the two donors still share one electron. This is in contrast to the case of two far separated donors with one electron each where A_{ij}=117.53 MHz. In the [110] direction, A_{ij} can be seen to oscillate as a function of separation due to the interference between the wavefunctions of the six conduction band valleys of silicon, similar to the predicted exchange oscillations [18]. From Fig. 2.4 we can see that A_{ij} of a P-donor pair in silicon with one bound electron can vary from ∼287.4 MHz to ∼48.9 MHz within a 5 nm separation range.

Next, we evaluate the ESR frequencies of the donor-based quantum dots for multi-electron occupation. As discussed earlier, the resultant hyperfine coupling in a donor dot originates from the unpaired electronic spin of the outermost electron. In such a case, the unpaired electron is screened from the positively charged donor cores by the spin-paired electrons of the inner orbitals, and the wavefunction spreads out more in space causing a reduction in the density at the nuclear sites in the central region. This causes a sharp decrease in the Fermi contact hyperfine coupling as more electrons are loaded. Note that, by referring to spin-paired inner electrons, we are still referring to the extra electrons in the donor molecules that do not take part in the covalent bonds with the nearest silicon atoms as these bonds remain intact in the donor-dot.

In Fig. 2.5(b), we show the ESR frequencies for 1 and 3 electrons on a 2P donor dot, assuming the D4 positional configuration of Fig. 2.5(a) in which the donors are separated by ∼1.5 nm in the [110] direction. Fig. 2.5(a) shows the probability density distribution of the 3rd electron solved with Hartree self-consistent field approximation

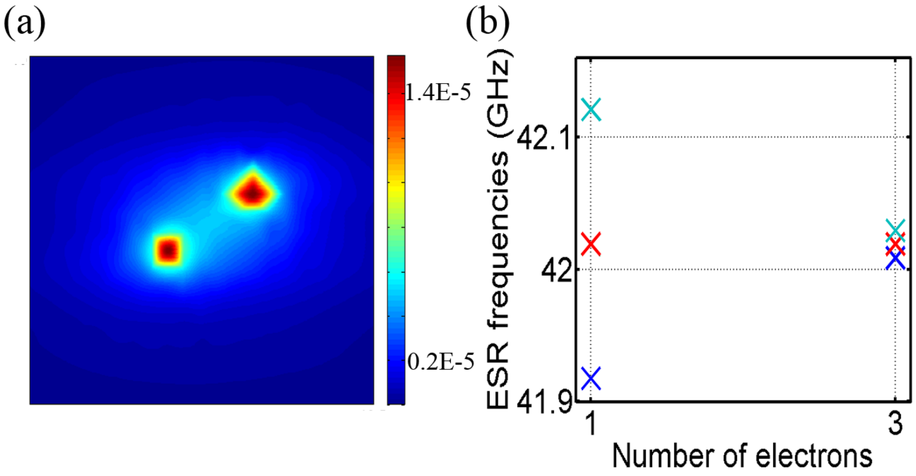

Fig. 2.5. Impact of multi-electron occupation in a donor-dot on ESR frequencies. (a) Single-electron probability density distribution of the 3^{rd} electron in D4 with Hartree self-consistent field solution (in nm^{-3}). (b) The ESR frequencies of the 3^{rd} electron in D4, compared with the case of only 1 electron in D4 (shown as the 2^{nd} figure in Fig. 2.2(a)).

as illustrated in the methodology section. It has a larger extent and lower on-site concentrations compared with the single-electron probability density of D4 (shown as the 2^{nd} figure in Fig. 2.2(a)). With two more electrons, consequently the Fermi contact hyperfine coupling decreases to 10.5 MHz from 101.8 MHz. Correspondingly, the ESR resonance peaks of Fig. 2.5(b) are closer to each other if the number of bound electrons in a given donor-dot is larger. Interestingly we observe the effect of multi-electron occupation in hyperfine coupling reduction (a factor of $\sim$10) is more prominent than increasing the inter-donor distance up to $\sim$1.5 nm within the dot (a factor of $\sim$3, Fig. 2.3(b)). Therefore, the electron number in a donor quantum dot can also be detected with this metrology. To summarize the metrology, the number of ESR frequencies indicates the number of donors within a quantum dot, and the separations between the ESR frequencies imply the bound electron number and inter-donor distances.

Lastly, we investigate the effect of electric field (E-field) from a top gate, as in the typical Kane proposal [5, 6, 35], on the ESR spectra of Si:P quantum dots. The Si:P

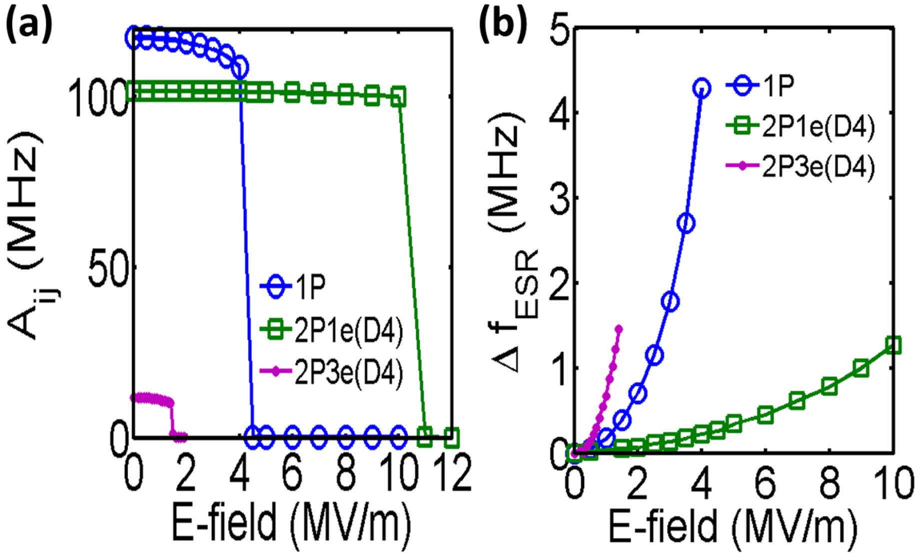

Fig. 2.6. Electric field dependence of (a) Fermi contact hyperfine couplings A_{ij} (b) shift of ESR frequencies Δf_{ESR} with all nuclear spins $\Uparrow$.

quantum dots are placed ∼15 nm below the Si/SiO$_2$ interface (see Fig. 2.1(a)). As can be seen in Fig. 2.6(a), the change in the hyperfine couplings due to the electric fields is quite small for 1P (∼9 MHz) and almost negligible for the 2P cases before the bound electron is ionized (where A_{ij} suddenly goes to 0). The corresponding shift in the ESR frequencies Δf_{ESR} (Fig. 2.6(b)) is ∼4 MHz for the 1P case and ∼1 MHz for the 2P cases up to the ionization fields. Here we assume all the nuclear spins are in their lowest-energy configurations (all $\Uparrow$). Therefore the E-field induced shifts in the ESR frequencies are not comparable to the separation of the ESR frequencies, which are in the order of ∼100 MHz for the 1P and 2P1e cases, and ∼10 MHz for the 2P3e case as shown above. This is because the electron wavefunction is strongly confined in a donor dot qubit and spatially small. The typical Bohr radius is 1-2 nm. As a result, the wavefunction is not so sensitive to electric fields given by the top gates, so are the hyperfine interactions and the ESR spectra, because the fraction of electron wavefunction pulled away from the dot (toward the interface) is almost negligible. For STM-patterned devices, the electric fields can also be applied laterally with in-plane gates. We have shown in our previous work [10] that the stark shift of hyperfine interaction of a 2P dot is ∼10 MHz, and even smaller for a 3P dot with lateral electric fields up to 7 MV/m. Therefore, the Stark shift in the ESR frequencies does not play a significant role in the metrology proposed in this work. Moreover, the shift is predictable and can be accounted for when characterizing a realistic device under gate biases.

2.4 Conclusion

We have proposed a metrology technique to characterize spin qubits hosted by Si:P quantum dots in silicon. The metrology can help extract information about the number of donors, donor locations and the number of electrons based on ESR measurements, and is potentially more accurate than charging energy based metrology. An atomistic tight-binding method is coupled with a Hartree self-consistent field approach to obtain the orbital wavefunctions of multi-donor quantum dots in silicon. Solving a multi-spin Hamiltonian with parameters computed from the wavefunctions enable us to predict ESR transition frequencies for the Si:P quantum dots. We found that the number of ESR frequencies increases with the number of donors, while the locations and the spacings of the ESR peaks on the frequency axis can help extract information about the spatial extent of the donors within the quantum dot and the number of bound electrons. The extracted information is useful for engineering single and multi-qubit operations in a system with very long coherence times. The method proposed here may also be applied to obtain information about other $\frac{1}{2}$-spin qubit systems like phosphorus donors in germanium, or non-$\frac{1}{2}$-spin qubit systems, for example, arsenic/boron dopants in silicon, and potentially on dopants in other semiconductors.

3. ENGINEERING EXCHANGE INTERACTION BETWEEN DONOR-BASED QUBITS

The work in this chapter including appendices A, B and C is published in Ref. [12], and the text is taken from there.

3.1 Introduction

In this chapter, we introduce an alternate design for an exchange gate in a two-qubit donor system, which allows flexibility in device fabrication and in tuning the exchange coupling. In principle, this new design can 1) eliminate the need for additional J-gates between the donors, 2) function with a range of donor separations, 3) provide a ∼5 orders of magnitude J-tunability within a modest E-field range of ∼3 MV/m and lowered 'Off' state exchange, and 4) mitigate the J-oscillations with donor separations. This design can also benefit from improved addressability [10] and longer T_1 times [42], and can be used in conjunction with the two-qubit scheme proposed in Ref. [45]. This design can therefore overcome some of the experimental obstacles for realizing a two-qubit gate in silicon. To perform these state-of-the-art calculations of exchange energy in donor qubits, we have combined atomistic full band electronic structure calculations, electrostatic device simulations of experimentally realizable device architecture, and a two-electron full configuration interaction (FCI) technique over a lattice of 1.7 million atoms. The calculations therefore describe the detailed two-electron spectrum of donor qubits over large E-field ranges accounting for both crystal effects and electron-electron exchange and correlation effects [46].

By studying double quantum dots (DQD) in silicon [14], we find that an asymmetric 2P-1P system outperforms the symmetric 1P-1P system in exchange controllability with detuning gates. Analogous to exchange-tuning in a DQD [47, 48], we envision a

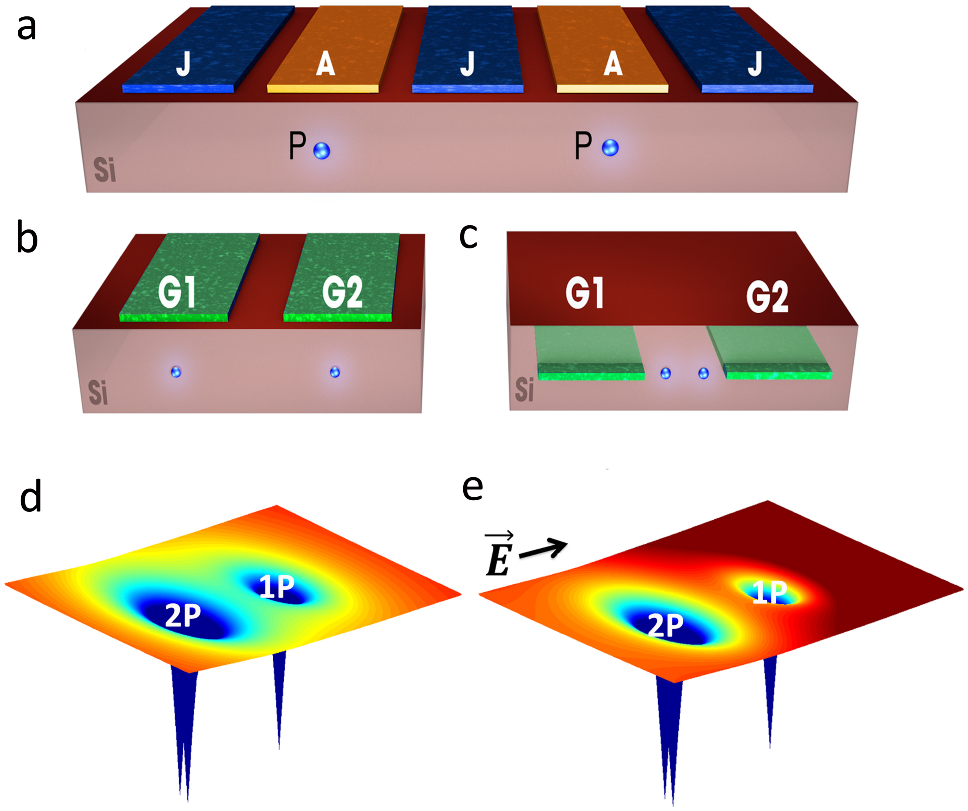

Fig. 3.1. Control of exchange in donor based qubits separated by ∼15 nm. (a) Kane's two-qubit donor device with J-gate [5]. (b) A MOS device with top detuning gates. (c) An STM patterned device with in-plane detuning gates. (d),(e) schematic potential energy profiles of the two-qubit system without and with the detuning electric field $\vec{E}$, showing a tilt in potential energy along the separation direction in (e).

(1,1) to (2,0) charge transition [49] in both 1P-1P and 2P-1P qubits as a function of a lateral electric field which provides the energy detuning. As the electron bound to one donor is pulled to the other by the electric field, the exchange coupling can be engineered from a small value in the (1,1) state to a large value in the (2,0) state due to the large spatial overlap of the wavefunctions in the latter. Such an electric field can be applied from either top gates (see Fig. 3.1b) in a metal-oxide-semiconductor (MOS) device or from in-plane gates realized by scanning tunneling microscope (STM) based lithography (see Fig. 3.1c) [14]. Placed on either side of the donor qubits, the detuning gates eliminate the need for a sensitive tunnel barrier control by the J-gate. Instead, this design realizes a tilt in the potential landscape of the two qubits, as shown in Fig. 3.1d and e, and therefore relaxes the more stringent engineering requirements of donor separations and gate widths of the Kane architecture, leading to a reduced overall gate density in the computer.

3.2 Methods

Previous works have calculated the exchange energy between two donor-bound electrons in silicon as a function of separation R using the effective mass approximation (EMA) and the Heitler-London (HL) formalism [18, 50], which is valid in the regime of small wavefunction overlap ($R > 5$nm). Control of exchange with the Kane J-gate was also calculated in Ref. [50, 51] from EMA based HL method. However, this method becomes inaccurate at modest gate biases when the wavefunction overlap increases. The HL method also ignores contributions of doubly excited configurations that increase with reduced separations or increasing fields. More recently, the exchange coupling was calculated in a 1P-1P system from EMA based molecular orbital and configuration interaction approaches for separation distances larger than 7.5 nm [53] and modest electric fields [54]. All these works are based on the Kohn-Luttinger form of the donor wavefunctions [55], which provides a very specific solution to the two-electron problem, and cannot provide a full description of the (1,1) to (2,0) charge transition in which strong Stark effect causes mixing of the lowest states with many excited states [56]. The atomistic configuration interaction method used here goes beyond these approximations to include the Stark effect, large wavefunction overlap and electron-electron exchange and correlations. In this work, we employ a large scale atomistic tight-binding (TB) method that describes the crystal as a linear combination of atomic orbitals, and captures the full energy spectrum of a donor in silicon including the conduction band valley degrees of freedom, the valley-orbit interaction [57], the Stark shift of the donor orbitals [56], and real and momentum space images of the donor obtained by STM experiments [40]. Using the atomistic wavefunctions, we compute the two-electron states of donor and donor-clusters in the presence of an electric field from a FCI technique. The same method has been successful in solving the challenging problem of the D^- state (the two electron state of a single donor) without any fitting parameters and providing a charging energy of 45 meV [58] compared to the 44 meV experimental value [41]. The method is described in detail in Appendix A.

The FCI technique is an exact way to solve the multi-electron problem only limited by the number of one electron basis functions used. The method diagonalizes the multi-electron Hamiltonian in the basis of all Slater determinants (SD) constructed from the single electron states of the system. Each SD represents a multi-electron anti-symmetric wavefunction for a particular arrangement of the electrons among the basis orbitals. In addition to the ground state, the method also captures the excited multi-electron spectra. The exchange coupling J in the two-electron case can be obtained from the difference between the lowest triplet energy (E_T) and singlet energy (E_S) divided by the Planck's constant h, as $J = \Delta E_{ST}/h = (E_T - E_S)/h$ [48].

3.3 Results

In Fig. 3.2a we show the computed exchange coupling between two donor bound electrons as a function of donor separation along two high symmetry crystallographic directions [100] and [110]. We consider two cases: 1) a symmetric two-qubit system of 1P-1P [5] (black triangles and squares), and 2) an asymmetric two-qubit system of 2P-1P along the lines of Refs. [10, 14] in which we consider two representative locations of the donors inside the 2P cluster, shown in Fig. 3.2b as 2P(A) and 2P(B). The exchange coupling as function of 2P-1P separation for these two spatial configurations of the 2P cluster are labeled as 2P(A) (blue curves) and 2P(B) (magenta curves) in Fig. 3.2a. In Fig. 3.2b, the squares represent the silicon atoms on the (001) plane and the filled circles represent the substituting P atoms. In all the cases, the exchange coupling decreases exponentially with increasing separation in both the [100] and the [110] directions, attaining ∼1,000 GHz for separation ∼5 nm and a few tens of MHz for ∼15 nm. This is expected since the wavefunction overlap between the qubits decreases as the separation increases.

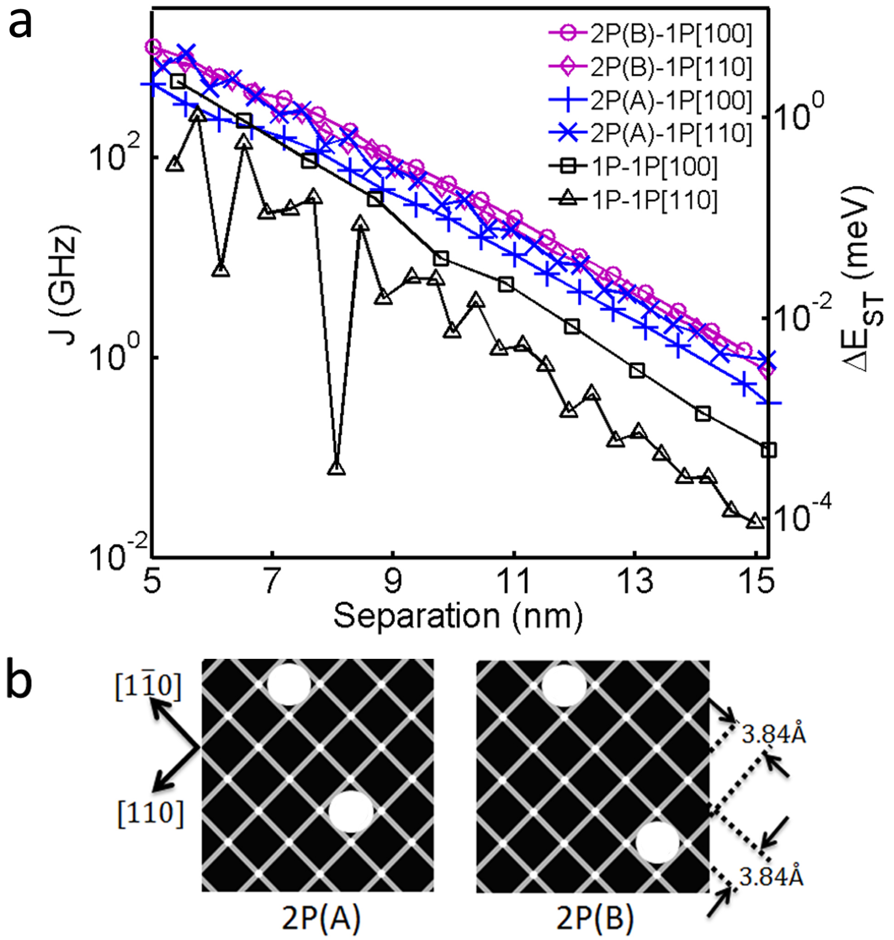

Fig. 3.2. Separation dependence of exchange coupling. (a) The exchange coupling of 1P-1P and 2P-1P qubits in silicon as a function of inter-qubit separation along the [100] and [110] crystallographic axes without any applied electric fields. (b) Two studied 2P cases with different donor locations on a (001) plane in silicon. The squares are the silicon atoms on the (001) atomic plane and the filled circles are the substituting P atoms.

The exchange coupling of the 2P-1P qubits are found to be slightly larger than the 1P-1P qubits even without an electric field. This is somewhat counter-intuitive considering the fact that a 2P system provides a stronger confinement for the electron and should minimize the overlap with the 1P electron. However, due to the asymmetry of the confinement potential, the 2P cluster is already slightly detuned towards the (2,0) state with larger wavefunction overlap, resulting in a larger exchange. The exchange can be reduced below the 1P-1P value due to the smaller Bohr radius of the 2P wavefunction in this case by applying a negative detuning bias, as shown later.

The exchange coupling of the 1P-1P qubits in the [110] direction (black triangles) exhibit oscillations as a function of donor separation. This has been observed in earlier works based on the Kohn-Luttinger effective mass HL method [18,50], and has been attributed to the interference between the wavefunctions of the six conduction band valleys of silicon. In the [100] direction, we don't observe the J-oscillations as predicted by the Kohn-Luttinger effective mass theory, which is consistent with Ref. [52] due to effective mass anisotropy captured by our atomistic tight-binding method.

It is interesting to note that the J-oscillations are strongly mitigated in all the 2P-1P cases along both [100] and [110] separation. In fact, we considered two different 2P cluster configurations, 2P(A) and 2P(B) to verify this. In 2P(A), the intra-cluster P donors are separated by a_0 times an integer in both [100] and [010], and in 2P(B) by $a_0/2$ times an odd integer. These two cases are thus representatives of the donors separated by a whole unit cell and a half unit cell. Relative to this 2P cluster, if the 1P distance is varied along [100] or [110], the J-oscillations should appear in analogy with the 1P-1P system. However, as shown in Fig. 3.2a, we observe strongly suppressed J-oscillations in all the 2P-1P cases due to a number of factors such as reduction of Bohr radius, valley repopulation, and contribution of excited orbital states, which are analyzed in more detail in the Appendix B. Hence, the 2P-1P unit is a more fault-tolerant system for fabrication and control than the 1P-1P unit.

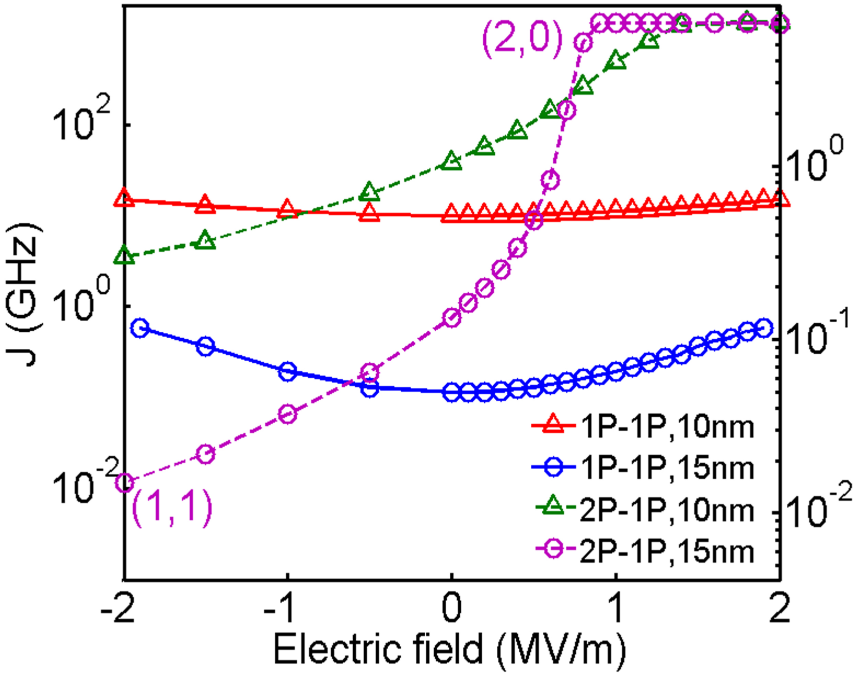

Fig. 3.3. Electric field induced exchange in donors. Exchange energy as a function of an electric field along the separation axis for a 1P-1P and a 2P-1P system with inter-dot separations of 10 nm and 15 nm. The 2P(B) configuration is used (shown in Fig. 3.2b).

Now that we have explored the range of exchange energies that can be accessed in donor qubits for various donor separations, we investigate the electric field control of exchange in the 1P-1P and 2P-1P systems. Fig. 3.3 shows the exchange energies as a function of the electric field for 10 nm and 15 nm qubit separations respectively. We consider an electric field range of -2 to 2 MV/m, consistent with typical E-fields realized in STM patterned donor devices. In general, the exchange curves show a transition from a low value to a large value for a charge transition from (1,1) to (2,0) for the 2P-1P curves. This is because when the two electrons are localized on separate qubits, the spatial overlap of the wavefunction is small, and so is the J coupling. Since a 2P-1P system is slightly detuned toward the 2P cluster at zero field, a negative electric field further decreases the wavefunction overlap so that the exchange coupling is decreased. A positive field pulls both the electrons gradually to one qubit, such that the spatial overlap increases, and so does the exchange. In the extreme (2,0) regime when both electrons are on the left qubit, the electric field has little effect on the overlap, and the exchange coupling levels off. For the 2P-1P exchange curve at a 15 nm separation, the exchange coupling is observed to vary from 11.6 MHz to 1,310 GHz over a field range of -2 to 0.9 MV/m, resulting in over five orders of magnitude tunability. The 'Off' state (at -2 MV/m) is ∼1 order of magnitude lower than that of the 1P-1P case at a 15 nm separation (the circled blue curve at 0 MV/m).

We note that within the 2 MV/m field range, only the 2P-1P cases exhibit significant exchange tunability in Fig. 3.3. The 1P-1P case only shows a change from 113.4 MHz to 578.6 MHz (5 times) over 2 MV/m for a 15 nm separation distance. Since the 2P cluster has two core nuclear charges with one bound electron, it is easier to shuttle an extra electron to this system aided by the net attractive potential of the core. In the 1P-1P case, the electron-electron repulsive energy is stronger due to the charge neutrality of each qubit, and a larger E-field is needed to reach the (2,0) regime. The calculations show that for $E< 2$ MV/m, the (2,0) regime is never reached in the 1P-1P case if the separation is less than 15 nm. In addition, since such a system is symmetric, either a positive or a negative field will increase the exchange coupling. It can be seen that qubit pairs with larger separations exhibit larger tunability. This is because the same electric field causes a larger potential drop between the qubits if their separation is larger, and hence provides a larger detuning energy. We also note that the exchange curves show that the transition to the (2,0) regime is smoother if the separation distance is less. This is due to the stronger molecular hybridization of closely spaced qubit pairs.

After comparing the 1P-1P and 2P-1P cases in Fig. 3.3, one can see that a 2P-1P system with a 15 nm separation provides a promising two-qubit unit of a silicon quantum computer, yielding 5 orders of magnitude exchange tunability. In our simulations with uniform electric fields, we are unable to go to the high field regime for the 1P-1P case, as high fields induce a triangular quantum well at the lateral domain boundaries causing electron localization in the surface states [56]. However, larger exchange energies can possibly be realized even in the 1P-1P case with large spatially varying E-fields from detuning gates as shown in Fig. 3.1b and c. In Appendix C, we show that the exchange coupling of a 1P-1P system can be tuned by a factor of 50 using surface detuning gates. We also compare the exchange tunability of corresponding cases to the original Kane architecture with J-gate and show the proposed detuning scheme in this manuscript is superior. These simulations include electrostatic simulations with the Sentaurus technology computer-aided design tool (TCAD) [59] coupled to the TB-FCI method.

We now study the promising 2P-1P system for a 15nm separation in more detail including the two-electron energy spectrum and the singlet and triplet wavefunctions at various electric fields. Fig. 3.4a demonstrates the two-electron total energies of several lowest singlet (black curves) and triplet (blue curves) states as a function of the electric field, relative to the top of the valence band energy at the midpoint of the two qubits. The lowest black solid lines are the (1,1) and (2,0) singlet states. They mix at low electric fields and anti-cross at ∼0.7 MV/m, which marks the symmetry point of the (1,1) to (2,0) charge transition. The lowest (1,1) triplet state represented by the blue dotted line has little dependence of the electric field until 0.9 MV/m, indicating that it is decoupled from other triplet states. A sharp transition occurs at 0.9 MV/m, beyond which the energies of singlet and triplet states have a linear dependence on the electric field, indicating the occupation regime of a (2,0) charge configuration where the lowest states of the two qubits are no longer tunnel-coupled.

Fig. 3.4b shows the weight of the lowest (2,0) Slater Determinant $|L_0{\uparrow}L_0{\downarrow}\rangle$ in the ground state singlet of the 2P-1P system as a function of the electric field. As can be seen, the weight changes from a small probability $3{\times}10^{-6}$ to ∼1, indicating a charge transition from (1,1) to (2,0). This (2,0) probability can be measured by a charge sensor, as in experiments with DQD based singlet-triplet qubits [47, 60]. Thus the

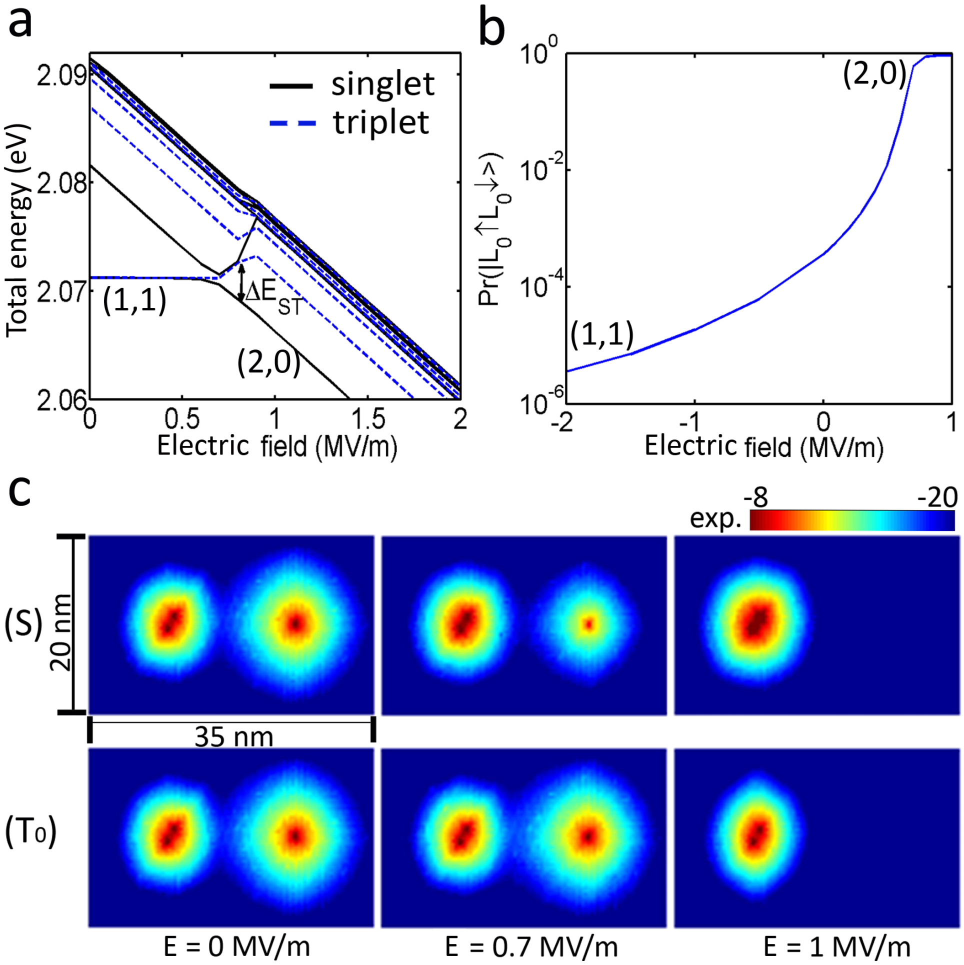

Fig. 3.4. Electric field dependence of singlet and triplet states. (a) The total energy of the lowest few singlet and triplet states of a 2P-1P system with a 15 nm inter-qubit separation as a function of electric field. (b) Probability of the (2,0) state with both electrons on 2P as a function of electric field. (c) Two electron density of the lowest singlet (S) and triplet (T_0) states at three electric field values, showing a transition from (1,1) to (2,0).

same control scheme of Ref [47] can be utilized to realize singlet-triplet based donor qubits with electrical manipulation of J.

In Fig. 3.4c, we show the two-electron density of the lowest singlet and triplet states computed from the FCI wavefunctions at three different E-fields. At $E = 0$, the singlet and triplet states look similar as they are both in the (1,1) charge configuration.

The stronger confinement in the 2P cluster on the left is responsible for a smaller wavefunction extent. At $E = 0.7$ MV/m, the (1,1) singlet mixes with the (2,0) singlet and the electron density gradually shifts to the 2P cluster. However, due to spin blockade, the triplet still remains in the (1,1) configuration, with almost negligible change in the wavefunction. At high enough electric fields of 1 MV/m, both the singlet and the triplet are in the (2,0) regime, as verified by the electron densities being localized in the 2P cluster.

3.4 Discussion

In summary, we have shown that a detuning gate control of the J-coupling in donors can relax the stringent requirements of including additional J-gates to control the exchange coupling needed to realize a two-qubit gate in silicon. In addition, the use of an asymmetric 2P-1P qubit pair can yield tunability of the exchange by 5 orders of magnitude over a modest field range (3 MV/m) with an even lower 'Off' state exchange than the corresponding 1P-1P qubits. Combined with long T_1 times of donor clusters [42], improved addressability of 2P-1P qubits [10], and operation schemes of Ref [45], the proposed design helps in the experimental realization of the much sought after two-qubit gate with donors in silicon. The calculations of detuning controlled exchange coupling also helps in realizing highly tunable singlet-triplet qubits [47].

4. ELECTRICAL CONTROL OF DONOR-BASED SPIN QUBITS IN SILICON

The work in this chapter including appendix D is published in Ref. [19], and the text is taken from there.

4.1 Introduction

Controlling individual electron spins is of great importance for donor-based quantum computation. Manipulation of electron spins with integrated microwave antenna has been demonstrated in both donor and gate-defined quantum dot qubits with long coherence and high gate fidelity [4, 44]. However, it is challenging to use an ac magnetic field to realize local spin control for many qubits, a crucial requirement for multi-qubit operations in a scalable quantum computer architecture. We also know that a microwave antenna can introduce deleterious noise to the coherence of a qubit [44]. An alternative way to spin control is to utilize an oscillating electric field, which has been demonstrated in quantum dot systems [3, 61, 62]. Here, the qubit is modulated periodically by the difference in Zeeman energy caused by either non-uniform electron g-factor, external magnetic field or hyperfine couplings [47, 63, 64]. To date, all-electrical control of spins without a microwave magnetic field in donor systems in silicon has not been demonstrated.

In this chapter, we propose all-electrical control of donor-based spin qubits taking advantage of the hyperfine coupling difference between single donor and few-donor quantum dots by introducing ancillary dots (The device schematic is shown in Fig. 1(a) and (b) with “P” denoting phosphorus donors). The electron and the 3 nuclear spins (of 2P + 1P atoms) in the dashed box in Fig. 1(b) define the single-qubit operation space, and the information is encoded in the electron spin. Here the ancillary dot

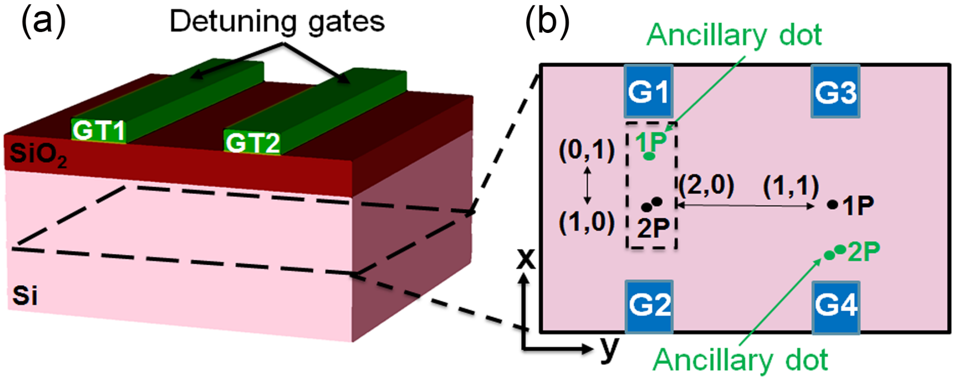

Fig. 4.1. Electrical control of donor-based spin qubits. (a) The pink box denotes the silicon substrate. The two gates shown in green (GT1 and GT2) are the surface detuning gates for controlling two-qubit exchange interaction. The dashed contour indicates the plane that contains the central device components (as shown in (b)). (b) The blue rectangles represent the in-plane gates (G1-G4) to induce the (1,0) and (0,1) [49] transitions for single-qubit operations. The (2,0) and (1,1) transition is controlled by the surface gates (GT1 and GT2) in (a) for two-qubit operations.

(1P in green) creates a difference in the local hyperfine coupling between the 1P and 2P dots due to the different number of nuclei and asymmetric quantum confinement in the dashed box [11]. The (1,0)↔(0,1) [49] charge transition between them can be controlled by the pair of in-plane gates G1 and G2. An electric dipole can thereby be induced by biasing the system near the (1,0)–(0,1) charge degeneracy point, where the hyperfine couplings can be modulated with an ac electric field on top of the dc electric field from the in-plane gates G1 and G2 to drive the electron spin transition.

In this proposed approach, the donor dots can be placed with atomic precision far from interfaces or surfaces using an STM based lithography technique, making them less prone to noise sources close to the interface [66–69]. Using Coulomb confined states leads to higher valley and orbital states that are not accessible as they are typically at least 10 meV above the ground state. This results in well-isolated states of operation within which the qubit coherence can be boosted. Moreover, this scheme could be realized with existing circuitry in STM-patterned devices [14, 65] without introducing extra control components. The donor dots can be coupled via the exchange interaction (e.g. the (1,1)↔(2,0) transition in Fig. 1(b)) controlled by the surface detuning gates GT1 and GT2 (Fig. 1(a)), retaining the highly tunable exchange coupling [**?**] and allowing fully electrical two-qubit operations. This design can be potentially extended to a scalable quantum computer architecture by repeating the fundamental structure (Fig. 1(a) and (b)) according to the requirements of the large-scale architecture [7, 70].

4.2 Methods

In the following, we describe the spin and charge evolution in the 2P-1P system by an effective Hamiltonian with quantitative details. The effective Hamiltonian can be expressed as:

$$H = H_e + H_T + H_{Z_e} + H_{Z_n} + H_{HF}, \tag{4.1}$$

with the basis $|s, i_1 i_2 i_3, d\rangle$ including spin and charge information, where we denote $s = \uparrow, \downarrow$ as electron spin, $i_j = \Uparrow, \Downarrow$ (j = 1,2,3. See Fig. 2(a)) as the three nuclear spins, and $d = 2P, 1P$ as the specific dot site (e.g. $|\downarrow, \Uparrow\Uparrow\Uparrow, 2P\rangle$ is the lowest energy configuration). H_e reflects both the on-site energy detuning and the applied ac electric field, which is expressed as:

$$H_e = \sum_{d=1P,2P} (\epsilon_d + e\vec{E_{ac}} \cdot \vec{R})|d\rangle\langle d|, \tag{4.2}$$

where ϵ_d is the on-site detuning energy, and d is the dot index (1P or 2P). e is the elementary charge, $\vec{E_{ac}}$ is the ac electric field, and $\vec{R}$ is the separation between the 2P and the 1P dot. The second term represents the tunnel coupling between the (1,0) and (0,1) charge states of the 2P and the 1P dot:

$$H_T = \sum_{d \neq d'} t_c |d\rangle\langle d'|, \tag{4.3}$$

where t_c denotes the tunnel coupling between the two donor dots. d and d' denote different dot indexes. The third and the fourth term denote the Zeeman energy of the electron spin and the nuclear spins:

$$H_{Z_e} = g_e \mu_B \vec{B} \cdot \vec{S}, \tag{4.4}$$

$$H_{Z_n} = \sum_j g_n \mu_B \vec{B} \cdot \vec{I_j}, \tag{4.5}$$

where g_e and g_n are the electron and nuclear g-factors respectively. μ_B and μ_n are the Bohr magneton and the nuclear magneton respectively. $vecS$ denotes the electron spin operator, and $\vec{I_j}$ denotes the spin operator of the jth nucleus.The fifth term gives the hyperfine coupling between the qubit electron and donor nuclei:

$$H_{HF} = \sum_j A_j \vec{I_j} \cdot \vec{S}, \tag{4.6}$$

where A_j is the Fermi-contact hyperfine coupling between the qubit electron and the jth nucleus.

To provide quantitative guidelines for exploiting this proposal, it is important to obtain the parameters in H, the tunnel coupling t_c, Fermi contact hyperfine couplings A_j, with sufficient accuracy. Here we model the system using an atomistic tight-binding approach to obtain the Stark-shifted electron wavefunctions, from which tunnel couplings t_c, hyperfine couplings A_j and their electric field dependency can be extracted [11, 34, 35]. In the tight-binding approach, the atoms are represented by $sp^3d^5s^*$ atomic orbitals with spin-orbit coupling and nearest-neighbor interactions. Each donor is represented by a Coulomb potential screened by the dielectric constant of silicon and an on-site constant potential for the Coulomb singularity, calibrated with the P donor energy spectrum [39]. The donor ground-state wavefunction obtained from this approach agrees well with the recent STM imaging experiments [40]. This physics-based approach automatically includes silicon conduction band valley degrees of freedom, and captures valley-orbit interaction [57] and Stark effect in donor orbitals [35]. The experimentally spin relaxation times of a single P donor and few-donor dots can also be reproduced with our approach [42]. This provides us confidence in accurately extracting the parameters t_c and A_j under realistic electric fields.

4.3 Results and Discussions

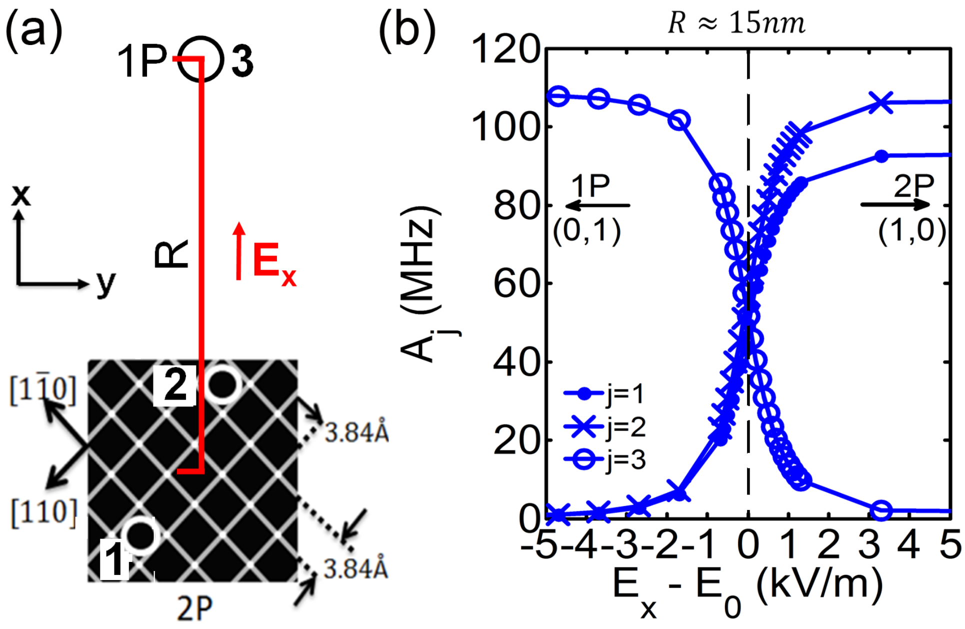

Fig. 4.2. Electric field dependence of hyperfine couplings. (a) The black squares represent the silicon atoms on a (001) atomic plane and the open circles represent the substituting P atoms. The ancillary 1P dot is placed away from the center of the 2P dot along the equivalent [010] crystallographic direction (the x direction) by R. The nuclei associated with the three donors in the system (in the dashed box in Fig. 1(b)) are labeled as 1, 2 and 3. (b) The hyperfine couplings associated with each nucleus as a function of electric field E_x for R ≈15 nm. $E_0 = 4963.3$ kV/m.

Fig. 4.2 shows the modulation of the hyperfine couplings (A_j) between the qubit electron spin and the nuclear spins of the P donors (2P + 1P) with electric field, with j=1,2 labeling the nuclei of the 2P dots respectively and j=3 labeling the nucleus of the 1P dot. The detail of the system in the dashed box in Fig. 1(b) is depicted as Fig. 2(a), where an atom configuration of the 2P dot is shown at the bottom. An in-plane external electric field (E_x) between G1 and G2 applied along the direction between the 2P dot and its ancillary 1P dot can detune the system and redistribute the electron wavefunction between them, thereby controlling the hyperfine couplings of the 2P and the 1P dots, as shown in Fig. 2(b). As can be seen, $A_3 \approx 0$ at $E_x - E_0 = 5kV/m$, and $A_1, A_2 \approx 0$ at $E_x - E_0 = -5kV/m$, indicating that the charge states (0,1) and (1,0) can be accessed with a small electric field range ($\sim$ 10 kV/m) with an inter-dot separation R≈15 nm. At $E_x \approx E_0$, the (1,0) and (0,1) charge states are degenerate, forming hybridized bonding and anti-bonding states. As observed, the hyperfine couplings (A_j) have a nearly linear dependence on the electric field near the (1,0)–(0,1) charge degeneracy point ($-1kV/m < E_x - E_0 < 1kV/m$), indicating that the hyperfine coupling difference between the 2P and the 1P dot has a linear response to the external electric field. Near the charge degeneracy point ($E_x \approx E_0$), an electric dipole transition can be driven by an ac electric field $\varepsilon_0 sin(\omega t)$ applied from G1 and G2, thereby causing the modulations of A_j with time. When the ac electric field is in resonance with the qubit energy splitting (solved from the static part of H in eq. (2.1)), the electron spin transition can be induced by the overall local hyperfine coupling difference [62, 71] between the 2P and the 1P dot. The emulation of this process in a 2P-1P system is now described by solving the time evolution based on the Hamiltonian in eq. (4.1).

We assume the system is initially in its lowest energy configuration and the electron is located at the 2P dot (at (1,0)), i.e. $|\downarrow, \Uparrow\Uparrow\Uparrow, 2P\rangle$, and assume the 2P dot configuration as shown in Fig. 2(a) with the 2P in one dot ≤1.5 nm apart. A static magnetic field B_0 is applied along the separation direction x. One of the possible ways to prepare the qubit in this initial state is to utilize the dynamic nuclear polarization technique [72] by repeatedly and selectively loading up-spin electrons to the donor dots [20] and emptying the dots to dynamically drive the nuclear spins up, then depleting the dots and loading a down-spin electron onto the dots in the end.

To achieve universal quantum gates, two-axis control of single qubits, i.e. Z-gate and X-gate, is needed. A Z-gate can be simply realized by applying the external static B-field. We will focus on X-gate in the following. As shown in Fig. 3(a), at the beginning of the control manipulation, an adiabatic in-plane gate bias between G1 and G2 is applied to ramp the static dc electric field up to and to keep it at $\sim E_0$, which is followed by a continuous ac electric field between the same gates. The X-gate rotation (the manipulation of $\downarrow \rightarrow \uparrow$ or $\uparrow \rightarrow \downarrow$) is then driven by the ac electric field if $h\gamma = \Delta E$, where ΔE is the energy difference between the two qubit states and γ is the frequency of the ac electric field. To be explicit, the qubit ground state is $\frac{1}{\sqrt{2}}(|\downarrow, \Uparrow\Uparrow\Uparrow, 2P\rangle - |\downarrow, \Uparrow\Uparrow\Uparrow, 1P\rangle)$, and the qubit excited state is a dressed state involving both electron and nuclear spins, which can be expressed as $\alpha(|\uparrow, \Downarrow\Uparrow\Uparrow, 2P\rangle - |\uparrow, \Downarrow\Uparrow\Uparrow, 1P\rangle) + \beta(|\uparrow, \Uparrow\Downarrow\Uparrow, 2P\rangle - |\uparrow, \Uparrow\Downarrow\Uparrow, 1P\rangle) + \zeta(|\uparrow, \Uparrow\Uparrow\Downarrow, 2P\rangle - |\uparrow, \Uparrow\Uparrow\Downarrow, 1P\rangle)$. A second adiabatic gate bias is then applied after the X-gate control is finished to bring the electron back to the 2P dot for spin storage. Here, we choose 2P over 1P because the electron spin relaxation time is longer in a 2P donor cluster than a single donor dot [42].

To achieve high-fidelity X-gate operation and make the system less prone to charge noise and relaxation, we need to make appropriate choices of the external B-field and the tunnel coupling. On the one hand, with regard to the external B-field, the qubit energy splitting ΔE can be expressed as $E_{Z_e} + \delta$, where E_{Z_e} is the electron Zeeman splitting, and δ includes the effects of nuclear spin Zeeman energies and hyperfine couplings, which contributes to an effective magnetic field in the order of mT. To form well-defined qubit states and suppress nuclear spin flip-flop, we need $E_{Z_e} >> \delta$ to hold the qubit state when no ac field is applied. As a result, the external B-field is required to be in the order of 0.1 T.

On the other hand, regarding the tunnel coupling, we need ΔE significantly smaller than $2t_c$ in order to make the higher anti-bonding states well separated from the lower qubit states, preventing state hybridization or excitation due to environmental noise. As an example, Fig. 3(b) shows the Rabi oscillations of the qubit electron spin under the driving ac electric-field under $\Delta E < 2t_c$ (B_0 = 0.5 T) and $\Delta E \approx 2t_c$ (B_0 = 1.45 T) for $R \approx 11.4$ nm, where the magnitude of the driving ac electric field is 15 kV/m, and its frequency is $\gamma \approx 14$ GHz which satisfies $\Delta E = h\gamma$. The ac electric field is assumed to be a single-frequency sinusoid. As shown, a full X-gate spin rotation can be achieved for $\Delta E < 2t_c$, while the X-gate fidelity (defined as $\max(\sum |\langle\Psi| \uparrow, i_1 i_2 i_3, d\rangle|^2))$ is diminished when $\Delta E \approx 2t_c$ due to the qubit spin-up state (solid blue curve in Fig. 3(a)) is hybridized with the upper anti-bonding spin-down state (dashed green curve). As a result, t_c needs to be engineered large enough. Fig. 3(c) show t_c as a function of the inter-dot separation R. As can be seen, t_c decreases exponentially as a function of R, because the wavefunction overlap of the 2P and the 1P dots decreases exponentially as R increases. To achieve $\Delta E < 2t_c$, if we choose B = 0.1 T, R needs to be larger than 15.6 nm approximately according to Fig. 3(c). If B = 0.5 T is chosen, R needs to be at least 13 nm.

In the following, we investigate the effect of R (or t_c) on the qubit coherence time. Both magnetic and charge noise can lead to qubit decoherence [73]. In the proposed design, magnetic noise can be suppressed to a large extent if the substrate is made of enriched Si-28. In addition, the microwave antenna that introduces magnetic noise [44] in the traditional magnetic qubit manipulation is excluded here. As a consequence, we mainly consider the effect of the charge noise from the charge fluctuations in the nearby gates on qubit coherence.

We investigate the decoherence time T_2^* possibly due to different types of charge noise from a single nearby in-plane gate, e.g. G1 in Fig. 1(b). T_2^* can be obtained using [74]:

$$\frac{1}{T_2^*} = \frac{e^2}{\hbar^2} \Big| \sum_{r_i = x,y,z} \langle\Psi_\uparrow|r_i|\Psi_\uparrow\rangle - \langle\Psi_\downarrow|r_i|\Psi_\downarrow\rangle\Big|^2 \cdot \frac{S_E(\omega)}{\omega}\bigg|_{\omega\to 0} \frac{2k_B T}{\hbar}, \tag{4.7}$$

where e is the elementary charge, $\Psi_\uparrow$ and $\Psi_\downarrow$ are the electron spin-up and spin-down molecular wavefunctions solved by the atomistic tight-binding method respectively, ω is the noise frequency and $S_E(\omega)$ is the noise field spectrum. For $S_E(\omega)$, we study $1/f^\alpha$ noise, Johnson noise and evanescent wave Johnson noise (EWJN) [75], assuming the noise source is 65 nm (the distance between G1 and the two dot center) away from the qubit system to be consistent with Ref. [65]. The expressions of the noise field spectra and the parameter estimations based on experiments [65, 76, 77] are also included in Appendix D.

Fig. 4.4(a) demonstrates the decoherence rate $1/T_2^*$ as a function of the applied dc electric field (E_x) due to Johnson noise from a single noise source for the case $R \approx$ 13 nm, assuming B = 0.5 T. Using the estimated parameters in Appendix D, we find that T_2^* is limited by Johnson noise. Based on our calculations, the effect of EWJN is at least 2 orders of magnitude lower than Johnson noise, and $1/f^\alpha$ noise is negligible (see Appendix D), thus they are not shown here. As shown, the decoherence rate $1/T_2^*$ reaches a maximum at $E_x = E_0$, where the bonding and anti-bonding states are formed and the system is most sensitive to charge noise. The left y-axis of Fig. 4.4(b) shows the maximum decoherence rate $1/T_2^*$ due to Johnson noise as a function of inter-dot separation R. As shown, T_2^* can be improved by shrinking the inter-dot separation. This can be explained by the curvature of the qubit energy curve (e.g. the solid green or blue curve in Fig. 3(a))), which serves as a metric of how the qubit is prone to charge noise near $E_x = E_0$. On the right y-axis of Fig. 4(b), we plot this curvature (a in its absolute value) by fitting the energy curves with a quadratic function of E_x for different R. The curvature term $|a|$ increases with R because the tunnel coupling t_c decreases with R (Fig. 3(c)), causing more abrupt charge transition. As can be seen, $1/T_2^*$ agrees with the trend of the curvature term $|a|$. Consequently, larger tunnel coupling/smaller 2P-1P separation is preferred to enhance the qubit coherence time.

So far, we have investigated the decoherence time due to a single charge noise source. In a real device, there could be multiple charge noise sources (other in-plane gates, top gates, etc.), resulting in T_2^* being degraded by 1-2 orders of magnitude eventually. Even then, using a 2P-1P spin qubit with electrical control is likely to yield devices comparable to single electron spin qubit based on single donor ($T_2^* =$ 268 μs [44]) and single quantum dot qubit ($T_2^* = 120$ μs [4]) based on magnetic control, and outperform the 1P-1P charge qubit ($T_2^* = 0.72$ μs [78]) in terms of qubit coherence time.

4.4 Summary

In summary, we propose a novel approach for all-electrical control of donor-based spin qubits in silicon using full-band atomistic tight-binding modeling and time-dependent simulations based on effective spin Hamiltonian. In this design, ancillary dots are introduced to form an asymmetric 2P-1P system to create a hyperfine coupling difference between 2P and 1P, utilized to realize electron spin control with an ac electric field. We perform a quantitative analysis to optimize this design in terms of X-gate fidelity and decoherence time through external static B-field and tunnel coupling determined by inter-dot separation. We show that a long qubit coherence time can be potentially achieved. This work can serve as an alternative design to those that exploit the hyperfine difference to the donor the interface states [71], where the qubit coherence could be undermined by noise sources near the interface [68, 69]. To further reduce possible sources of deleterious noise in the proposed design, we would further pursue all-in-plane electrostatic and qubit control without the top surface gates in the future.

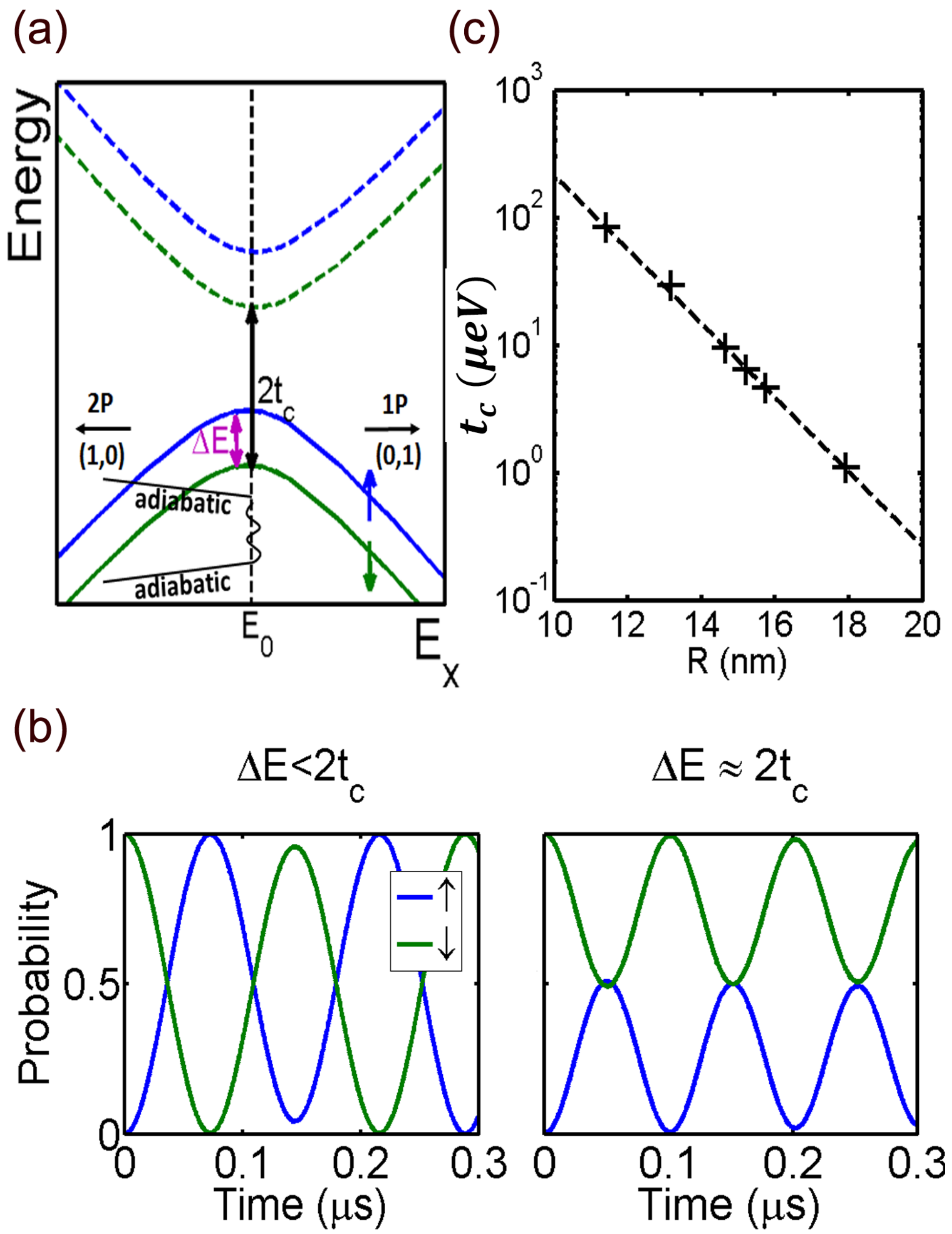

Fig. 4.3. Impact of inter-dot separation on tunnel coupling and Rabi oscillations.(a) The simplified energy diagram of the 2P-1P system under a static magnetic field near the (1,0)–(0,1) charge degeneracy point(E_0). The solid green (electron spin down) and blue (electron spin up) curves represent the two bonding states that define the qubit, separated by ΔE in energy. The dashed curves are the anti-bonding states, $2t_c$ above the bonding states respectively. The explicit nuclear spins are not shown here for simplicity. (b) Electron spin Rabi oscillations under ΔE$< 2t_c$ and ΔE$\approx 2t_c$. (c) The tunnel coupling (t_c) as a function of inter-dot separation (R). The markers " + " indicate data extracted from the atomistic tight-binding simulations, and the dashed curve is fitted to the data with the regression function $t_c = t_0 e^{-bR}$, where $t_0 = 0.1742$ eV and b = 0.67 nm^{-1}.

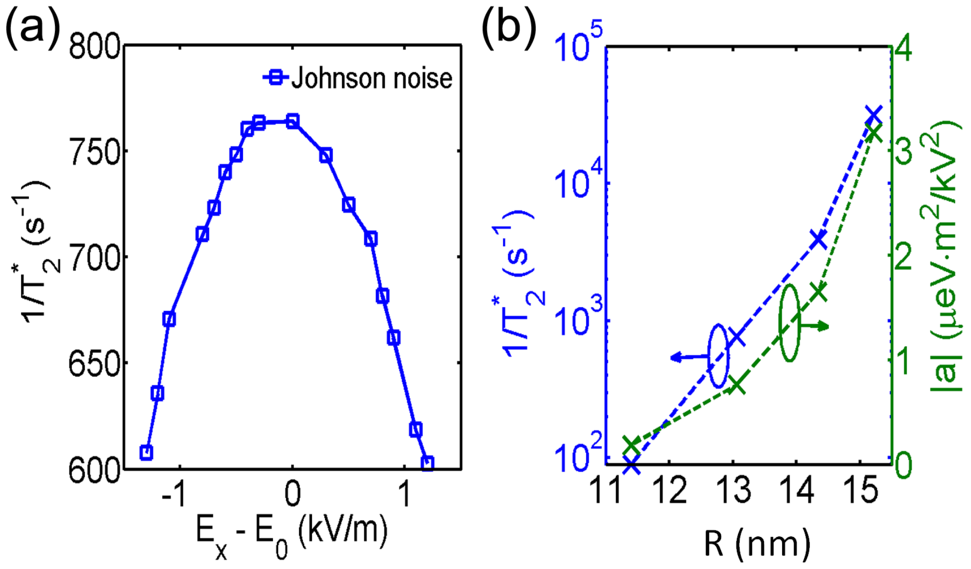

Fig. 4.4. Impact of electric field and inter-dot separation on decoherence time. (a) Qubit decoherence rate $1/T_2^*$ as a function of dc electric field in the x direction due to Johnson noise from a single noise source, for R $\approx$ 13 nm and B = 0.5 T. Here, $E_0 = 5682.2$ kV/m. (b) The maximum $1/T_2^*$ due to Johnson noise (left y-axis) and energy curve curvatures ($|a|$ on the right y-axis) as a function of 2P-1P inter-dot separation R.

5. OPTIMIZING TUNNEL TIME FOR HIGH-FIDELITY SPIN READOUT OF DONOR QUBITS

Part of the work in this chapter is to be submitted to a journal.

5.1 Introduction

Recent works have shown that a new regime of electronics can be achieved in silicon by a bottom-up scanning tunneling microscopy (STM) based fabrication technology [8], capable of achieving unprecedented doping densities with atomic scale precision [13, 79]. With this technology, various functional components of low-temperature electronics, such as metallic leads, gates, quantum dots (QD) and single-electron transistors (SET) have been fabricated by precise placement of dopant atoms on a single plane of silicon [9, 10, 13, 14, 79–81]. Moreover, recent work has indicated that this STM lithography technique provides a mechanism to build a scalable donor-based quantum computer in silicon [7, 10, 13, 14] that can advantage of the extremely long coherence times of the electron and nuclear spins [2, 23, 44]. A quantum computer based on individually addressable phosphorus donors in silicon was first proposed in 1998 by Kane [5], and relies on precision placement of single donors in silicon, a feat that the STM technique achieves with an accuracy of 1 nm [8].

The ability to selectively load and unload electrons by tunneling into and out of single dopants and dopant-based quantum dots is crucial to this new regime of electronics. The tunnel times govern transport characteristics of these devices and lead to the observation of Coulomb and spin blockade [14]. Moreover, the initialization and readout of spin qubits are typically performed through spin dependent tunneling [10, 20, 80, 82], and the fidelity is largely determined by the tunnel rate [83]. Recently, rapid initialization and readout via higher electron states of a single donor qubit has been demonstrated [65]. Also, as donor-cluster qubits have long spin relaxation time and additional addressability [10, 42], their readout times are worth theoretical studying. Therefore, knowledge of how the dopant bound qubit states are coupled to nearby electron reservoirs is therefore critical to design devices. However, to date a comprehensive quantitative theory that can provide design guidance for these devices using a quantum mechanical description is lacking. In this chapter, we present an atomistic method to compute the tunnel times between an SET island and single donor and multiple donors as a function of various design and control parameters of the device.

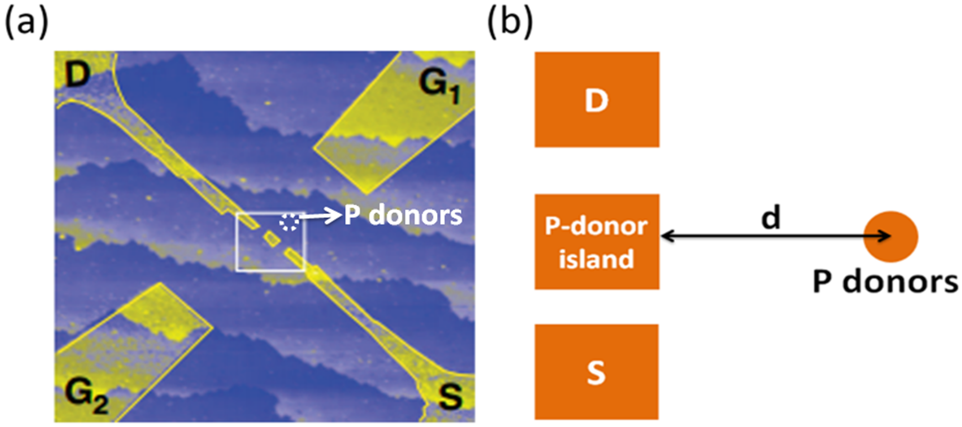

Fig. 5.1. Device structure for single shot spin readout of a donor-based quantum dot. (a) The layout of an STM patterned donor device for spin read-out of a silicon qubit. S and D are the source and drain respectively, whereas G_1 and G_2 are gates [10]. (b) A schematic of the central components of the device, showing source, drain, and an SET P-donor island coupled to a precisely positioned P donor or P donor-cluster at a distance *d*.

In Fig. 5.1, we show a typical device patterned by STM lithography, where a P donor-dot serves as an addressable qubit with an P-donor SET island for spin readout. Fig. 5.1(a) shows the scanning electron microscope (SEM) image of a typical device [10]. The yellow regions are highly doped in-plane gates (G_1, G_2), leads (S, D) and a SET island, with a doping density of 1 P in every 4 Si (i.e. inter-donor separations are usually less than 1 nm). Fig. 5.1(b) depicts the schematic diagram of the central components of the spin-readout device marked as the white box in (a). The disk on the right hand side represents either a single or a few P donors acting as the qubit. The P-donor island is an SET channel comprising a small densely doped three dimensionally confined reservoir with discrete energy levels, allowing the flow of a current when its energy levels are between the Fermi levels of the source (S) and drain (D) regions. Gates G_1 and G_2 can tune the energy levels of the SET and the donor qubit, and can cause an electron to be loaded onto or emptied from the donor by quantum tunneling [80] depending upon the energy level alignment of the two systems.

The separation distance between the donor and the SET island (shown as d in Fig. 5.1(b)) is a critical design parameter of this device. The tunnel time is found to be exponentially sensitive to this separation distance and can therefore be engineered by orders of magnitude by choosing an appropriate d. Since both single donor and donor-cluster qubits are being considered for scalable quantum computer architectures [10,16,17], we investigate the tunnel times from a single P donor and 2P clusters with varying number of electrons.

5.2 Modeling Strategy

To model the system with quantitative accuracy, several challenges need to be overcome. First, the wavefunctions of electrons confined in the donor and the SET need to be captured from a full 3D quantum mechanical method that also includes the multiple conduction band valley degrees of freedom in silicon. A full 3D description is needed because both the donor and the SET are 3D confined systems with discrete energy states that are not isotropic where a lower dimensional approximation to their wavefunctions would compromise the accuracy of the method [84]. Also, it is well-known that the indirect gap conduction band valley degeneracies in silicon ascribe short-range highly oscillatory components to the wavefunctions based on the symmetry of the potential and thus needs to be taken into account [40]. Second, strong electron-electron interactions in multi-donor clusters in the few-electron regime are responsible for the binding energies and wavefunction extents of the electrons, and need to be captured in a computationally feasible manner [14]. Third, the SET region comprises of about a hundred donor atoms and bound electrons due to its large doping density, where a full self-consistent atomistic treatment of silicon and the donors to obtain its electrostatic potential is not feasible. For example, in reference [10], the size of the SET island is $\sim 10 \times 5$ nm^2 and the 2D doping density is $\sim 2\times 10^{14} cm^{-2}$. Although both ab initio [85] and tight-binding [86] methods have been employed in the past to model small periodic unit cells of silicon with such high doping densities, these methods cannot be extended to solve a finite-sized SET of large dimensions considered in this work. Fourth, the tunneling problem considered here is a non steady-state fully quantum mechanical problem, and well-known steady-state approaches such as the non-equilibrium Green's function (NEGF) method [87] or the semi-classical WKB approaches are not directly applicable. Hence, we need methods that take into account all the above described complexities to provide general 3D wavefunctions from which the tunneling times can be computed.

We have combined several methods to provide a multi-scale model of the system, as outlined here. 1) We employ a large-scale atomistic tight-binding (TB) approach to solve the donor and the SET wavefunctions in a 3D silicon lattice. 2) We use a self-consistent Hartree method with tight-binding to capture electron-electron interactions in multi-donor clusters. 3) For the solution of the SET potential, we use a finite-element (FEM) non-linear Poisson solver with semi-classical charge density using Fermi-Dirac statistics. 4) To compute the tunnel times, we employ Bardeen's transfer matrix approach [88] with TB wavefunctions. Below we describe each of these methods in detail.

The TB model employed in this work uses the $sp^3d^5s^*$ atomic orbital basis with spin-orbit interactions, and captures the full band structure of silicon including accurate effective masses, band gaps, valley degeneracies [36], as benchmarked against a variety of experiments with the NEMO3D tool [39, 89]. A single P donor is represented by the Coulomb potential of a positive charge screened by the dielectric constant of silicon, along with an on-site cut-off potential representing the much studied central-cell correction [35, 39]. This approach has successfully reproduced the full energy spectrum of a single P donor in silicon, as well as various charge and spin properties [35, 56, 57]. Recent STM imaging experiments have shown that this donor model reproduces both the observed spatial and momentum space electron probability distribution of the donor [40]. The full TB Hamiltonian is solved using a parallel block Lanczos eigen solver in 64 processors to obtain the relevant energy states and wavefunctions of the donor just below the conduction band.

To address multi-electron occupation of these complex multi-donor systems, we have adopted a self-consistent Hartree approximation in which the electron-electron interaction potential is obtained iteratively from the electron density $n(r)$ given by $\sum_i^N |\psi(r)|^2$, where the summation is over the N lowest spin-resolved eigenstates of the TB Hamiltonian for N electron occupation. Exchange and correlation potential is obtained from the local density approximation on $n(r)$ [86], and added to the total potential in the TB Hamiltonian, and iterated till convergence. The above method has been successfully used to compute donor cluster binding energies and spin-lattice relaxation times in quantitative agreement with experiments [14, 41, 42].

The SET region comprises of a hundred donor atoms and bound electrons due to its large doping density, and a full self-consistent atomistic treatment of silicon and the donors to obtain its electrostatic potential with either ab initio [85] or tight-binding [86] approach is not feasible. Here, the semi-classical potential of the SET is obtained from a solution of the non-linear Poisson equation with a FEM grid in the Senaturus tool [59]. A doping density of $N_D = 10^{21}\ cm^{-3}$ is used in the SET island with the bandgap narrowing effect considered. We assume a p-type substrate with $N_A = 10^{15} cm^{-3}$ in line with experiment. Since most of the measurements are performed at cryogenic temperatures, we use a temperature of 2K in the simulation. The electron distribution is computed from the conduction band effective density of states N_c of silicon and the Fermi-Dirac integral in the framework of Sentaurus. The semi-classical SET potential is then interpolated on to the atomistic lattice, and added to the TB Hamiltonian to solve for the SET wavefunctions.

Once the donor and the SET wavefunctions are available, the electron tunnel time can be computed using Bardeen's transfer matrix method [88], which has been widely used to model and understand electron tunneling in STM measurements. The resonant tunnel time T_R can be obtained by

$$\frac{1}{T_R} = \frac{2\pi}{\hbar}|\langle \Psi_D|H - H_{SET}|\Psi_{SET}\rangle|^2 \tag{5.1}$$

$$H_{SET} = H_0 + U_{SET} \tag{5.2}$$

$$H = H_0 + U_{SET} + U_D + U_{ee} \tag{5.3}$$

where H_{SET} denotes the SET Hamiltonian which includes the background silicon Hamiltonian H_0 and the effective potential energy U_{SET} from the semi-classical approach. H is the total Hamiltonian, which includes, apart from H_{SET}, the donor potential energy U_D given by the positive charge of the P donors, and U_{ee} the repulsive potential energy of the electrons from the self-consistent Hartree method in case of multi-electron occupation. Ψ_D indicates the donor or donor cluster wavefunction solved from $(H_0 + U_D + U_{ee})\Psi_D = E_D\Psi_D$ for eigen energies E_D. Ψ_{SET} is the effective single electron wavefunction of the SET solved from $H_{SET}\Psi_{SET} = E_{SET}\Psi_{SET}$ for SET eigen energy E_{SET}.

5.3 Results and Discussions

Fig. 5.2(b) shows the computed tunnel times as a function of qubit-SET separation distance and bound electron number for both a single donor (blue curve) and 2P clusters with different electron numbers. Two different intra-cluster donor separations are considered for the 2P cluster to show the effect of small variations in donor locations due to variations in STM lithography. Fig. 5.2(a) shows these two 2P configurations on a plane of Si with donor separations of 0.86 nm and 1.58 nm, denoted as D2 and D4 respectively.

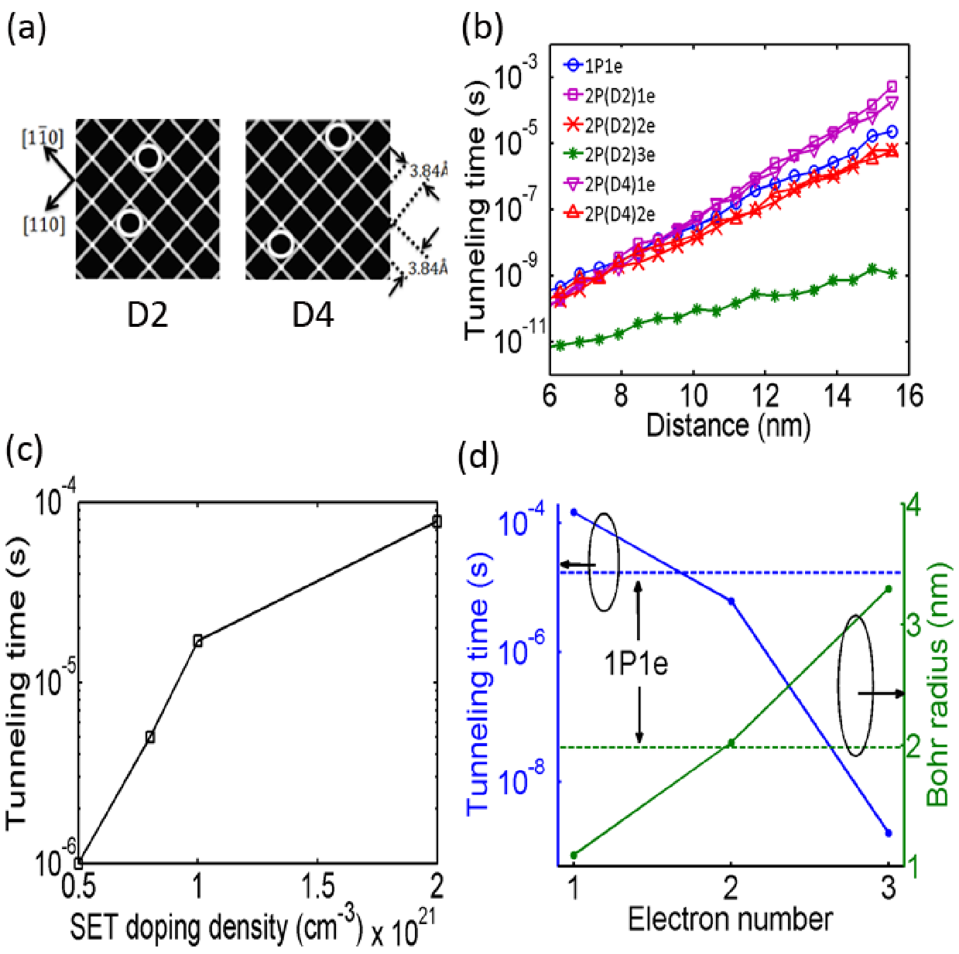

Fig. 5.2. Tunnel time sensitivity to donor-dot electron number and location. (a) The atomic locations of P donor(s) in a 2P cluster shown on the 2D plane of the silicon. (b) The electron tunnel time as a function of distance between the SET island and the donor (blue) or donor-clusters (violet and red) for various numbers of electrons. (c) The tunnel time at a separation distance of 15 nm of a single donor as function of the doping density of the SET island. (d) The tunnel time at a separation distance of 15 nm and the Bohr radii of the 2P(D2) donor-cluster as a function of the number of bound electrons compared with the tunnel time for a single donor single electron.

The solid blue curve in Fig. 5.2(b) represents a single P donor with 1 bound electron. On a semi-log plot, the tunnel times between the donor and the SET island appear nearly as a straight line, showing the tunnel times increase exponentially with

SET-donor separation as expected. Importantly, we see the tunnel times increase exponentially from $\sim 10^{-10}$s at 6 nm to $\sim 10^{-4}$ s at 16 nm, over ~6 orders of magnitude within 10 nm.

In experiments, there are uncertainties in the donor number and bound electron number of the SET island and substrate doping density, which impacts the effective single-electron confinement landscape of the SET island. Effectively, the doping density could deviate from $10^{21} cm^{-3}$ and affect the tunnel times. In Fig. 5.2(c), we fix the distance of the single donor and the SET island as 15 nm and show the tunnel time as a function of the SET doping density. As can be seen, the tunnel time can be changed from ~ 1 μs to ~ 78 μs by changing the SET doping density from $0.5 \times 10^{21} cm^{-3}$ to $2 \times 10^{21} cm^{-3}$, which is a reasonable range given such uncertainties. In the following discussions, we will always use $10^{21} cm^{-3}$ to be in line with the experimental assumption.

Fig. 5.2(b) also shows how the tunnel times vary for 2P donor clusters with one, two and three electron occupation portrayed by the red, violet and green curves respectively, the slopes of which are sensitive to the electron number. Although all these donor-electron configurations show an exponential increase in tunnel times with distance as before, the slopes of the curves are now sensitive to the electron number. This is because the tunnel times depend on the decay length of the electron wavefunctions, which in turn depends on the net charge of the system. A wavefunction that decays faster produces less overlap and tunnel coupling with an SET bound wavefunction, which translates to longer tunnel times. The 2P2e cases (red curves) lie very close to the 1P1e curve, as both cases result in a charge neutral system with comparable wavefunction extent. In the 2P1e cases (violet curves), the wavefunction is more confined at the donor cores and decays more rapidly due to the remnant positive charge of the nucleus. As a result, the tunnel times are larger than the 1P cases for most separation distances. The 2P3e case (green curve) has the largest wavefunction extent due to the net negative charge of the configuration, and therefore the tunnel times are much shorter.

The green curve in Fig. 5.2(d) shows the effective Bohr radius in the SET-donor separation direction as a function of electron number. The Bohr radius is extracted from the converged Hartree wavefunction by numerically fitting an exponential function. The size of the electron wavefunction of a donor-cluster is different for different electron numbers, and as a result the tunnel time of the qubit electron varies dramatically. For a distance of 15 nm between the donor dot and the SET island, the blue curve in Fig. 5.2(d) shows the tunnel time as a function of the number of electrons bound to the donor-cluster in comparison with the tunnel time of single P donor qubit (dotted blue horizontal line). As shown, the tunnel time for the first electron is about 2 orders of magnitude longer than that of the single P qubit due to the stronger quantum confinement. In this two-donor system, the tunnel time decreases by 4 orders of magnitude as 3 electrons are loaded on to the 2P cluster, as Coulomb repulsion between the electrons causes the wavefunction to spread out spatially. It seems that the tunnel time can be decreased dramatically by taking advantage of multi-electron occupation of a donor cluster qubit. But one needs to keep in mind that spin relaxation time (T_1) also decreases several orders of magnitude when there is multi-electron occupation. Reference [42] showed T_1 in a 2P donor-cluster can be decreased by 4-5 orders of magnitude from 1e to 3e. As a consequence, the trade off between the tunnel time and T_1 needs to be considered in designing a scalable and addressable qubit architecture.

5.4 Summary

We have developed a multi-scale modeling method, combining atomistic tight-binding approach, semi-classical solution of electrostatics, self-consistent Hartree theory, and Bardeen's transfer matrix method to compute the electron tunnel times between donors and SET islands used in spin-readout devices. We overcame the challenge of treating a non-steady state tunneling problem in full 3D taking into account a quantum mechanical description of the host band structure and electron-

electron interaction in a realistic device setting, which enables us to compare directly with the measurements of state-of-the-art spin-readout experiments. The tunnel time is found to be exponentially sensitive to the distance between the donor and the SET island and decreases significantly as the electron number increases in a multi-donor cluster. Device design considerations are put forward for addressable 1P and 2P qubit configurations, demonstrating a tradeoff between the spin relaxation time and spin readout time.

The developed multi-scale modeling method has some drawbacks in the modeling of the SET island due to computational limitations. First, the SET P-donor island is not treated fully quantum mechanically. Though the band gap narrowing effect is considered in the TCAD model, the full band structure including the impurity bands of a δ-doped layer [85, 86] and that under quantum confinement are not well captured. Second, The SET island is not treated fully atomistically. The Coulombic donor potentials are not included in the charge and potential calculations, and electron density is not computed from a full quantum solution. Moreover, atomic disorder (random donor locations, diffusion and segregation) is not accurately considered. The consequent effect might not affect the final wavefunction of the SET island and the calculated tunnel times much as they can be averaged out due to the large number of donors, but it is worth further validating. The above limitations can result in inaccuracy of the obtained wavefunction of the SET island, which can lead to discrepancy between the calculated and the measured tunnel times. Therefore, a more accurate model to treat the SET electronic structure is in need of further development.

6. BULK AND SUB-SURFACE DONOR BOUND EXCITONS IN SILICON UNDER ELECTRIC FIELDS

The work in this chapter is published in Ref. [98], and the text is taken from there.

6.1 Introduction

In this chapter, we investigate the electronic structure of the donor bound exciton (D^0X) in silicon under the influence of electric fields and interfaces, thus mimicking the environment of realistic devices. This is required since single spin readout in a quantum computer can not be achieved in a bulk environment but requires a device environment. The electronic states of the donor bound exciton are influenced by the complicated band structure of silicon including its multiple valley degeneracy in the conduction band (CB), the light and heavy hole valence bands (VB), the Coulomb bound donor states and the three-particle fermionic interactions. We include all these factors in quantitative details using an atomistic tight-binding method over a silicon lattice of one million atoms, and compute the spin-resolved transition energies and transition dipoles of the D^0X in a gated nanostructure. For specificity, we refer here only to the most common shallow donor in silicon, phosphorus. These methods can readily be generalized to the other shallow donors Sb, As and Bi, which have slightly different electronic binding energies, and also different nuclear spins and hyperfine constants.

Three-particle excitons or trions have also been reported recently in two-dimensional materials such as MoS_2 [90, 91] and have attracted much attention as a test-bed for studying many-body interactions in a semiconductor with both spin and valley degrees of freedom. Previous theoretical studies in bulk D^0X in silicon have been performed from effective mass approximations to understand Auger recombination in

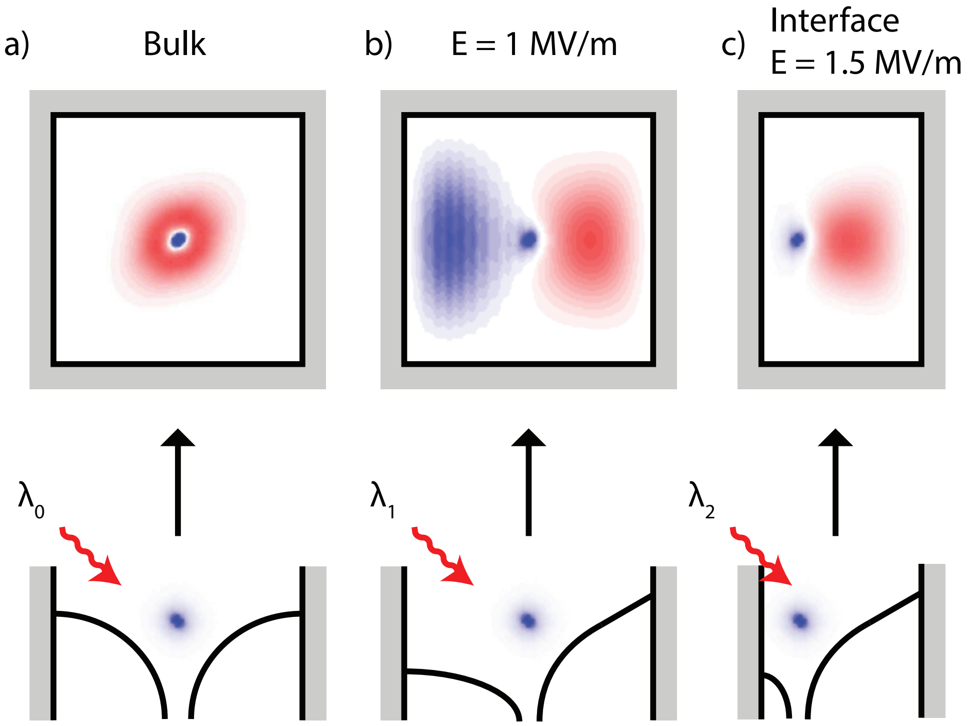

Fig. 6.1. Schematic of the photon induced transition from a Coulomb bound electron in a donor to a donor bound exciton in bulk a) with and b) without an electric field, and c) in a confined nano device with an interface and electric field. The blue and the red color describes the electron and hole probability densities respectively. The bottom panel provides a 1D schematic of the Coulomb potential of the donor core.

donors [92] and more recently to investigate applications such as quantum Hall charge sensors [93]. This work presents atomistic electronic structure calculations of the D^0X in a device environment for the first time, crucial for experiments to integrate optical addressing methods in a silicon quantum computer.

A neutral P donor in bulk silicon comprises a positively charged donor core that produces a Coulomb potential and binds an electron 45 meV below the conduction band edge (also called the D^0 state). If stimulated by a laser pulse of appropriate wavelength, an additional electron and a hole can be generated and bound to the impurity, forming the donor bound exciton (D^0X), as shown in Fig. 6.1a) for a bulk donor, with blue and red representing the electron and hole wavefunction probability densities respectively. The bulk transition energy from a D^0 to a D^0X state has been measured to be near 1150 meV [23]. Fig. 6.1b) shows a schematic of the same system under an applied electric field. Both the D^0 and the D^0X undergo a Stark shift, however the latter is more strongly perturbed due to the larger size of the wavefunction. The electric field pushes the electrons and holes in opposite directions and thus changes the excitation wavelength from λ_0 to λ_1. Fig. 6.1c) shows the combined effect of an interface and an electric field with excitation wavelength λ_2. In this case, the donor wave functions are also truncated by the interface. Later, we will show the transition energies, Hartree energy, wavefunctions and transition dipole moments for these three cases, as well as the interface and E-field induced hyperfine and hole splitting that can affect the spin-resolved transition energies.

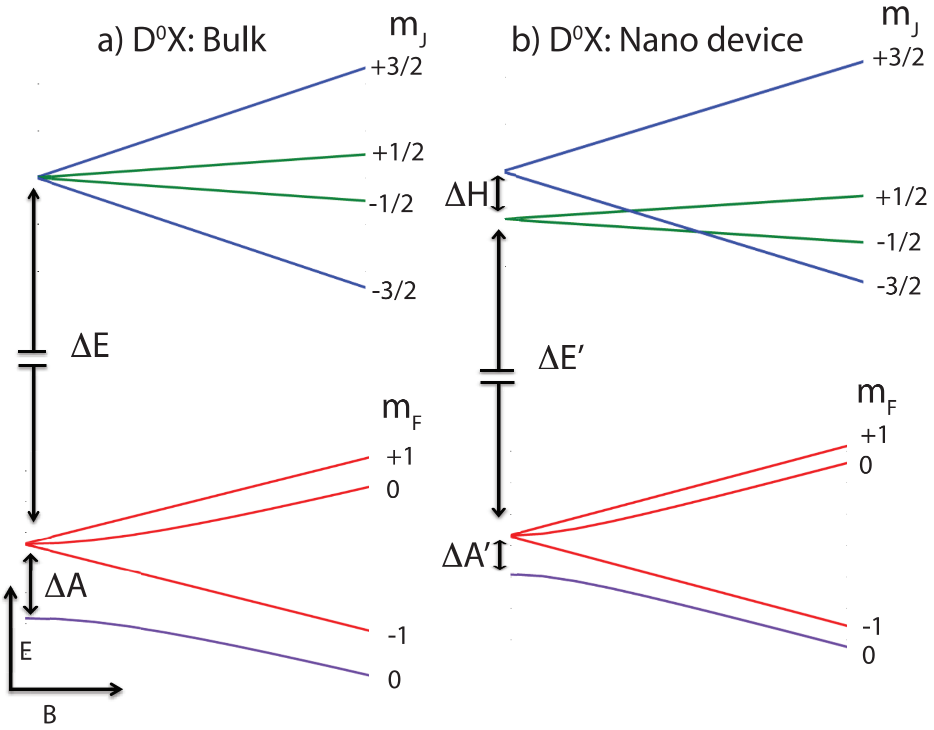

Fig. 6.2. Energy levels and spin structure of the D^0X in a magnetic (B) field a) in bulk and b) in a nanostructure. ΔA ($\Delta A'$) and ΔH denote the hyperfine and heavy hole-light hole splitting respectively, while ΔE ($\Delta E'$) is the formation energy at $B = 0$.

In Fig. 6.2, a schematic of the energy levels of the D^0 and D^0X are shown for a bulk-like exciton and an exciton in a nanoscale device. In the D^0 state, the hyperfine interaction between the nuclear and the electronic spins produces a singlet and a triplet splitting ΔA. The D^0X has two electrons spin paired in a singlet with $S = 0$, and as a result, the spin splitting in a B-field is governed by the hole 3/2 and 1/2 total angular momentum states, which arise from the heavy hole (HH) and the light hole (LH) bands. If the donor is located close to an interface or subjected to an electrical field, then the transition energies of the D^0X are strongly modified, as shown in Fig. 6.2b). First, the presence of an interface or electric field changes the localization of all the confined particles in both D^0 and D^0X. As the wave functions shift and deform in space, the particle-particle interactions also change. We have computed this transition energy from self-consistent Hartree method with tight-binding, and denote it as $\Delta E'$. Second, the electric field or the interface also splits the 3/2 and 1/2 states of the hole bound to the D^0X, which we denote as ΔH. This splitting is due to the effect of confinement on the HH and LH bands, which have different effective masses. Third, the hyperfine coupling of the D^0 state also changes due to the field and depth [35], and is denoted as $\Delta A'$ in Fig. 6.2b). Details of how the spin-resolved D^0X transitions can be used to initialize and readout the donor nuclear spins using an Auger recombination process can be found in Refs [23, 24].

6.2 Method

We employ an $sp^3d^5s^*$ atomic orbital tight-binding method with spin-orbit interaction and nearest neighbor coupling to represent the full band structure of silicon [35, 39–41, 89, 94]. Details of the methods can be found in the following.

The Hamiltonian of the three-particle D^0X is given by,

$$H = H_{0,e_1} + H_{0,e_2} + H_{0,h} + H_{e_1,e_2} + H_{e_1,h} + H_{e_2,h} \tag{6.1}$$

where the first three terms represent the single particle Hamiltonian of the two electrons (e_1, e_2), and the hole h, and the last three terms are the pairwise Coulomb interaction between the three particles. Each of the $H_{0,n}$, for $n \in \{e_1, e_2, h\}$ includes the Hamiltonian of the silicon lattice H_{Si}, the potential energy of the donor atom V_D, and the potential energy of the applied electric field F, and is given by,

$$H_{0,n} = H_{Si} + V_D - e\vec{F} \cdot \vec{r} \tag{6.2}$$

In the atomistic tight-binding formalism employed here, H_{Si} is represented in a basis of 20 atomic orbitals (sp^{3}d^{5}s*) per atom including spin in the basis and nearest neighbor interactions [89]. For a bulk silicon unit cell, the model reproduces the full band structure of the host material [37]. Surfaces are treated as dangling bond passivated following the model shown in Ref [38]. The donor potential energy is represented as a Coulomb potential with an on-site cut-off term and an orbital based central-cell correction, and reproduces the full spectrum of donor bound states including a ground state at 45.6 meV below the conduction band [35, 39]. For the solution of a bulk single donor in silicon, a box size of 30 nm × 30 nm × 30 nm was used such that the donor wavefunctions are not affected by the interfaces of the box. The model has been used in a variety of earlier works to reproduce various experimental data with very good accuracy [35,40,42,94]. The resulting Hamiltonian is solved by a parallel block Lanczos eigen solver to obtain a set of states close to the conduction and valence band edges [38].

An exact solution of the three-particle system involves diagonalizing eq. 6.1 in the basis of many Slater Determinants comprising of the single particle electron and hole states until convergence is achieved with the so called Configuration Interaction (CI) approach. However, such an approach is computationally intractable for a Hamiltonian of over one million atoms, as Coulomb and exchange integrals between the three particles need to be computed with a very large number wave functions to represent the spatial spread and symmetries of the electrons and holes. Hence, we employ a mean-field method based on the self-consistency between the effective single particle Hamiltonian of each particle and the Poisson equation. In this approach, the particles are each represented with a separate Hamiltonian taking into account the mutual interactions, as described below,

$$H_{e_1} = H_{0,e_1} + V_{e_2} + V_h \tag{6.3}$$

$$H_{e_2} = H_{0,e_2} + V_{e_1} + V_h \tag{6.4}$$

$$H_h = H_{0,h} + V_{e_1} + V_{e_2} \tag{6.5}$$

Here, each particle is subjected not only to the host and donor potential along with the applied field ($H_{0,n}$), but also to the potential due to the other two particles (V_n). Finding an approximate solution can be done by initially solving the three Hamiltonians with all $V_n = 0$ to obtain the respective initial wave functions Ψ_{0,e_1}, Ψ_{0,e_2}, and $\Psi_{0,h}$, and corresponding energies E_{0,e_1} , E_{0,e_2} and $E_{0,h}$. Using these wavefunctions, the charge densities $n(r)$ and the potential V_n can then be computed. Using these new V_n terms, the Hamiltonians are solved again, and the process repeated till the energies and the wavefunctions converge. A similar technique had been used to compute the D$^-$ (two-electron) state of a P donor in close agreement with experimental measurements [41], and more recently to obtain charging energies of multi-electron donor clusters [14].

If the final ground state energies of the Hamiltonians shown in eq 3-5 are given by $E_{f,e1}$, $E_{f,e2}$ and $E_{f,h}$ with f denoting the final iteration (Ψ_{f,e_1}, Ψ_{f,e_2}, and $\Psi_{f,h}$ being the corresponding wavefunctions), then the total three-particle interaction energy E_C is given by,

$$E_C = \frac{1}{2}[E_{f,e1} + E_{f,e2} + E_{f,h} - E_{0,e1} - E_{0,e2} - E_{0,h}] \tag{6.6}$$

Also, the total energy E_T is given by,

$$E_T = E_{0,e1} + E_{0,e2} + E_{0,h} + E_C \tag{6.7}$$

The transition energy from the D^0 state to a D^{0}X state depends on the difference of the total energy of the two systems, and is given by,

$$\Delta E = E_T(D^0X) - E_T(D^0) \tag{6.8}$$

where $E_T(D^0X)$ and $E_T(D^0)$ are the total energies of D^{0}X and D^0 respectively. In our calculations, the total energies are with respect to the VB edge at F=0 MV/m (i.e. the 0 eV reference point). If E_D is the donor binding energy relative to the CB edge, corresponding to -45.6 meV for a bulk donor at F=0 MV/m, then $E_T(D^0) = E_g + E_D$, where $E_g = 1.17$ eV is the low temperature (4K) band gap of silicon. E_D changes with donor depth and electric field, as shown earlier [56]. Hence, the transition energy ΔE is expected to vary with donor depth and applied electric field, as both $E_T(D^0X)$ and $E_T(D^0)$ change.

The transition dipole moments describe a photon induced transition from the D^0 state to a D^{0}X state, and is given by the dipole moment between the electron and the hole wavefunctions,

$$\begin{aligned} W_{D^0->D^0X} &= q|\langle\Psi_{0,e_{1,2}}|\vec{r}\cdot\hat{e}|\Psi_{f,e_1}\rangle\langle\Psi_{f,h}|\vec{r}|\Psi_{f,e_2}\rangle \\ &\quad +\langle\Psi_{0,e_{1,2}}|\vec{r}\cdot\hat{e}|\Psi_{f,e_2}\rangle\langle\Psi_{f,h}|\vec{r}|\Psi_{f,e_1}\rangle|^2 \end{aligned} \tag{6.9}$$

where $\hat{e}$ is the polarization direction of the photon and $\vec{r}$ is the dipole operator. The first term represents a transition in which the D^0 electron (denoted by Ψ_{0,e_1} or Ψ_{0,e_2}, which are the same) forms electron 1 of D^{0}X, while electron 2-hole transition emerge based on the dipole moment. The second term represents the other pathway in which the D^0 electron forms electron 2 of D^{0}X, and electron 1-hole transition results due to the photon. If one of the electrons and the hole are now spatially separated by the E-field, $\langle\Psi_{f,h}|\vec{r}|\Psi_{f,e_2}\rangle$ or $\langle\Psi_{f,h}|\vec{r}|\Psi_{f,e_1}\rangle$ decrease as a result of reduced wavefunction overlap. Eq 9 therefore provides a measure of the transition probability from D^0 to D^{0}X.

An exact electronic structure calculation of D^0X involves a three-interacting particle solution of the system Hamiltonian taking into account description of multiple conduction band valleys and features of multiple valence bands. While simplified effective mass envelope function solutions may be possible, it is difficult to incorporate all the band structure effects, such as valley-orbit and spin-orbit interactions, multi-valley and multi-band descriptions under a unified framework. Furthermore, the hyperfine structure and the spin structure needs to be computed, in addition to the effects of fields and interfaces. It is also cumbersome to perform a density functional calculation, as the wavefunctions of the holes and electrons typically spread out over 30 nm × 30 nm × 30 nm of silicon lattice (1.4 million atoms). The atomistic tight-binding technique employed [35,89] in this work provides a suitable compromise between computational rigor and complexity, as multi-million atom systems can be simulated at ease including the full band-structure of the host material. Particle-particle interactions can be also incorporated in a computationally tractable manner through a self-consistent mean-field description [41] without using the more exact CI method [48].

The only compromise we make here is that the mean field approach does not capture exchange and correlation effects. However, the singlet electronic state of the D^0X can be described well without considering exchange and spin correlations, as shown by Hartree calculations of the D^- state of the donor, which reproduces the charging energy within 1-2 meV. The two electron state of the donor has higher order orbital correlations since excited orbital states beyond 1s are needed to describe the spatially extent D^- wavefunctions. However, our self-consistent Hartree method iteratively updates Hamiltonian till the mean-field Coulomb interation converges. Hence, the orbital extent is well-captured by this method [13]. Furthermore, the hole is distinguishable from the electron pairs by its charge, and the indistinguishable particle CI method does not need to be used in this case.

6.3 Results and Discussions

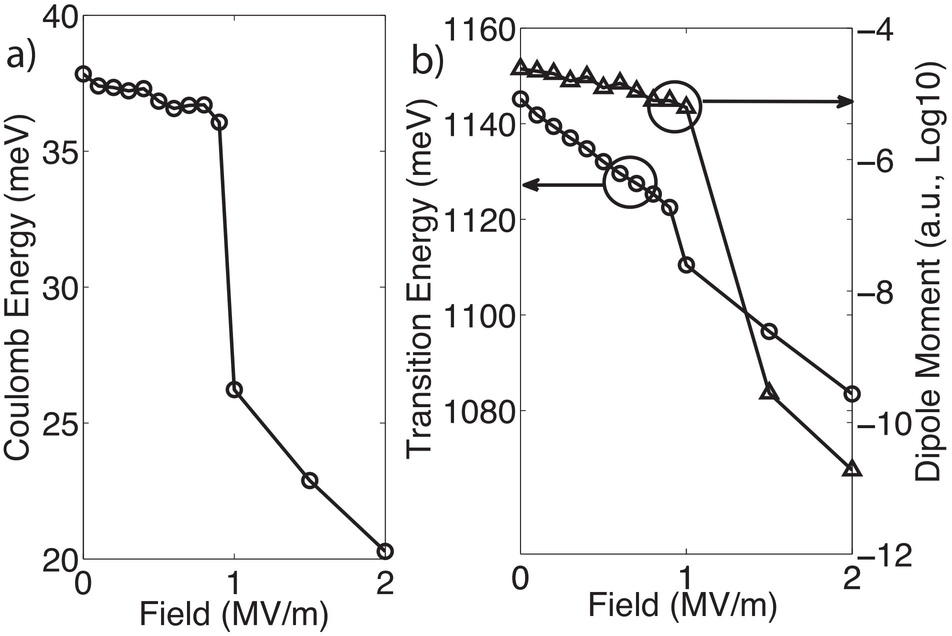

Fig. 6.3. a) Coulomb energy of the three-particle system with E-field. b) Transition energy (left axis) from D^0 to D^0X for a bulk-like system as a function of an applied E-field. Transition dipole moment (right axis) from D^0 to D^0X with E-field.

First, we investigate the Stark effect of the D^0X when the donor is in bulk silicon. Fig. 6.3 shows the Coulomb energy, transition energy and transition dipole moment of the three-particle D^0X for a bulk-like case as a function of an electric field. In the simulation, a bulk system is represented by a 30 nm × 30 nm × 30 nm of silicon lattice bounded by hydrogen passivated hard-walls on all sides. The donor is placed at the center of the box, and the simulation domain size is chosen such that the electronic and hole wavefunctions at zero E-field are not affected by the boundaries of the box. This is reasonable as the Bohr radii of the D^0 and D^- states are in the range of 1-4 nm.

The Coulomb energy of the D^0X comprises of the repulsive energy between the two electrons and the attractive energy between the hole and each of the electrons.

Fig. 6.3a) shows this three-particle Coulomb energy with an E-field, computed from eq 3 of the Supplementary Materials (SM). At low fields, the Coulomb energy lies between 35 and 40 meV, and decreases slightly with the field. It is known that the Coulomb energy in the two-electron D^- state is about 43 meV at zero E-field [41]. Therefore, the attractive energy of the hole in D^0X reduces the total Coulomb energy to sub 40 meV. As the E-field is increased, the electron and hole wavefunctions are spatially separated steadily, and the Coulomb energy decreases. An abrupt drop in the Coulomb energy is observed in Fig. 6.3a) at about F=1 MV/m as the hole and one of the electrons ionize to opposite surfaces of the bounding box. The E-field produces triangular wells at the opposite surfaces (in the CB and VB). When the energy of the bound states in these triangular wells are lower than those of the Coulomb bound states (including mutual screening between the particles), the electrons and holes localize at the surfaces. As a result, the large spatial separation between the three particles at ionization reduces their net electrostatic interaction.

The transition energy required to excite a D^0 into a D^0X state is computed from the difference of the total energies of the D^0X and D^0 as given by eq 6 of the SM, and is shown in Fig 6.3b) on the left vertical axis. Using the low temperature band gap of 1.17 eV in silicon, the transition energy at zero field (F=0) is 1145 meV in close agreement with the experimental measurements [24]. It is to be noted that no fitting parameters are used in the D^0X simulations. As the E-field is increased, the transition energy drops gradually untill an abrupt drop is witnessed at F=1 MV/m due to field ionization. Overall the transition energy decreases with E-field due to both the reduced Coulomb energy and the reduced energy difference between the single particle orbital energies in the CB and in the VB.

A reduced transition energy with E-field, however, does not mean that the D^0 to D^0X transition becomes more likely. The transition probability is governed by the dipole moment between the wavefunctions which depends strongly on their spatial overlaps. Using eq 7 of the SM, we evaluated the transition dipole moment of the D^0X in Fig. 6.2b) on the right vertical axis. It is shown that the dipole moment is large at low E-fields and close to the F=0 value, but decreases rapidly by orders of magnitude near F=1 MV/m. As the hole and one of the electrons are ionized towards opposite surfaces, the spatial overlap of the wavefunctions of the three particles diminish abruptly, making the D^0 to D^0X excitation unlikely.

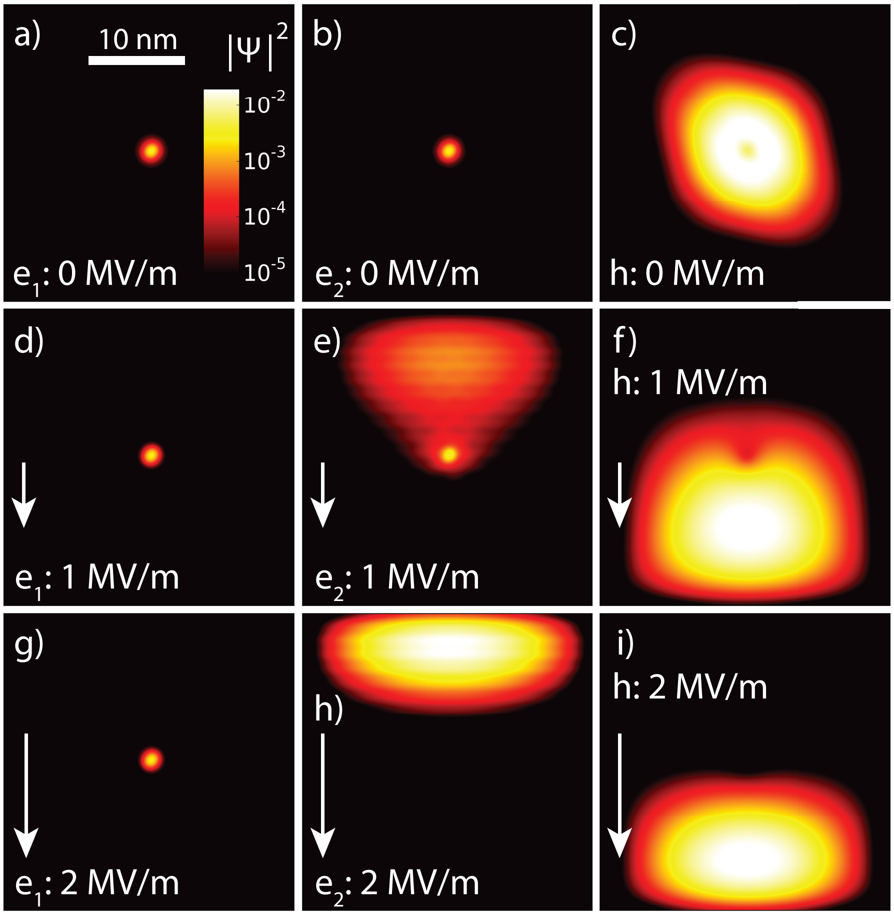

Fig. 6.4. Wavefunction probability density ($|\psi|^2$) of the two electrons (column 1 and 2) and the hole (column 3) plotted separately for a bulk-like donor. Each row shows $|\psi|^2$ for a specific E-field. a-c) are for F=0, d-f) for F=1 MV/m, and g-i) for F=2 MV/m.

Fig. 6.4 shows the spatial probability densities of the electron and hole wavefunctions with an E-field applied along the vertical direction.The first row depicts the probability distributions (a-c) without an E-field, showing the electrons to be tightly bound to the donor as in the D^- state [41]. Since the hole experiences a weak negative potential of the two electrons, its probability distribution spreads out over a larger region, but is still far from the edges of the bounding box. Hence, the use of 30 nm $\times$ 30 nm $\times$ 30 nm box to represent the bulk-case is justified. The hole wavefunction assumes a more p-like structure as shown by the lower density at the core (green) and a larger density rim (red) surrounding it. As a vertical E-field of 1 MV/m is applied in the second row, one of the electrons remains donor bound (d), while the other electron is pulled opposite the E-field towards the top surface (e). The hole, on the other hand, is pushed towards the back surface in a direction along the E-field (f). Hence, the overlap between the three particles decreases. However, both the electrons and the holes still have some density at the core, showing that the ionization at this field is only partial. The 3rd row shows the complete ionization case at a large E-field of 2 MV/m, in which the electron (h) and hole wavefunctions (i) are fully localized near the surface. At even larger biases, the donor bound electron (g) will eventually also ionize to the surface, but this regime is not pertinent to this work.

Next, we investigate the Stark effect of the D^0X when the donor is closer to a surface, which is more representative of a realistic device. It was shown in prior works [56] that a single electron bound to a donor in silicon can undergo strong orbital Stark shift if the donor depth D from the surface is small (typically $<$ 6 nm). In this case, a large E-field can be applied without completely ionizing the donor electron. At these relatively large E-fields, the donor orbitals hybridize with the confined states of the triangular well at the surface, resulting in a gradual (non-abrupt) ionization process.

Fig. 6.5a) shows the three-particle Coulomb energy for the D^0X when the donor is at 4.2 nm depth from the surface. The Coulomb energy is still in the sub 40 meV range, but decreases slightly below the bulk value at F=0. The high potential

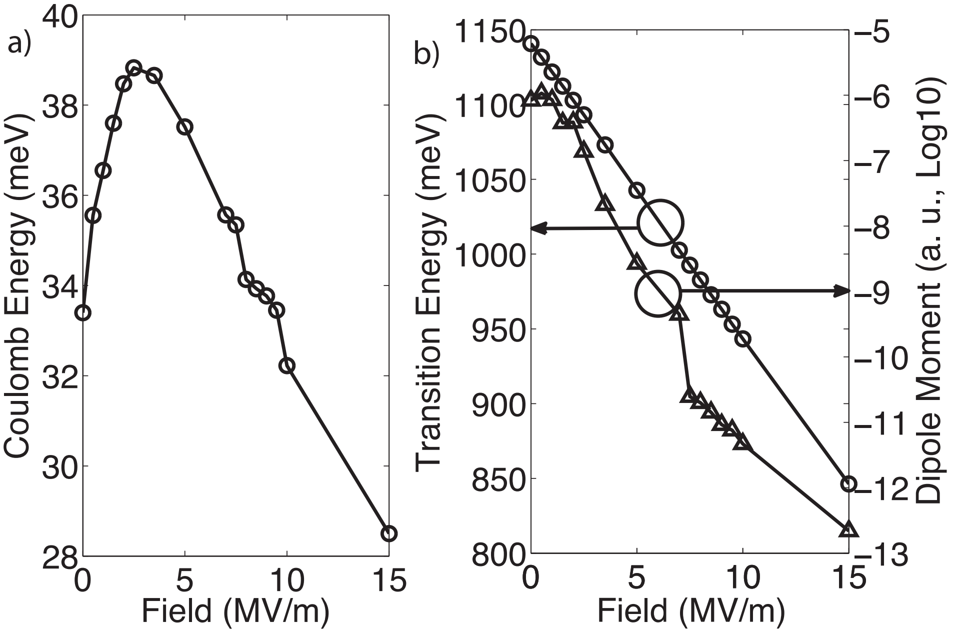

Fig. 6.5. a) Coulomb energy of D^0X for a donor 4.2 nm from an interface as a function of E-field. b) Transition energy (left) and dipole moment (right) for the same.

barrier at the surface not only truncates part of the wavefunction but also pushes the asymmetric charge densities a bit off the donor center with the electron wavefunctions slightly shifting deeper into the lattice and the hole wavefunction moving closer to the surface. The Coulomb energy is maximum when the electron-hole charge densities are centered around the donor core, but decreases when the electron-hole wavefunctions are displaced from the donor core. A small applied E-field acts against the surface potential and pulls the electron-hole densities towards the donor core. Hence, the Coulomb energy is seen to increase at low E-fields and reaches a maximum of 39 meV. A larger applied field now pushes the electrons towards the surface and holes away from the surface (acting opposite the E-field due to the surface potential), and decreases the Coulomb energy monotonically. Unlike the bulk case, the ionization process is gradual (non-abrupt), and the Coulomb energy curve appears smooth even when the hole and one of the electrons ionize at about 10 MV/m. Fig. 6.5b) also shows the transition energy and dipole moments as before, however, these curves are also relatively smoother as the larger E-fields cause a gradual ionization of the electrons and holes.

The ionizing field for the D^0X is depth dependent. Ignoring the donor potential and the inter-particle interactions, the potential drop between the donor location and the surface for electrons and holes is $qF\rho_{e,h}$, where, ρ_e is equal to the donor depth, D, and ρ_h equals the distance to the opposite surface, $W - D$, in which W is the thickness of the channel. Hence, even for a donor close to an interface (small D) the D^0X disassociates already at moderate field strengths by removal of the hole if W is large compared to D. This is qualitatively different from field ionization of the D^0 and D^- states [41, 56].

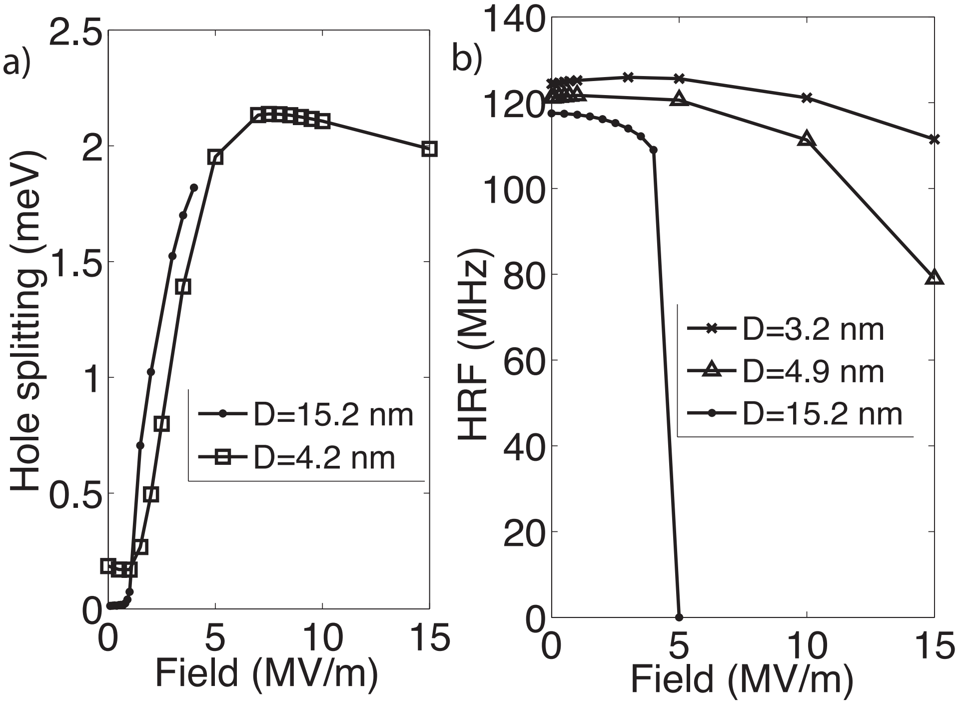

Fig. 6.6. a) D^0X hole splitting with E-fields for a bulk and a subsurface dopant. b) Hyperfine resonance frequencies (HRF) of a P donor below a depth D from the silicon surface with applied electric fields.

In Fig. 6.6, we investigate the other two energy gaps, ΔH and ΔA, that influence the D^0 to D^0X transition energy, as shown in Fig. 6.2b). The proximity to an interface and/or the presence of an applied field changes both the LH and HH splitting ΔH, and the hyperfine resonance energy ΔA. Fig. 6.6a) shows that ΔH increases with E-field both for bulk and interface donors, as the $m_J = \pm 3/2$ and $m_J = \pm 1/2$ states are affected differently, which is consistent with recent studies of Boron acceptors in silicon [95]. Fig. 6.6b) shows the variation of the hyperfine coupling with E-field for donors at various depths. The shift in the hyperfine coupling from a bulk donor can be directly evaluated using the amplitude of the D^0 wavefunction at the donor site, as done in Ref [35]. A for bulk-like donors (D=15.2 nm) varies from the bulk value of 117 MHz at small fields before abruptly diminishing to 0 as the donor ionizes. In contrast, A for donors nearer to an interface can assume a continuous range of values (117 to 0 MHz) depending on the field as the ionization process is gradual. Also, much higher fields in the range of 10-40 MV/m can be applied to donors less than 5 nm deep without completely ionizing the D^0 electron.

There are two factors which we have ignored here, as they lie beyond the scope of this work. First, we have neglected exchange and correlation effects, and treated the problem within the Hartree approximation for computational feasibility. There is a 5 meV difference between the calculated and measured bulk transition energy [24], as shown earlier, which could be due to this approximation. More justification of this approximation is provided in the SM. Second, some residual strain has been reported recently in nanodevices close to the oxide-silicon interface [96]. Although we have not included the effect of local strain in the calculations as it may vary from device to device, qualitatively the effect of strain is similar to that of the electric field. The strain may cause valley-repopulation of the donor, and reduce the weight of the electronic wavefunction in the central-cell. As a result, strain will reduce both the Coulomb energy ΔE and the hyperfine coupling ΔA. In addition, strain removes the light and heavy hole degeneracy, and enhances ΔH, which has been shown in Ref [25].

6.4 Conclusion

We have shown that electric fields and interfaces can affect the transition energies and dipole moments of donor bound excitons in nanodevices quite significantly, and optical addressing techniques for donor qubits need to be aware of these changes to be successful. We have also performed the first atomistic electronic structure calculation of the donor bound exciton in silicon taking into account the full band structure and full donor energy spectrum using spin-resolved atomic orbitals of over a million atoms, and have obtained the three-particle Coulomb energy, hyperfine and hole splittings, all of which contribute to the D^0X transition energy. A detailed understanding of the range of excitation frequencies possible in nanoscale devices and the environmental conditions needed for a stable D^0X helps to extend the optical addressing methods from bulk ensembles to single donor qubits, and may also enable hybrid opto-electric addressing of nuclear spins in silicon with improved fidelity and possible higher temperature operation.

7. SUMMARY AND OUTLOOK

In this work, we provide novel approaches and considerations for designing and optimizing donor-based spin qubits in silicon, in terms of characterization, single- and two-qubit operations, electrical control of spin, spin readout based on quantum tunneling and opto-electric hybrid approach. The work is based on the well calibrated atomistic quantum modeling approach that can capture the full band structure of silicon and the electronic structures of donors in silicon. With this approach, we are able to provide designs with quantitative guidelines, which is helpful for future experiments.

Looking forward, there are several directions to further pursue in order to help experimentalists build better donor-based spin qubits in silicon using an atomistic quantum modeling approach:

1) *Realistic qubit coherence time calculations.* In chapter 4, we develop a method to calculate the decoherence time of electrically controlled donor qubit by using atomistic wavefunctions. In this method, the noise power spectrum is estimated based on existing experiments, but is not calculated directly from the device components in the simulation. Including the noise spectra of different device components such as top metal gates, in-plane gates, single electron transistors, and their influences on the coherence times directly in simulations would help in design, feasibility validation and optimization of scaled-up multiple-qubit devices with all these components present. The noise model development would involve calibration with experimental measurements of noise spectra for different components.

2) *Scalable multiple-qubit modeling.* In chapter 3, we propose a two-qubit design that is alternative to the Kane architecture. The design is relied on electron-electron exchange calculation based on an atomistic full configuration approach, which is computationally expensive. In practice, we can extend the atomistic FCI simulation to

three qubits, but simulations of over three qubits could be very challenging. Therefore, for designing a quantum computer that has many qubits with the help of modeling and simulations, an approach that is more compact and less computationally expensive is needed, which will assist and accelerate the design and experiment iterations. Without losing accuracy, the compact model would be based on a large amount of atomistic simulation results (e.g. binding energies, tunnel couplings, exchange couplings, etc. and their dependencies) as the design basis, and also be able to project unknown parameters by using the existing data and regression or advanced machine learning algorithms. This would break the computation bottleneck of the existing method, and enable the design and modeling of many-qubit devices.

3) *Quantum algorithm simulations based on an atomistic approach.* If the atomistic approach based compact model envisioned above can be realized, with imperfections (e.g. noise) and error correction mechanisms included, we would further pursue quantum algorithm simulations (e.g. Shor's algorithm for factorization used in cryptography) in realistic environments. The idea is to treat the whole qubit system as a black box which is described by the compact model, the dc and ac gate biases and their time dependencies as the input, and the quantum states of the qubits as the output. The time evolution of the effective Hamiltonian described in chapter 4 could serve as a premature version of this approach. A more sophisticated approach would help in validating the feasibility of physical or experimental realization of a quantum algorithm and its further optimization.

REFERENCES

REFERENCES

[1] http://computer.howstuffworks.com/quantum-computer1.htm.

[2] A. M. Tyryshkin, S. Tojo, J. J. L. Morton, H. Riemann, N. V. Abrosimov, P. Becker, H.-J. Pohl, T. Schenkel, M. L. W. Thewalt, K. M. Itoh, and S. A. Lyon, "Electron spin coherence exceeding seconds in high-purity silicon," Nat. Mater. **11**, 143-147 (2012).

[3] E. Kawakami, P. Scarlino, D. R. Ward, F. R. Braakman, D. E. Savage, M. G. Lagally, Mark Friesen, S. N. Coppersmith, M. A. Eriksson, and L. M. K. Vandersypen, "Electrical control of a long-lived spin qubit in a Si/SiGe quantum dot," Nat. Nanotechnol. **9**, 666670 (2014).

[4] M. Veldhorst, J. C. C. Hwang, C. H. Yang, A. W. Leenstra, B. de Ronde, J. P. Dehollain, J. T. Muhonen, F. E. Hudson, K. M. Itoh, A. Morello, and A. S. Dzurak, "An addressable quantum dot qubit with fault-tolerant control-fidelity," Nat. Nanotechnol. **9**, 981985 (2014).

[5] B. E. Kane, "A silicon-based nuclear spin quantum computer," Nature **393**, 133-137 (1998).

[6] A. Laucht, J. T. Muhonen, F. A. Mohiyaddin, R. Kalra, J. P. Dehollain, S. Freer, F. E. Hudson, M. Veldhorst, R. Rahman, G. Klimeck, K. M. Itoh, D. N. Jamieson, J. C. McCallum, A. S. Dzurak, and A. Morello, "Electrically controlling single-spin qubits in a continuous microwave field," Sci. Adv. **(1)**, e1500022 (2015).

[7] C. D. Hill, E. Peretz, S. J. Hile, M. G. House, M. Fuechsle, S. Rogge, M. Y. Simmons, and L. C. L. Hollenberg, "A surface code quantum computer in silicon," Sci. Adv. **1**, no. 9, e1500707 (2015).

[8] S. R. Schofield, N. J. Curson, M. Y. Simmons, F. J. Rue, T. Hallam, L. Oberbeck, and R. G. Clark, "Atomically Precise Placement of Single Dopants in Si," Phys. Rev. Lett. **91**, 136104 (2003).

[9] M. Fuechsle, S. Mahapatra, F. A. Zwanenburg, Mark Friesen, M. A. Eriksson, and M. Y. Simmons, "Spectroscopy of few-electron single-crystal silicon quantum dots," Nat. Nanotechnol. **5**, 502-505 (2010).

[10] H. Büch , S. Mahapatra, R. Rahman, A. Morello, and M. Y. Simmons, "Spin readout and addressability of phosphorus-donor clusters in silicon," Nat. Commun. **4**, 2017 (2013).

[11] Y. Wang, C.-Y. Chen, G. Klimeck, M. Y. Simmons, and R. Rahman, "Characterizing Si:P quantum dot qubits with spin resonance techniques," Sci. Rep. **6**, 31830 (2016).

[12] Y. Wang, A. Tankasala, L. C. L. Hollenberg, G. Klimeck, M. Y. Simmons, and R. Rahman, "Highly tunable exchange in donor qubits in silicon," npj Quantum Information **2**, 16008 (2016).

[13] M. Fuechsle, J. A. Miwa, S. Mahapatra, H. Ryu, S. Lee, O. Warschkow, L. C. L. Hollenberg, G. Klimeck, and M. Y. Simmons, "A single-atom transistor," Nat. Nanotechnol. **7**, 242-246 (2012).

[14] B. Weber, Y. H. M. Tan, S. Mahapatra, T. F. Watson, H. Ryu, R. Rahman, L. C. L. Hollenberg, G. Klimeck, and M. Y. Simmons, "Spin blockade and exchange in Coulomb-confined silicon double quantum dots," Nat. Nanotechnol. **9**, 430-435 (2014).

[15] T. F. Watson, B. Weber, J. A. Miwa, S. Mahapatra, R. M. P. Heijnen, and M. Y. Simmons, "Transport in asymmetrically coupled donor-based silicon triple quantum dots," Nano. Lett. **14**(4), 1830-1835 (2014).

[16] J. J. Pla, K. Y. Tan, J. P. Dehollain, W. H. Lim, J. J. L. Morton, D. N. Jamieson, A. S. Dzurak, and A. Morello, "A single-atom electron spin qubit in silicon," Nature **489**, 541-545 (2012).

[17] J. J. Pla, K. Y. Tan, J. P. Dehollain, W. H. Lim, J. J. L. Morton, F. A. Zwanenburg, D. N. Jamieson, A. S. Dzurak, and A. Morello, "High-fidelity readout and control of a nuclear spin qubit in silicon," Nature **496**, 334-338 (2013).

[18] B. Koiller, X. Hu, and S. D. Sarma, "Exchange in silicon-based quantum computer architecture," Phys. Rev. Lett. **88**, 027903 (2001).

[19] Y. Wang, C.-Y. Chen, G.Klimeck, M. Y. Simmons, and R. Rahman, "All-electrical control of donor-bound electron spin qubits in silicon", arXiv:1703.05370 (2017).

[20] A. Morello, J. J. Pla, F. A. Zwanenburg, K. W. Chan, K. Y. Tan, H. Huebl, M. Mttnen, C. D. Nugroho, C. Yang, J. A. van Donkelaar, A. D. C. Alves, D. N. Jamieson, C. C. Escott, L. C. L. Hollenberg, R. G. Clark, and A. S. Dzurak, "Single-shot readout of an electron spin in silicon," Nature **467**, 687-691 (2010).

[21] J. J. Pla, F. A. Mohiyaddin, K. Y. Tan, J. P. Dehollain, R. Rahman, G. Klimeck, D. N. Jamieson, A. S. Dzurak, and A. Morello, "Coherent Control of a Single ^{29}Si Nuclear Spin Qubit," Phys. Rev. Lett. **113**, 246801 (2014).

[22] L. Childress, M. V. Gurudev Dutt, J. M. Taylor, A. S. Zibrov, F. Jelezko, J. Wrachtrup, P. R. Hemmer, and M. D. Lukin, "Coherent Dynamics of Coupled Electron and Nuclear Spin Qubits in Diamond," Science **314**, 281 (2006).

[23] K. Saeedi, S. Simmons, J. Z. Salvail, P. Dluhy, H. Riemann, N. V. Abrosimov, P. Becker, H.-J. Pohl, J. L. J. Morton, and M. L. W. Thewalt, "Room-temperature quantum bit storage exceeding 39 minutes using ionized donors in silicon-28," Science **342**, 830-833 (2013).

[24] M. Steger, K. Saeedi, M. L. W. Thewalt, J. J. L. Morton, H. Riemann, N. V. Abrosimov, P. Becker, H.-J. Pohl, "Quantum Information Storage for over 180 s Using Donor Spins in a ^{28}Si Semiconductor Vacuum," Science **336**, 1280-1283 (2012).

[25] C. C. Lo, M. Urdampilleta, P. Ross, M. F. Gonzalez-Zalba, J. Mansir, S. A. Lyon, M. L. W. Thewalt, and J. J. L. Morton, "Hybrid opticalelectrical detection of donor electron spins with bound excitons in silico," Nat. Mater. **14**, 490-494 (2015).

[26] A. Yang, M. Steger, T. Sekiguchi, M. L. W. Thewalt, T. D. Ladd, K. M. Itoh, H. Riemann, N. V. Abrosimov, P. Becker, and H.-J. Pohl, "Simultaneous Subsecond Hyperpolarization of the Nuclear and Electron Spins of Phosphorus in Silicon by Optical Pumping of Exciton Transitions," Phys. Rev. Lett. **102**, 257401 (2009).

[27] A. Yang, M. Steger, D. Karaiskaj, M. L. W. Thewalt, M. Cardona, K. M. Itoh, H. Riemann, N. V. Abrosimov, M. F. Churbanov, A. V. Gusev, A. D. Bulanov, A. K. Kaliteevskii, O. N. Godisov, P. Becker, H.-J. Pohl, J. W. Ager, III, and E. E. Haller, "Optical Detection and Ionization of Donors in Specific Electronic and Nuclear Spin States," Phys. Rev. Lett. **97**, 227401 (2006).

[28] C. Yin, M. Rancic, G. G. de Boo, N. Stavrias, J. C. McCallum, M. J. Sellars, and S. Rogge, "Optical addressing of an individual erbium ion in silicon," Nature **497**, 91 (2013).

[29] L. C. L. Hollenberg, A. D. Greentree, A. G. Fowler, and C. J. Wellard, "Two-dimensional architectures for donor-based quantum computing," Phys. Rev. B **74**, 045311 (2006).

[30] F. A. Zwanenburg, A. S. Dzurak, A. Morello, M. Y. Simmons, L. C. L. Hollenberg, G. Klimeck, S. Rogge, S. N. Coppersmith, and M. A. Eriksson, "Silicon quantum electronics," Rev. Mod. Phys. **85**, 961 (2013).

[31] M. Veldhorst, C. H. Yang, J. C. C. Hwang, W. Huang, J. P. Dehollain, J. T. Muhonen, S. Simmons, A. Laucht, F. E. Hudson, K. M. Itoh, A. Morello, and A. S. Dzurak, "A two-qubit logic gate in silicon," Nature **526**, 410414 (2015).

[32] J. G. Keizer, S. R. McKibbin, and M. Y. Simmons, "The impact of dopant segregation on the maximum carrier density in Si:P multilayers," ACS Nano **9**(7), 70807084 (2015).

[33] E. B. Hale, and R. L. Mieher, "Shallow Donor Electrons in Silicon. I. Hyperfine Interactions from ENDOR Measurements," Phys. Rev. **184**, 739 (1969).

[34] S. H. Park, R. Rahman, G. Klimeck, and L. C. L. Hollenberg, "Mapping Donor Electron Wave Function Deformations at a Sub-Bohr Orbit Resolution," Phys. Rev. Lett. **103**, 106802 (2009).

[35] R. Rahman, C. J. Wellard, F. R. Bradbury, M. Prada, J. H. Cole, G. Klimeck, and Lloyd C. L. Hollenberg, "High precision quantum control of single donor spins in silicon," Phys. Rev. Lett. **99**, 036403 (2007).

[36] G. Klimeck, F. Oyafuso, T. B. Boykin, R. C. Bowen, and P von Allmen, "Development of a nanoelectronic 3-D (NEMO 3-D) simulator for multimillion atom simulations and its application to alloyed quantum dots," CMES **3**(5), 601-642 (2002).

[37] T. B. Boykin, G. Klimeck, and F. Oyafuso, "Valence band effective-mass expressions in the sp3d5s* empirical tight-binding model applied to a Si and Ge parametrization," Phys. Rev. B **69**, 115201 (2004).

[38] S. Lee, F. Oyafuso, P. Allmen, and G. Klimeck, "Boundary conditions for the electronic structure of finite-extent embedded semiconductor nanostructures," Phys. Rev. B **69**, 045316 (2004).

[39] S. Ahmed, N. Kharche, R. Rahman, M. Usman, S. Lee, H. Ryu, H. Bae, S. Clark, B. Haley, M. Naumov, F. Saied, M. Korkusinski, R. Kennel, M. McLennan, T. B. Boykin, and G. Klimeck, "Multimillion Atom Simulations with NEMO 3-D," In Meyers, Robert (Ed.) Encyclopedia of Complexity and Systems Science vol. 6, 57455783 Springer New York 2009.

[40] J. Salfi, J. Mol, R. Rahman, G. Klimeck, M. Y. Simmons, L. C. L. Hollenberg, and S. Rogge, "Spatially resolving valley quantum interference of a donor in silicon," Nat. Mater. **13**, 605-610 (2014).

[41] R. Rahman, G. P. Lansbergen, J. Verduijn, G. C. Tettamanzi, S. H. Park, N. Collaert, S. Biesemans, G. Klimeck, L. C. L. Hollenberg, and S. Rogge, "Electric field reduced charging energies and two-electron bound excited states of single donors in silicon," Phys. Rev. B **84**, 115428 (2011).

[42] Y.-L. Hsueh, H. Büch, Y. Tan, Y. Wang, L. C. L. Hollenberg, G. Klimeck, Michelle Y. Simmons, and Rajib Rahman, "Spin-lattice relaxation times of single donors and donor clusters in silicon," Phys. Rev. Lett. **113**, 246406 (2014).

[43] F. Mohiyaddin, R. Rahman, R. Kalra, G. Klimeck, L. C. L. Hollenberg, J. J. Pla, A. S. Dzurak, and A. Morello, "Noninvasive spatial metrology of single-atom devices," Nano Lett. **13**(5), 19031909 (2013).

[44] J. T. Muhonen, J. P. Dehollain, A. Laucht, F. E. Hudson, R. Kalra, T. Sekiguchi, K. M. Itoh, D. N. Jamieson, J. C. McCallum, A. S. Dzurak, and A. Morello, "Storing quantum information for 30 seconds in a nanoelectronic device," Nat. Nanotechnol. **9**, 986-991 (2014).

[45] R. Kalra, A. Laucht, C. D. Hill, and A. Morello, "Robust two-qubit gates for donors in silicon controlled by hyperfine interactions," Phys. Rev. X **4**, 021044 (2014).

[46] C. D. Sherrill, and H. F. Schaefer III, "The configuration interaction method: advances in highly correlated approaches," Adv. Quantum Chem. **34**, 143-269 (1999).

[47] J. R. Petta, A. C. Johnson, J. M. Taylor, E. A. Laird, A. Yacoby, M. D. Lukin, C. M. Marcus, M. P. Hanson, and A. C. Gossard, "Coherent manipulation of coupled electron spins in semiconductor quantum dots," Science **309**, 2180-2184 (2005).

[48] R. Rahman, E. Nielsen, R. P. Muller, and M. S. Carroll, "Voltage controlled exchange energies of a two-electron silicon double quantum dot with and without charge defects in the dielectric," Phys. Rev. B **85**, 125423 (2012).

[49] The charge configuration of the system is denoted as (M,N), where M indicates the number of electrons on the left dot, and N the right dot.

[50] C. J. Wellard, L. C. L. Hollenberg, L. M. Kettle, and H.-S. Goan, “Voltage control of exchange coupling in phosphorus doped silicon,” J. Phy.: Condens. Matter **16**, 5697 (2004).

[51] C. J. Wellard, L. C. L. Hollenberg, F. Parisoli, L. M. Kettle, H.-S. Goan, J. A. L. McIntosh, and D. N. Jamieson, “Electron exchange coupling for single-donor solid-state spin qubits, Phys. Rev. B **68**, 195209 (2003).

[52] G. Pica, B. W. Lovett, R. N. Bhatt, and S. A. Lyon, “Exchange coupling between silicon donors: The crucial role of the central cell and mass anisotropy,” Phys. Rev. B **89**, 235306 (2014).

[53] L. M. Kettle, H-.S. Goan, and S. C. Smith, “Molecular orbital calculations of two-electron states for P-donor solid-state spin qubits,” Phys. Rev. B **73**, 115205 (2006).

[54] M. F. Gonzalez-Zalba, A. Saraiva, M. J. Caldern, D. Heiss, B. Koiller, and A. J. Ferguson, “An exchange-coupled donor molecule in silicon,” Nano Lett. **14**, 5672-5676 (2014).

[55] W. Kohn, and J. M. Luttinger, “Theory of Donor States in Silicon,” Phys. Rev. **98**, 915 (1955).

[56] R. Rahman, G. P. Lansbergen, S. H. Park, V. Verduijn, G. Klimeck, S. Rogge, and L. C. L. Hollenberg, “Orbital Stark effect and quantum confinement transition of donors in silicon,” Phys. Rev. B **80**, 165314 (2009).

[57] R. Rahman, S. H. Park, T. B. Boykin, G. Klimeck, S. Rogge, and L. C. L. Hollenberg, “Gate-induced g-factor control and dimensional transition for donors in multivalley semiconductors,” Phys. Rev. B **80**, 155301 (2009).

[58] A. Tankasala, Y. Wang, G. Klimeck, and R. Rahman, “Atomistic configuration interaction simulations of two-electron states of donors in silicon,” APS March Meeting 2015, Vol. 60, No. 1, A37.00011.

[59] “Synopsys Sentaurus Semiconductor TCAD Software,” East Middlefield Road, Mountain View, CA 94043 USA.

[60] M. D. Shulman, O. E. Dial, S. P. Harvey, H. Bluhm, V. Umansky, and A. Yacoby, “Demonstration of entanglement of electrostatically coupled singlet-triplet qubits,” Science **336**, 202-205 (2012).

[61] Y. Kato, R. C. Myers, D. C. Driscoll, A. C. Gossard, J. Levy, and D. D. Awschalom, “Gigahertz Electron Spin Manipulation Using Voltage-Controlled g-Tensor Modulation,” Science **299**, 1201-1204 (2003).

[62] E. A. Laird, C. Barthel, E. I. Rashba, C. M. Marcus, M. P. Hanson, and A. C. Gossard, “Hyperfine-Mediated Gate-Driven Electron Spin Resonance,” Phys. Rev. Lett. **99**, 246601 (2007).

[63] J. Pingenot, C. E. Pryor, and M. E. Flatt, “Method for full Bloch sphere control of a localized spin via a single electrical gate,” Appl. Phys. Lett. **92**, 222502 (2008).

[64] Y. Tokura, W. G. van der Wiel, T. Obata, and S. Tarucha, "Coherent Single Electron Spin Control in a Slanting Zeeman Field," Phys. Rev. Lett. **96**, 047202 (2006).

[65] T. F. Watson, B. Weber, M. G. House, H. Bch, and M.Y. Simmons, "High-Fidelity Rapid Initialization and Read-Out of an Electron Spin via the Single Donor D^- Charge State," Phys. Rev. Lett. **115**, 166806 (2015).

[66] S. Shamim, B. Weber, D. W. Thompson, M. Y. Simmons, and A. Ghosh,"Ultralow-Noise Atomic-Scale Structures for Quantum Circuitry in Silicon," Nano Lett. **16**(9), 5779-5784 (2016).

[67] S. Shamim, S. Mahapatra, G. Scappucci, W.M. Klesse, M.Y. Simmons, and A. Ghosh, "Spontaneous Breaking of Time-Reversal Symmetry in Strongly Interacting Two-Dimensional Electron Layers in Silicon and Germanium," Phys. Rev. Lett. **112**, 236602 (2014).

[68] T. Schenkel, J. A. Liddle, A. Persaud, A. M. Tyryshkin, S. A. Lyon, R. de Sousa, K. B. Whaley, J. Bokor, J. Shangkuan and I. Chakarov, "Electrical activation and electron spin coherence of ultralow dose antimony implants in silicon," Appl. Phys. Lett. **88**, 112101 (2006).

[69] S.-Y. Paik, S.-Y. Lee, W. J. Baker, D. R. McCamey, and C. Boehme, "T_1 and T_2 spin relaxation time limitations of phosphorous donor electrons near crystalline silicon to silicon dioxide interface defects," Phys. Rev. B **81**, 075214 (2010).

[70] A. G. Fowler, S. J. Devitt, and L. C. L. Hollenberg, "Implementation of Shor's Algorithm on a Linear Nearest Neighbour Qubit Array," Quantum Inf. Comput. **4**, 237245 (2004).

[71] G. Tosi, F. A. Mohiyaddin, S. B. Tenberg, R. Rahman, G. Klimeck, and A. Morello, "Silicon quantum processor with robust long-distance qubit couplings," arXiv:1509.08538 (2015).

[72] J. R. Petta, J. M. Taylor, A. C. Johnson, A. Yacoby, M. D. Lukin, C. M. Marcus, M. P. Hanson, and A. C. Gossard, "Dynamic Nuclear Polarization with Single Electron Spins," Phys. Rev. Lett. **100**, 067601 (2008).

[73] A. V. Kuhlmann, J. Houel, A. Ludwig, L. Greuter, D. Reuter, A. D. Wieck, M. Poggio, and R. J. Warburton, "Charge noise and spin noise in a semiconductor quantum device," Nat. Phys. **9**, 570575 (2013).

[74] L. Chirolli and G. Burkard, "Decoherence in Solid State Qubits," Adv. in Phys. 57:3, 225-285 (2008).

[75] P. Huang and X. Hu, "Electron spin relaxation due to charge noise," Phys. Rev. B **89**, 195302 (2014).

[76] B. Weber, H. Ryu, Y.-H. M. Tan, G. Klimeck, and M. Y. Simmons, "Limits to Metallic Conduction in Atomic-Scale Quasi-One-Dimensional Silicon Wires," Phys. Rev. Lett. **113**, 246802 (2014).

[77] H. Büch, M. Fuechsle, W. Baker, M. G. House, and M. Y. Simmons, "Quantum dot spectroscopy using a single phosphorus donor," Phys. Rev. B **92**, 235309 (2015).

[78] L. C. L. Hollenberg, A. S. Dzurak, C. Wellard, A. R. Hamilton, D. J. Reilly, G. J. Milburn, and R. G. Clark, "Charge-based quantum computing using single donors in semiconductors," Phys. Rev. B **69**, 113301 (2004).

[79] B. Weber, S. Mahapatra, H. Ryu, S. Lee, A. Fuhrer, T. C. G. Reusch, D. L. Thompson, W. C. T. Lee, G. Klimeck, L. C. L. Hollenberg, and M. Y. Simmons, "Ohms Law Survives to the Atomic Scale," Science **335**, 64 (2012).

[80] S. Mahapatra, H. Büch, and M. Y. Simmons, "Charge Sensing of Precisely Positioned P Donors in Si," Nano letters **11**(10), 4376-4381 (2011).

[81] M. G. House, E. Peretz, J. G. Keizer, S. J. Hile, and M. Y. Simmons, "Single-charge detection by an atomic precision tunnel junction," Appl. Phys. Lett. **104**, 113111 (2014).

[82] J. P. Dehollain, J. T. Muhonen, K. Y. Tan, A. Saraiva, D. N. Jamieson, A. S. Dzurak, and A. Morello, "Single-Shot Readout and Relaxation of Singlet and Triplet States in Exchange-Coupled ^{31}P Electron Spins in Silicon," Phys. Rev. Lett. **112**, 236801 (2014).

[83] H. Büch, "Readout and addressability of Si:P qubits with the prospect of scalability," Doctoral thesis (2014).

[84] D. W. Drumm, L. C. L. Hollenberg, M. Y. Simmons, and M. Friesen, "Effective mass theory of monolayer δ doping in the high-density limit," Phys. Rev. B **85**, 155419 (2012).

[85] D. J. Carter, O. Warschkow, N. A. Marks, and D. R. McKenzie, "Electronic structure models of phosphorus δ-doped silicon," Phys. Rev. B **79**, 033204 (2009).

[86] S. Lee, H. Ryu, H. Campbell, L. C. L. Hollenberg, M. Y. Simmons, and G. Klimeck, "Electronic structure of realistically extended atomistically resolved disordered Si:P δ-doped layers," Phys. Rev. B **84**, 205309 (2011).

[87] S. Datta, "Atoms to Transistors," Cambridge (2007).

[88] J. Bardeen, "Tunnelling from a Many-Particle Point of View," Phys. Rev. Lett. **6**, 57 (1961).

[89] G. Klimeck, S. S. Ahmed, H. Bae, N. Kharche, S. Clark, B. Haley, S. Lee, M. Naumov, H. Ryu, F. Saied, M. Prada, M. Korkusinski, T. B. Boykin, R. Rahman, "Atomistic Simulation of Realistically Sized Nanodevices Using NEMO 3-D−Part I: Models and Benchmarks," IEEE Trans. Electron Devices **54**, 2079 (2007).

[90] K. F. Mak, K. He, C. Lee, Gwan Hyoung Lee, J. Hone, T. F. Heinz, and J. Shan, "Tightly bound trions in monolayer MoS_2," Nat. Mater. **12**, 207-211 (2013).

[91] A. Chernikov, T. C. Berkelbach, H. M. Hill, A. Rigosi, Y. Li, O. B. Aslan, D. R. Reichman, M. S. Hybertsen, and T. F. Heinz, "Exciton Binding Energy and Nonhydrogenic Rydberg Series in Monolayer WS_2," Phys. Rev. Lett. **113**, 076802 (2014).

[92] W. Schmid, "Auger lifetimes for excitons bound to neutral donors and acceptors in Si," Phys. Stat. Sol. **84**, 529 (1977).

[93] D. Sleiter, N. Y. Kim, K. Nozawa, T. D. Ladd, M. L. W. Thewalt, and Y. Yamamoto, "Quantum Hall charge sensor for single-donor nuclear spin detection in silicon," New J. Phys., **12**, 093028 (2010).

[94] G. P. Lansbergen, R. Rahman, C. J. Wellard, I. Woo, J. Caro, N. Collaert, S. Biesemans, G. Klimeck, L. C. L. Hollenberg, and S. Rogge, "Gate-induced quantum-confinement transition of a single dopant atom in a silicon FinFET," Nat. Phys. **4**, 656-661 (2008).

[95] J. Mol, J. Salfi, R. Rahman, Y. Hsueh, J. A. Miwa, G. Klimeck, M. Y. Simmons, S. Rogge, "Interface-induced heavy-hole/light-hole splitting of acceptors in silicon," Appl. Phys. Lett. **106**, 203110 (2015).

[96] T. Thorbeck, and N. M. Zimmerman, "Formation of strain-induced quantum dots in gated semiconductor nanostructures," AIP Advances **5**, 087107 (2015).

[97] X. Hu, B. Koiller, and S. D. Sarmar, "Charge qubits in semiconductor quantum computer architecture: Tunnel coupling and decoherence," Phys. Rev. B **71**, 235332 (2005).

[98] R. Rahman, J. Verduijn, Y. Wang, C. Yin, G. De Boo, G. Klimeck, and S. Rogge, "Bulk and sub-surface donor bound excitons in silicon under electric fields," arXiv:1510.00065 (2015).

APPENDICES

A. TIGHT BINDING APPROACH AND FULL CONFIGURATION INTERACTION METHOD

In our TB approach, the full Hamiltonian of silicon and donor atoms is represented by the $sp^3d^5s^*$ atomistic basis with nearest neighbor interactions [89]. This method expresses the single electron wavefunction as a linear combination of the atomic orbitals. For a silicon unit cell, the model reproduces the full band structure including the correct conduction band and valence band extrema, effective masses, and band gap [37]. A donor is modeled by the Coulomb potential of a positive charge screened by the silicon dielectric constant, and an onsite cut-off potential U_0, which is adjusted to reproduce the ground state binding energy of 45.6 meV below the conduction band for a P donor in Si [35]. It has been shown in earlier works that this model captures the central-cell correction, and produces correct wavefunction symmetries and energy splittings of the donor states [39]. The computed ground state wavefunction also showed excellent agreement with real and momentum space images of the donor obtained by STM experiments [40]. Using this model, the single electron molecular orbitals of the two donors are obtained by

$$H_{1,2} = H_0 + H_L + H_R + e\vec{E} \cdot \vec{r}, \tag{A.1}$$

where $H_{1,2}$ represents the single electron Hamiltonian for electron 1 or 2, H_0 is the crystal Hamiltonian of millions of Si atoms, H_L and H_R are the left and right donor potential energy respectively, and the last term is the potential energy of a detuning electric field $\vec{E}$. The eigen problem $H_i\Psi = \epsilon\Psi$ is solved by a parallel block Lanczos algorithm to obtain a set of molecular orbitals of the P-P$^+$ system, $\{\Psi_1, \Psi_2, ..., \Psi_m\}$ corresponding to energies $\{\epsilon_1, \epsilon_2, ..., \epsilon_m\}$ where the index goes from the ground state 1 to the excited state m.

Using the m molecular orbitals, all possible two-electron Slater determinants (SD) are constructed to represent non spin-adapted anti-symmetric electron configurations of electrons occupying molecular orbitals i and j as $SD_{ij} = \frac{1}{\sqrt{2}}[\Psi_i(\vec{r}_1)\Psi_j(\vec{r}_2) - \Psi_j(\vec{r}_1)\Psi_i(\vec{r}_2)]$, where $\vec{r}_1$ and $\vec{r}_2$ are the coordinates of electron 1 and 2. We employ a full configuration interaction (FCI) scheme, which means that we include all possible single and double excitations of the system for the two-electron problem. We found that about 12 single electron molecular orbitals (24 spin states) are needed to achieve convergence, which leads to the number of SDs being C^2_{24}. The two-electron Hamiltonian is given as

$$H_{2e} = H_1 + H_2 + \frac{e^2}{4\pi\epsilon(|\vec{r}_1 - \vec{r}_2|)}\frac{1}{|\vec{r}_1 - \vec{r}_2|}, \tag{A.2}$$

where the last term denotes the Coulomb interaction between electrons 1 and 2 with the dielectric function being $\epsilon(|\vec{r}_1 - \vec{r}_2|)$. If this term is evaluated in the basis of the SDs, the familiar Coulomb (C) and exchange (K) integrals are obtained, as follows,

$$\langle SD_{ij}|\frac{e^2}{4\pi\epsilon(|\vec{r}_1 - \vec{r}_2|)}\frac{1}{|\vec{r}_1 - \vec{r}_2|}|SD_{pq}\rangle = C_{ij,pq} - K_{ij,pq}, \tag{A.3}$$

where $i, j, p, q \leq m$. The first and the second terms on the right hand side are the $C_{ij,pq}$ and $K_{ij,pq}$ integrals:

$$C_{ij,pq} = \iint d\vec{r}_1 d\vec{r}_2 \Psi^*_i(\vec{r}_1)\Psi^*_j(\vec{r}_2)\frac{e^2}{4\pi\epsilon(|\vec{r}_1 - \vec{r}_2|)}\frac{1}{|\vec{r}_1 - \vec{r}_2|}\Psi_p(\vec{r}_1)\Psi_q(\vec{r}_2), \tag{A.4}$$

$$K_{ij,pq} = \iint d\vec{r}_1 d\vec{r}_2 \Psi^*_i(\vec{r}_1)\Psi^*_j(\vec{r}_2)\frac{e^2}{4\pi\epsilon(|\vec{r}_1 - \vec{r}_2|)}\frac{1}{|\vec{r}_1 - \vec{r}_2|}\Psi_q(\vec{r}_1)\Psi_p(\vec{r}_2). \tag{A.5}$$

The solution of Eq. A.2 in the basis of SDs yields the total energies and wavefunctions of the two-electron system. The computed wavefunctions are spin singlets and triplets. The wavefunctions appear as linear combinations of SDs with coefficients c_{ij}, given as $\Psi_{2e} = \sum_{i,j} c_{ij} SD_{ij}$, where $i, j \leq m$ and $i \neq j$.

B. MITIGATED EXCHANGE OSCILLATIONS IN 2P-1P QUBITS: WAVEFUNCTION OF 2P CLUSTER AND ITS VALLEY RE-POPULATION

The exchange oscillations directly arise from the spatial oscillations of the wavefunctions due to the valley components. A further analysis of the atomistic wavefunction of the 2P cluster shows that several factors contribute to making the wavefunction smoother, which in turn suppresses the exchange oscillations. In particular, the 2P cluster wavefunctions have 1) excited orbital contributions, 2) Reduced Bohr radii, and 3) reduced X-Y valley weights, as shown below.

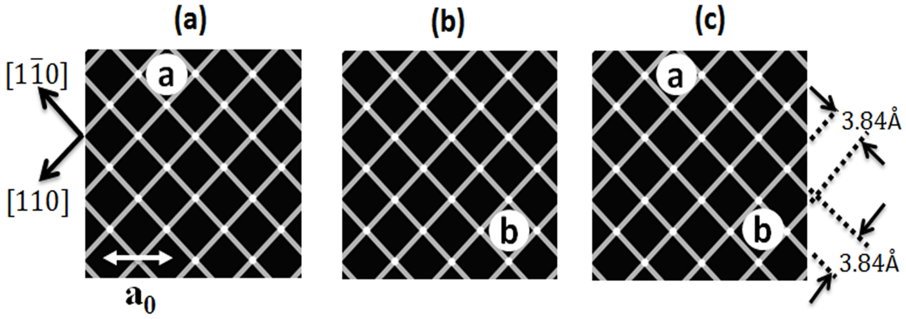

Fig. B.1. Donor locations of three systems (a), (b) (single donors), and (c) (a 2P cluster). The squares represent the silicon atoms on the (001) atomic plane and the white filled circles labeled a and b represent the substituting P atoms. The origin is defined as O. $a_0/\sqrt{2}$=0.384nm, where a_0 is the lattice constant of silicon (~0.543nm).

To explain the mitigated exchange oscillations in 2P-1P qubits, we analyzed the 2P wavefunction by decomposing it into isolated single donor wavefunctions. The three systems shown in Fig. B.1(a), (b) and (c) are studied. We solved the ground-state wavefunctions of these three systems using atomistic tight-binding approach, and denote these as $|\Psi_a\rangle$,$|\Psi_b\rangle$ and $|\Psi\rangle$ for (a), (b), and (c) respectively. We define the ideal bonding state formed by $|\Psi_a\rangle$ and $|\Psi_b\rangle$ as $|\Psi_{ab}\rangle$, where $|\Psi_{ab}\rangle = 1/\sqrt{2(1+S)}(|\Psi_a\rangle + |\Psi_b\rangle)$ (S is the overlap integral: $S = \langle\Psi_a|\Psi_b\rangle$). We evaluated $|\langle\Psi|\Psi_{ab}\rangle|^2 = 0.838$, which indicates that ~84% of the 2P wavefunction is composed of the 1s(A1) ground states of two isolated donors (Fig. B.1(a) and (b)), and the other ~16% is composed of higher orbital states.

Secondly, using the Kohn-Luttinger formula, the 2P electron wavefunction can be expressed as [97]:

$$\Psi_{2P}(x,y,z) = \frac{1}{\sqrt{2(1+S)}} \sum_{\mu}^{\pm x,\pm y,\pm z} \frac{\alpha_\mu u_\mu(\vec{r})}{\sqrt{\pi/R_B^3(2P)}} [e^{-|\vec{r}-\vec{r_a}|/R_B(2P)} e^{i\vec{k_\mu}(\vec{r}-\vec{r_a})} + e^{-|\vec{r}-\vec{r_b}|/R_B(2P)} e^{i\vec{k_\mu}(\vec{r}-\vec{r_b})}], \quad \text{(B.1)}$$

where μ is the index of the six conduction band valleys (x,y,z) of silicon, α_μ is the corresponding weight of the valleys, $R_B(2P)$ is the Bohr radius of the 2P cluster (assumed to be isotropic here for simplicity), k_μ is the corresponding wave vector of the valleys, $\vec{r}$ is the position vector, $\vec{r_a}, \vec{r_b}$ denotes the positions of the two donors, and $u_\mu(\vec{r})$ is the Bloch function. The oscillations are damped by the factor $e^{-r/R_B(2P)}$ because of the reduction of the Bohr radius of a 2P cluster (~1nm) compared to a 1P donor (~2 nm) computed from atomistic tight-binding approach [42].

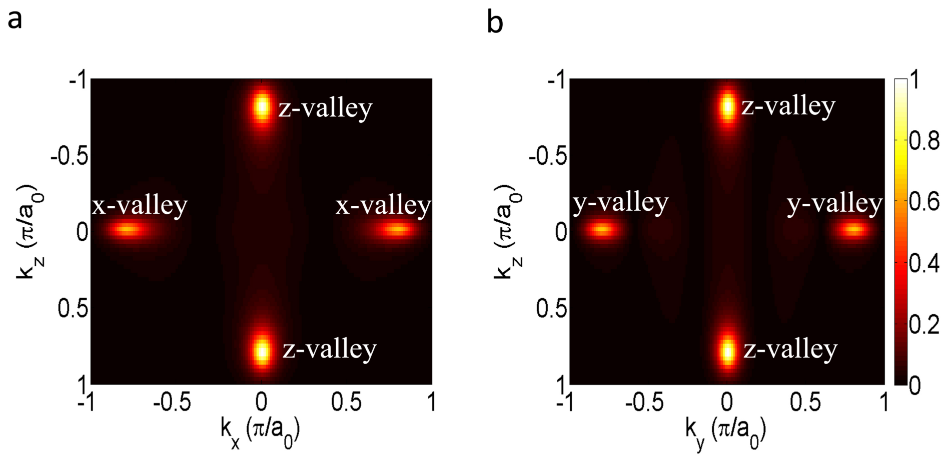

Fig. B.2. The momentum space components of $|\Psi\rangle$.

Thirdly, we also plot the momentum space components of the 2P wavefunction $|\Psi\rangle$ in Fig. B.2. As can be seen, the weights of the z-valleys are dominant as shown by the brighter colors of the z-valleys compared to the x- and y- valleys while the x- and y-valley contributions are relatively suppressed. As a result, the wavefunction components containing $e^{ik_{\pm z}z}$ contribute the largest to the overall wavefunction. A displacement of the other (1P) donor on the X-Y plane affects the x- and y-valley components. Since the dominant interference terms do not arise from these components, the exchange oscillations are suppressed as a function of donor separations in the X-Y plane.

C. COMPARISON OF TUNING EXCHANGE COUPLING WITH KANE'S J-GATE AND DETUNING GATES

In this section, we demonstrate the exchange tunability of the 1P-1P and 2P-1P systems in realistic gated device structures as shown in Fig. 3.1. We compare the Kane device (Fig. 3.1a) and the detuning gate designs (Fig. 3.1b and c). In Fig. 3.1a, the widths of the A-gates and the J-gates are 6 nm. The dark red region is a SiO_2 layer with 3nm thickness. The light pink region is undoped silicon that hosts the donor qubits. The donor qubits are separated by 15 nm, and placed $\sim$10 nm below the Si/SiO_2 interface directly beneath the center of each A-gate. To tune the exchange coupling, the J-gate bias is varied from -1 V to 1 V while the A-gates are grounded. The electrostatic potential of the device is solved by a technology computer aided design tool Sentaurus [59] and then coupled to the atomistic TB-FCI calculations. Fig. C.1(a) shows the exchange coupling of the 1P-1P and 2P-1P systems as a function of the J-gate bias. By applying negative biases, the exchange coupling first decreases (0 V to -0.6 V) as the two electron wavefunctions are pushed apart, resulting in a reduction of the wavefunction overlap. Then the exchange coupling reaches a plateau (-0.6 V to -1 V) as the overlap of the wavefunctions is not affected by the negative potential and is largely determined by the spatial separation of the two qubits. With positive J-gate biases, the exchange coupling first increases (0 V to 0.5 V) because the wavefunctions are pulled toward the J-gate, and the overlap increases as a result. By further increasing the J-gate bias, for the 1P-1P system, the exchange coupling first decreases (at 0.6 V) because one of the donor electrons is ionized to the Si/SiO_2 interface whereas the other one is still bound. Then the exchange coupling drastically increases (0.7 V to 1 V) because both electrons are ionized to the interface causing the overlap to increase sharply. However, in this regime, the interface electrons are not distinguishable any more and cannot be utilized as qubit electrons. For the 2P-1P system, the exchange coupling starts decreasing at 0.6 V as the 1P electron is pulled to the interface while the 2P electron is still bound. The interface electron is prone to interface defects and gate noise, which can significantly undermine the coherence time and the qubit performance. We are only interested in the donor-bound regimes where the exchange coupling can only be tuned by a factor of ∼30 (-1 V to 0.5 V) under Kane's architecture for both the 1P-1P and the 2P-1P systems.

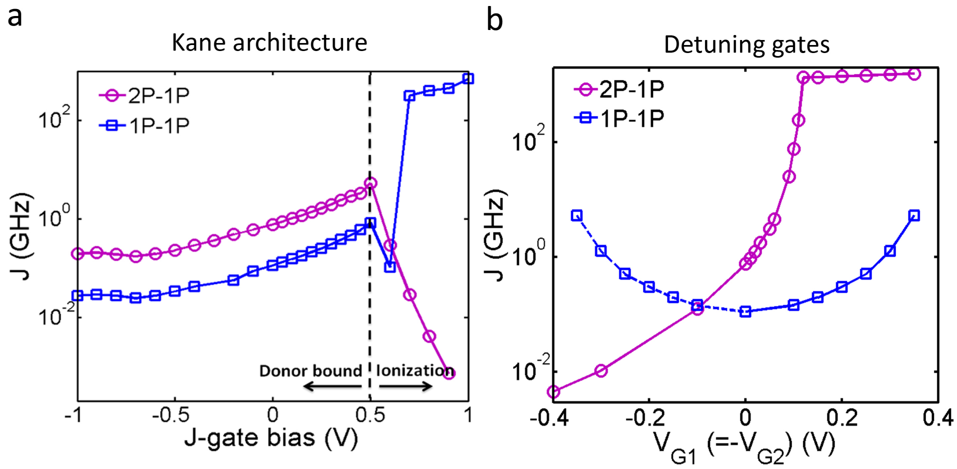

Fig. C.1. Comparison of the tunability of exchange coupling with Kane's structure and detuning gate structures. (a) Exchange energy as a function of J-gate biases for the 1P-1P and the 2P-1P systems. The two qubits are separated by 15 nm in the [100] direction. The corresponding device structure is shown in Fig. 3.1a in the main text. (b) Exchange coupling as a function of top-gate biases for the 1P-1P and the 2P-1P systems. The two qubits are separated by 15 nm in the [100] direction. The device structure is shown in Fig. 3.1b in the main text.

In comparison, we also investigate the exchange tunability with top and in-plane detuning gates. In Fig. 3.1b, G_1 and G_2 are two top gates that are 6 nm wide. The donor qubits are placed beneath the center of G_1 and G_2, respectively. They are separated by 15 nm and buried ∼10 nm below the Si/SiO$_2$ interface. Gate biases of opposite polarity are applied on G_1 and G_2 to detune the system. Fig. C.1(b) shows the exchange coupling as a function of the detuning gate biases in both the 2P-1P and the 1P-1P systems. For the 2P-1P system, a similar exchange tunability (5 orders of magnitude) as the uniform field detuning case (shown in Fig. 3.3 of the main text) is obtained. We find that the in-plane detuning gate structure (Fig. 3.1c) provides similar tunability as well (not shown). For the 1P-1P system, spatially varying electric fields applied from the top gates can tune the exchange coupling by a factor of ∼50 (from 0.13 GHz to 53.4 GHz) as shown in Fig. C.1(b). Compared with the uniform field detuning case (tunability of a factor of 5), the top-gate structure is more promising. The exchange tunability in the 1P-1P system will therefore be limited by the magnitude of the electric field realizable in practice. Better performance could possibly be achieved with more rigorous device geometry and control optimization.

In summary, the J-gates in Kane's architecture provide limited exchange tunability for both the 1P-1P and the 2P-1P systems. Larger exchange tunability can be achieved with the detuning gate scheme proposed here. This work therefore provides useful two-qubit design guidelines for future donor qubit experiments.

D. SPECTRUM FUNCTIONS OF CHARGE NOISE FIELDS

Following Ref. [75], we investigate three types of charge noise. The $1/f^{\alpha}$ noise field spectrum is expressed as:

$$S_E(\omega) = \frac{N}{\omega^{\alpha}}, \tag{D.1}$$

where N is the noise field strength in $(V/m)^2$. In this work, we estimate N based on Ref. [73], where the root-mean-square electric field noise is $F_{r.m.s} = 46$ V/m. Then $N = (\sqrt{2}F_{r.m.s})^2 = 4232\ (V/m)^2$. We assume the bandwidth starts at 0.1 Hz also in line with Ref. [73], and $\alpha = 1$ in the calculations.

The Johnson noise field spectrum is:

$$S_E(\omega) = \frac{2\xi\omega\hbar^2}{1 + (\omega/\omega_R)^2}/(el_0)^2, \tag{D.2}$$

where $\xi = R/R_k$, R_k is the fundamental quantum resistance h/e^2, R is the circuit resistance, and $\omega_R = 1/RC$ is the cutoff frequency. R is estimated based on Ref. [76]. In this work, we assume the gate length (l_g) is 100 nm and the gate width is 6 nm (w) which leads to 18 conducting modes (M, number of modes) [76]. As estimated in Ref. [76], the mean-free-path (λ) of such a wire is ∼6 nm. Hence, R in this work is calculated by $1/R = e^2/h \cdot M \cdot \lambda/(\lambda + l_g)$. l_0 is the distance between the qubit and the noise source, and we assume $l_0 = 65$ nm based on experimental devices [65]. C is estimated based on Ref. [77], where the donor-gate capacitance is 0.6 aF for a separation ∼35 nm. Therefore, C in this work is evaluated as $35nm/65nm \cdot 0.36aF = 0.17aF$.

The evanescent wave Johnson noise (EWJN) field spectrum can be expressed as:

$$S_E(\omega) = \frac{\hbar\omega}{8z^3\sigma}, \tag{D.3}$$

where σ is the conductivity of the gates. We extract σ from Ref. [76] where the wire length (l_w) is 47 nm. We assume the thickness of the wire (t_w) to be 2 nm considering donor diffusion and segregation, then the conductivity can be expressed as $4.8\frac{e^2}{h}\frac{l_w+\lambda}{w \cdot t_w}$.

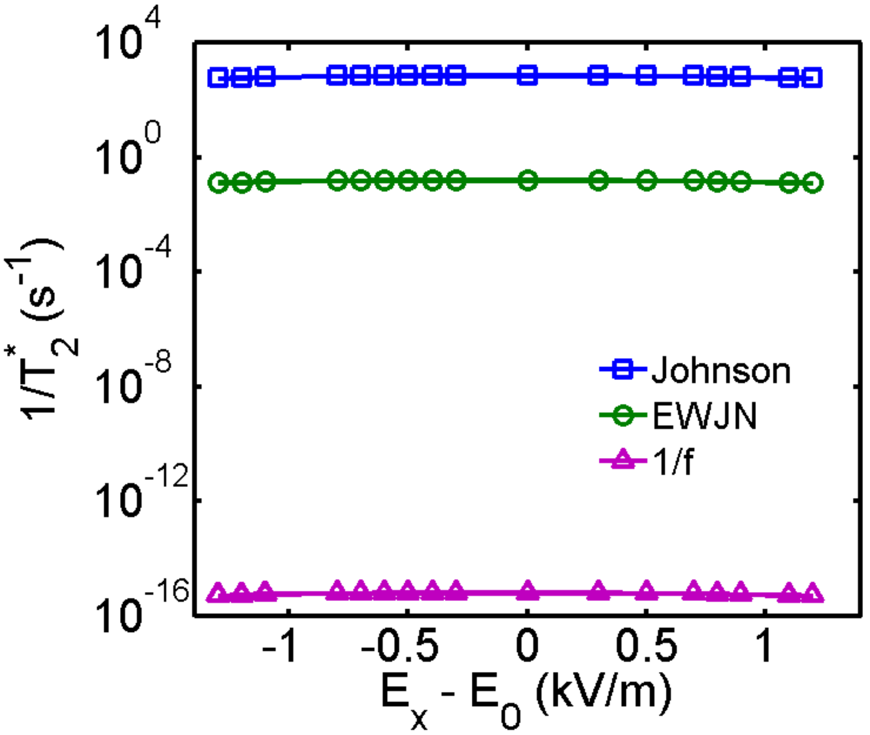

Fig. D.1. Comparison of the effects of Johnson noise, evanesant wave Johnson noise and $1/f$ noise on the decoherence rate $1/T_2^*$. The 2P-1P separation $R \approx 13$ nm and the applied static B-field is 0.5 T.

In Fig. D.1, we compare the effects of the three types of charge noise stated above on the decoherence rate $1/T_2^*$. As can be seen and stated in the main text, T_2^* is limited by Johnson noise. EWJN is at least 2 orders of magnitude lower than Johnson noise, and $1/f^\alpha$ noise is negligible, which is consistent with Ref. [75].

VITA

VITA

Yu Wang was born in Tianjin, China in 1989. He received his BSE from Beihang University, Beijing, China in 2008. He joined the PhD program in the School of Electrical and Computer Engineering at Purdue University in Fall 2012, and received his MS in Electrical and Computer Engineering in 2015. From 2012 to 2017, he was pursuing his PhD degree as a member of Nanoelectronic Modeling group under the guidance of Professor Gerhard Klimeck. His research at Purdue was focused on atomistic modeling of quantum devices for solid-state quantum spin logic applications.

NATURE PUBLISHING GROUP LICENSE TERMS AND CONDITIONS

Feb 14, 2017

This Agreement between Yu Wang ("You") and Nature Publishing Group ("Nature Publishing Group") consists of your license details and the terms and conditions provided by Nature Publishing Group and Copyright Clearance Center.

License Number	4047680459651
License date	Feb 14, 2017
Licensed Content Publisher	Nature Publishing Group
Licensed Content Publication	Nature
Licensed Content Title	A silicon-based nuclear spin quantum computer
Licensed Content Author	B. E. Kane
Licensed Content Date	May 14, 1998
Licensed Content Volume	393
Licensed Content Issue	6681
Type of Use	reuse in a dissertation / thesis
Requestor type	academic/educational
Format	electronic
Portion	figures/tables/illustrations
Number of figures/tables/illustrations	1
Figures	Figure 1
Author of this NPG article	no
Your reference number	
Title of your thesis / dissertation	Design and optimization of donor-based spin qubits in silicon
Expected completion date	May 2017
Estimated size (number of pages)	100
Requestor Location	Yu Wang Discovery Learning Research Center 207 South Martin Jischke Drive WEST LAFAYETTE, IN 47906 United States Attn: Yu Wang
Billing Type	Invoice
Billing Address	Yu Wang Discovery Learning Research Center 207 South Martin Jischke Drive WEST LAFAYETTE, IN 47906 United States Attn: Yu Wang
Total	0.00 USD

Terms and Conditions for Permissions

Nature Publishing Group hereby grants you a non-exclusive license to reproduce this material for this purpose, and for no other use,subject to the conditions below:

1. NPG warrants that it has, to the best of its knowledge, the rights to license reuse of this material. However, you should ensure that the material you are requesting is original to Nature Publishing Group and does not carry the copyright of another entity (as credited in the published version). If the credit line on any part of the material you have requested indicates that it was reprinted or adapted by NPG with permission from another source, then you should also seek permission from that source to reuse the material.

2. Permission granted free of charge for material in print is also usually granted for any electronic version of that work, provided that the material is incidental to the work as a whole and that the electronic version is essentially equivalent to, or substitutes for, the print version.Where print permission has been granted for a fee, separate permission must be obtained for any additional, electronic re-use (unless, as in the case of a full paper, this has already been accounted for during your initial request in the calculation of a print run).NB: In all cases, web-based use of full-text articles must be authorized separately through the 'Use on a Web Site' option when requesting permission.

3. Permission granted for a first edition does not apply to second and subsequent editions and for editions in other languages (except for signatories to the STM Permissions Guidelines, or where the first edition permission was granted for free).

4. Nature Publishing Group's permission must be acknowledged next to the figure, table or abstract in print. In electronic form, this acknowledgement must be visible at the same time as the figure/table/abstract, and must be hyperlinked to the journal's homepage.

5. The credit line should read:
   Reprinted by permission from Macmillan Publishers Ltd: [JOURNAL NAME] (reference citation), copyright (year of publication)
   For AOP papers, the credit line should read:
   Reprinted by permission from Macmillan Publishers Ltd: [JOURNAL NAME], advance online publication, day month year (doi: 10.1038/sj.[JOURNAL ACRONYM].XXXXX)

   Note: For republication from the *British Journal of Cancer,* the following credit lines apply.
   Reprinted by permission from Macmillan Publishers Ltd on behalf of Cancer Research UK: [JOURNAL NAME] (reference citation), copyright (year of publication)For AOP papers, the credit line should read:
   Reprinted by permission from Macmillan Publishers Ltd on behalf of Cancer Research UK: [JOURNAL NAME], advance online publication, day month year (doi: 10.1038/sj.[JOURNAL ACRONYM].XXXXX)

6. Adaptations of single figures do not require NPG approval. However, the adaptation should be credited as follows:

   Adapted by permission from Macmillan Publishers Ltd: [JOURNAL NAME] (reference citation), copyright (year of publication)

   Note: For adaptation from the *British Journal of Cancer,* the following credit line applies.
   Adapted by permission from Macmillan Publishers Ltd on behalf of Cancer Research UK: [JOURNAL NAME] (reference citation), copyright (year of publication)

7. Translations of 401 words up to a whole article require NPG approval. Please visit http://www.macmillanmedicalcommunications.com for more information.Translations of up to a 400 words do not require NPG approval. The translation should be credited as follows:

   Translated by permission from Macmillan Publishers Ltd: [JOURNAL NAME] (reference citation), copyright (year of publication).

Note: For translation from the *British Journal of Cancer,* the following credit line applies.
Translated by permission from Macmillan Publishers Ltd on behalf of Cancer Research UK: [JOURNAL NAME] (reference citation), copyright (year of publication)

We are certain that all parties will benefit from this agreement and wish you the best in the use of this material. Thank you.
Special Terms:
v1.1

Questions? customercare@copyright.com or +1-855-239-3415 (toll free in the US) or +1-978-646-2777.

Home Account Info Help

Title: Corrigendum: Characterizing Si:P quantum dot qubits with spin resonance techniques

Author: Yu Wang, Chin-Yi Chen, Gerhard Klimeck, Michelle Y. Simmons, Rajib Rahman

Publication: Scientific Reports

Publisher: Nature Publishing Group

Date: Nov 30, 2016

Logged in as:
Yu Wang
Account #:
3000930032

LOGOUT

Author Use

Authors of NPG articles do not require permission to use content from their article in most cases as stated in the author's guidelines.

Authors wishing to use their article for commercial purposes must request permission in the normal way.

For further questions, please contact NPG's permissions department: permissions@nature.com

BACK CLOSE WINDOW

For commercial reprints of this content, please select the Order Commercial Reprints link located beside the Rights and Permissions link on the Nature Publishing Group Web site.

Title: Characterizing Si:P quantum dot qubits with spin resonance techniques

Author: Yu Wang, Chin-Yi Chen, Gerhard Klimeck, Michelle Y. Simmons, Rajib Rahman

Publication: Scientific Reports

Publisher: Nature Publishing Group

Date: Aug 23, 2016

Logged in as:
Yu Wang
Account #:
3000930032

LOGOUT

Author Use

Authors of NPG articles do not require permission to use content from their article in most cases as stated in the author's guidelines.

Authors wishing to use their article for commercial purposes must request permission in the normal way.

For further questions, please contact NPG's permissions department: permissions@nature.com

BACK CLOSE WINDOW

For commercial reprints of this content, please select the Order Commercial Reprints link located beside the Rights and Permissions link on the Nature Publishing Group Web site.

nature publishing group

Title: Highly tunable exchange in donor qubits in silicon

Author: Yu Wang, Archana Tankasala, Lloyd C L Hollenberg, Gerhard Klimeck, Michelle Y Simmons et al.

Publication: npj Quantum Information

Publisher: Nature Publishing Group

Date: Apr 12, 2016

Logged in as:
Yu Wang
Account #:
3000930032

LOGOUT

Author Use

Authors of NPG articles do not require permission to use content from their article in most cases as stated in the author's guidelines.

Authors wishing to use their article for commercial purposes must request permission in the normal way.

For further questions, please contact NPG's permissions department: permissions@nature.com

BACK CLOSE WINDOW

For commercial reprints of this content, please select the Order Commercial Reprints link located beside the Rights and Permissions link on the Nature Publishing Group Web site.

NATURE PUBLISHING GROUP LICENSE
TERMS AND CONDITIONS

Feb 14, 2017

This Agreement between Yu Wang ("You") and Nature Publishing Group ("Nature Publishing Group") consists of your license details and the terms and conditions provided by Nature Publishing Group and Copyright Clearance Center.

License Number	4047820386289
License date	Feb 14, 2017
Licensed Content Publisher	Nature Publishing Group
Licensed Content Publication	Nature Communications
Licensed Content Title	Spin readout and addressability of phosphorus-donor clusters in silicon
Licensed Content Author	H. Büch, S. Mahapatra, R. Rahman, A. Morello, M. Y. Simmons
Licensed Content Date	Jun 18, 2013
Licensed Content Volume	4
Type of Use	reuse in a dissertation / thesis
Requestor type	academic/educational
Format	electronic
Portion	figures/tables/illustrations
Number of figures/tables/illustrations	1
High-res required	no
Figures	Figure 1
Author of this NPG article	no
Your reference number	
Title of your thesis / dissertation	Design and optimization of donor-based spin qubits in silicon
Expected completion date	May 2017
Estimated size (number of pages)	100
Requestor Location	Yu Wang Discovery Learning Research Center 207 South Martin Jischke Drive WEST LAFAYETTE, IN 47906 United States Attn: Yu Wang
Billing Type	Invoice
Billing Address	Yu Wang Discovery Learning Research Center 207 South Martin Jischke Drive WEST LAFAYETTE, IN 47906 United States Attn: Yu Wang

Total	0.00 USD

Terms and Conditions

Terms and Conditions for Permissions

Nature Publishing Group hereby grants you a non-exclusive license to reproduce this material for this purpose, and for no other use,subject to the conditions below:

1. NPG warrants that it has, to the best of its knowledge, the rights to license reuse of this material. However, you should ensure that the material you are requesting is original to Nature Publishing Group and does not carry the copyright of another entity (as credited in the published version). If the credit line on any part of the material you have requested indicates that it was reprinted or adapted by NPG with permission from another source, then you should also seek permission from that source to reuse the material.

2. Permission granted free of charge for material in print is also usually granted for any electronic version of that work, provided that the material is incidental to the work as a whole and that the electronic version is essentially equivalent to, or substitutes for, the print version.Where print permission has been granted for a fee, separate permission must be obtained for any additional, electronic re-use (unless, as in the case of a full paper, this has already been accounted for during your initial request in the calculation of a print run).NB: In all cases, web-based use of full-text articles must be authorized separately through the 'Use on a Web Site' option when requesting permission.

3. Permission granted for a first edition does not apply to second and subsequent editions and for editions in other languages (except for signatories to the STM Permissions Guidelines, or where the first edition permission was granted for free).

4. Nature Publishing Group's permission must be acknowledged next to the figure, table or abstract in print. In electronic form, this acknowledgement must be visible at the same time as the figure/table/abstract, and must be hyperlinked to the journal's homepage.

5. The credit line should read:
   Reprinted by permission from Macmillan Publishers Ltd: [JOURNAL NAME] (reference citation), copyright (year of publication)
   For AOP papers, the credit line should read:
   Reprinted by permission from Macmillan Publishers Ltd: [JOURNAL NAME], advance online publication, day month year (doi: 10.1038/sj.[JOURNAL ACRONYM].XXXXX)

   Note: For republication from the *British Journal of Cancer,* the following credit lines apply.
   Reprinted by permission from Macmillan Publishers Ltd on behalf of Cancer Research UK: [JOURNAL NAME] (reference citation), copyright (year of publication)For AOP papers, the credit line should read:
   Reprinted by permission from Macmillan Publishers Ltd on behalf of Cancer Research UK: [JOURNAL NAME], advance online publication, day month year (doi: 10.1038/sj.[JOURNAL ACRONYM].XXXXX)

6. Adaptations of single figures do not require NPG approval. However, the adaptation should be credited as follows:

   Adapted by permission from Macmillan Publishers Ltd: [JOURNAL NAME] (reference citation), copyright (year of publication)

   Note: For adaptation from the *British Journal of Cancer,* the following credit line applies.
   Adapted by permission from Macmillan Publishers Ltd on behalf of Cancer Research UK: [JOURNAL NAME] (reference citation), copyright (year of publication)

7. Translations of 401 words up to a whole article require NPG approval. Please visit http://www.macmillanmedicalcommunications.com for more information.Translations of up to a 400 words do not require NPG approval. The translation should be credited as follows:

Translated by permission from Macmillan Publishers Ltd: [JOURNAL NAME] (reference citation), copyright (year of publication).

Note: For translation from the *British Journal of Cancer,* the following credit line applies.
Translated by permission from Macmillan Publishers Ltd on behalf of Cancer Research UK: [JOURNAL NAME] (reference citation), copyright (year of publication)

We are certain that all parties will benefit from this agreement and wish you the best in the use of this material. Thank you.
Special Terms:
v1.1

Questions? customercare@copyright.com or +1-855-239-3415 (toll free in the US) or +1-978-646-2777.